ELECTROCHEMICAL STUDY OF PYRENE USING GLASSY CARBON ELECTRODE MODIFIED WITH METAL-OXIDE NANOPARTICLES AND A GRAPHENE OXIDE / MULTI-WALLED CARBON NANOTUBES NANOPLATFORM

DISEKO BOIKANYO

ELECTROCHEMICAL STUDY OF PYRENE USING GLASSY CARBON ELECTRODE MODIFIED WITH METAL-OXIDE NANOPARTICLES AND A GRAPHENE OXIDE / MULTI-WALLED CARBON NANOTUBES NANOPLATFORM

DISEKO BOIKANYO

B.Sc. (NWU), B.Sc. *Hons*. (NWU)

Dissertation submitted in fulfillment of the requirements for the degree

Master of Science
in the

Department of Chemistry

Faculty of Agriculture, Science and Technology

North-West University

Supervisor: **Prof. Eno. E. Ebenso**

Co-supervisor: Dr. Abolanle S. Adekunle

November 2015

DECLARATION

I hereby declare that the *Electrochemical Study of Pyrene Using Glassy Carbon Electrode Modified with Metal-Oxide Nanoparticles And a Graphene Oxide / Multi-walled Carbon Nanotubes Nanoplatform* submitted to the North West University, Faculty of Agriculture, Science and Technology, School of Mathematical and Physical Science, Department of Chemistry, is my own work and has not been submitted for any degree or examination in any other university, and that all sources have been quoted, indicated and acknowledged by means of complete references.

.....

Diseko Boikanyo

DEDICATION

I dedicate this to My Parents

My Mother, Emelda Mamothe Boikanyo and My Late Father, Thole Nelson Boikanyo.

Because they believed in me, when I did not and they moved Heaven and Earth to help me attain my dreams.

Ke Mokoena, Motlase!

Motho oa go lelala godima,

Tsa fatshe di lapisa molala!

ACKNOWLEDGEMENTS

First and foremost I acknowledge God, without whom none of this has been possible.

My deepest gratitude goes to Professor Eno Ebenso, my supervisor. I thank him for his patience, his tolerance, support, guidance and teaching. I thank him for his loyalty to his students, his fighting spirit and generosity. Thank you Professor Ebenso for inculcating in me a spirit of independence and initiative. I appreciate it more than you will ever know.

I thank my capable co-supervisor, Dr Abolanle Adekunle for introducing me to sensors, for teaching and being patient; always encouraging and pushing me to do better. Thank you for your support, vibrant enthusiasm and laughter throughout this project.

My mother, Emelda Boikanyo, for her profound strength; amidst the chaos, my anchor and pillar. Thank you, Mommy. Thank you Mothupi Boikanyo for helping with late night data capturing, Mothepana and Boikanyo for cheering me on, always! To Zolani, thank you for the companionship on this journey.

I would like to thank the Sasol Inzalo Foundation, the National Research Foundation and the North-West University for their financial support.

I am grateful to the North-West University Department of Chemistry staff and the MaSIM Research Group in their entirety for all their help. Special thanks to Mrs. Maggy Medupe, Dr. Mwadham Kabanda, Mr Kagiso Mokalane, Mr. Peter Mahlangu, Mr. Thato Majele, Mr. Sizwe Loyilane, Ms. Pearl Seoposengwe, Ms. Nomfundo Gumbi, Mrs. Omolola Fayemi, Mr. Lukman Olasunkanmi, Dr. Sassikumar Yesudass and Dr. Kaitano Dzinavatonga.

Thanks goes to Dr. Lucky Sikhwivhilu and Dr. Damian Onwudiwe for acquiring the TEM, SEM and XRD spectra.

ABSTRACT

This work describes and compares the electron transport and electrocatalytic properties of chemically synthesised cobalt oxide and nickel oxide using graphene oxide and acid treated multi-walled carbon nanotubes as supports grafted onto a glassy carbon electrode.

The successful synthesis of the metal oxides, carbon nanomaterials and nanocomposites was confirmed using various spectroscopic techniques such as Ultra violet-Visible (UV-Vis), Fourier transform – infra red (FT-IR) , X-ray diffraction spectroscopy (XRD), Electron dispersive X-ray spectroscopy (EDX), Raman spectroscopy and microscopic techniques such as Scanning electron microscope (SEM) and Transmission electron microscope (TEM) .

After electrode modification using the drop-casting method, comparative electrochemical studies were carried out in 0.1 M pH 7 phosphate buffer (PBS) and in 5mM ferricyanide/ ferrocyanide ($[Fe(CN)_6^{3-}]/[Fe(CN)_6^{4-}]$) outer sphere model redox probe using cyclic voltammetry (CV) and electrochemical impedance spectroscopy (EIS) in order to establish the electron transfer properties of the modified electrodes.

The electron transport between the various nanomaterials and / or their nanocomposites was detailed using EIS. This revealed that the modified electrodes have a pseudocapacitive nature as a result of the combined activity of the carbon nanomaterials (the double layer capacitor) and the electron conducting metal oxide nanoparticles.

The performance of the modified electrodes relative to the unmodified GCE in pyrene was studied using cyclic voltammetry and impedance measurements.

It was found that the metal oxides demonstrate better performance when the carbon nanotubes were used as a grafting support.

The fMWCNT-MO modified electrodes demonstrated faster electron transport and a dramatically enhanced catalytic current when compared to the same metal oxides grafted onto the graphene oxide (GO). This inefficient performance of the GO based electrodes is associated with a larger proportion of unreactive basal planes exposed relative to the reactive edge planes of the GO.

To better understand the mechanism of electrocatalytic oxidation of pyrene on the modified electrode surface, EIS was used to validate and compliment the results obtained using cyclic voltammetry.

The charge transfer resistance, electron transfer rate constant (k_s), Tafel value, limit of detection (LoD), sensitivity, adsorption equilibrium constant (β), Gibbs free energy change due to the adsorption (ΔG^o_{ads}) of pyrene onto the GCE-fMWCNT-Co_3O_4 were established and discussed. The LoD and ΔG^o_{ads} for pyrene were 1.62 nM and -15.8 kJ/mol, respectively, over a linear dynamic range of 1.0×10^{-9} – 100×10^{-9} M . The electro-oxidation of pyrene was a diffusion dominated process, but demonstrated adsorption thought to be as a result of a combination of the strong pi-pi electron interactions between pyrene and the MWCNT, thus the thin film formed on the surface of the electrode by the analyte and its reaction intermediates.

In conclusion, this research work has demonstrated that cobalt oxide supported on acid functionalised multi-walled carbon nanotubes grafted onto glassy carbon electrode can be used as a sensitive and low cost electrochemical sensor for the detection of pyrene; one of a group of recalcitrant, ubiquitous, toxic and carcinogenic persistent organic pollutants.

TABLE OF CONTENTS

LIST OF ABBREVIATIONS

A	Electrode surface area (cm^2)
Ag	Silver wire pseudo-reference electrode
Ag/AgCl	Silver/silver chloride reference electrode
CME	Chemically modified electrode
CNT	Carbon nanotubes
CV	Cyclic voltammetry
CV	Cyclic voltammogram
DMF	Dimethylformamide
EIS	Electrochemical impedance spectroscopy
$Fe_4(III)[Fe(II)(CN)_6]^3$	Divalent iron (II)/(III) cyanide complex
Fmwcnt	functionalised Multi-walled carbon nanotubes
FTIR	Fourier transform infrared
GCE	Glassy carbon electrode
LCR	Linear concentration range
LoD	Limit of detection
MO	Metal oxide
MWCNT	Multi-walled carbon nanotubes
NPs	Nanoparticles
PBS	Phosphate buffer solution
R.E.	Reference electrode
R_{ad}	Resistance due to adsorption
SCE	Standard calomel electrode
SEM	Scanning electron microscopy
SWCNT	Single-walled carbon nanotubes.
SWV	Square wave voltammetry
W.E.	Working electrode
XPS	X-ray photoelectron spectroscopy

LIST OF SYMBOLS

α	Rate of electron transfer
Γ	Surface coverage or concentration
π	Pi bonding
λ	Wavelength
A	Absorbance
c	Molar concentration of analyte
C	Capacitance
C_{dl}	Double-layer capacitance
CPE	Constant phase electrode
C_{Ox}	Concentration of the oxidized form of an analyte
C_{Red}	Concentration of the reduced form of an analyte
C_s	Specific interfacial capacitance
d	Diameter
D	Diffusion coefficient
E_f	Final potential
E_i	Starting potential
E_{pa}	Anodic peak potential
E_{pc}	Cathodic peak potential
E	Potential
E_o	Standard potential
$E_{1/2}$	Half-wave potential
ΔE_p	Anodic-to-cathodic peak potential separation
f	Frequency
F	Faraday constant
H	Plank's constant
Hz	Hertz
I_{abs}	Absorbed light
i_{pa}	Anodic peak current
i_{pc}	Cathodic peak current
k_s	Heterogeneous electron transfer coefficient
K^o	Equilibrium constant
K_a	Dissociation constant

K	Kelvin
n	Number of electron
N_A	Avogadro's constant
q	Electrical charge
Q	Electrical charge (C)
R	Universal gas constant
R_{ct}	Charge transfer resistance
R_s	Resistance of electrolyte soltuion
v	Scan rate
V	Volts
Z(Im)	Imaginary impedance
Z(Re)	Real impedance
Zw	Warburg impedance

LIST OF FIGURES

LIST OF TABLES

LIST OF SCHEMES

CHAPTER 1

INTRODUCTION

1.1 BACKGROUND

1.1.1 Persistent Organic Pollutants (POPs)

Post the World War II industrial boom; scientists became cognisant of Persistent Organic Pollutants (POPs). These chemicals had been used extensively during the industrial expansion. Most of them had been used for pest and disease vector control as well as in industry for the production of a multitude of consumables with great success. It was found that they were characterised by a particular set of physico-chemical properties such that, once discharged into the environment, they could easily withstand photo degradation, abiotic and biodegradation and as such were capable of global distribution and more importantly the ability to accumulate to levels that were detrimental to living organisms [1].

POPs are a group of chemicals that persist in the environment. Their persistence stems primarily from the fact that they have long half-lives- ranging from years to decades- in soils, sediments, air and biota because of their resistance to degradation. Typically, POPs are hydrophobic (water-hating) and lipophilic (fat-loving) chemicals. That they are lipophilic means they tend to partition into the lipids in cells and become stored in fatty tissue, they are also slow to metabolise and this confers persistence in that they would bio-accumulate in the food web. These chemicals have been found in pristine environments and regions where they have never been used or produced, which indicates that they are subject to long-range transport; where they enter the gas-phase under environmental temperatures and volatilise from soils and water bodies into the atmosphere and proceed to travel long distances before they are re-deposited [2, 3].

The cycle of volatilisation and deposition, their stability and resistance to metabolism and lipophilicity means they are subject to long-range atmospheric transport, bioaccumulation and

therefore, magnification in the food chain. This is the reason for concern about their toxicity on wildlife and humans. Since the early 1960's a multitude of studies conducted have documented the deleterious effects that the residues of POPs such as organochlorine pesticides (OCPs), polychlorinated biphenyls (PCBs) and polynuclear aromatic hydrocarbons (PAHs) have had on the environment and various living organisms [4].

POP's have been identified as hormone disruptors that alter the normal function of endocrine systems. In addition to this, they exhibit a wide range toxicological response such as immunotoxicity, teratogenicity and carcinogenicity. Of the many POP's that have been identified as carcinogens, poly aromatic hydrocarbons (PAH's) are the most obvious example, causing damage to the immune systems of people and wildlife and thus making them susceptible to disease and changes in behavioural patterns due to neurobehavioural impairment, promoting tumours and cancers, developmental abnormalities and reproductive deficiency [5-7].

The propensity for POPs to trans-boundary travel was the major impetus of the Stockholm Convention. The global threat of POPs necessitated a multi-lateral approach; and so in May 1995 the Governing Council of the United Nations Environmental Programme (UNEP) requested that an international process be undertaken to evaluate the twelve POPs initially listed for consideration. In June 1998 talks began wherein the text for an international legally binding instrument was negotiated and concluded in December 2000. Ultimately, the ground-breaking United Nations Treaty known as the Stockholm Convention on Persistent Organic Pollutants was signed in Stockholm , Sweden on 23 May 2001 [8]. The Convention entered into force on 17 May 2004. The Republic of South Africa ratified the Convention on 23 May 2001 and became a party on the 4 September 2002.

The main objective of the Stockholm Convention is to protect human health and the environment from persistent organic pollutants, specifically to reduce and eliminate the use and release of the originally identified 12 POPs. Under this general goal, there are specific provisions of the Convention that require each party member to prohibit and take legal and administrative action required for the elimination/reduction of POPs production and use, export and import, as well as to take actions to minimize or prevent POPs releases.

South Africa's National Department of Environmental Affairs in consultation with other departments is responsible for the implementation of the Stockholm Convention. In January 2007, the Enterprise Industry Development division of the DTI assessed the current capacity of laboratories in the country. The report identified that South Africa has limited capacity in terms of facilities and trained technical staff to measure POPs and even when POP analysis is possible, not all laboratories can analyze the full range of POPs [9]. Thus in light of the major concerns regarding the toxicity of POPs, there is a growing need for innovative ways to monitor these environmental pollutants.

1.1.2 Electrochemical Sensors

Electrochemical sensors have played an increasing role in environmental monitoring. Such devices have made it possible to carry out the measurement of numerous inorganic and organic pollutants from a central laboratory to the field and to perform them rapidly, inexpensively and reliably. Specifically, electrochemical sensors and detectors have great potential for addressing environmental needs, especially in the on-site detection of priority pollutants. These devices satisfy most of the requirements for on-site environmental analysis: they are characteristically sensitive and selective towards electro-active species, fast and accurate, compact, thus portable, as well as inexpensive.

The function of a sensor is to provide real-time information about the chemical composition of its environment. For electrochemical sensors, the analytical information is obtained from the electrical signal that results from the interaction between the recognition layer and the target analyte. Depending on the nature of the sample matrix as well as sensitivity and selectivity requirements, different electrochemical devices can be used for the task.

Various electrode substrates such as noble metals, mercury, carbon as well as composite materials have been exploited. Choosing an appropriate electrode substrate is critical for successful electrochemical analysis. Prediction of the efficacy of the electrode substrate is helpful and is based on two main factors: the redox behaviour of the target analyte and the other is the background current over the potential range applied in the measurements. With this, some other factors should be taken into consideration such as the electrical conductivity, mechanical properties, toxicity, cost etc. [10] .

Bare electrodes are not always ideal, thus chemically modified electrodes (CME) were developed to improve the situation. The modification of an electrode essentially involves the immobilization of reagents that change the electrochemical characteristics of the bare electrode surface. These chemical layers have also been used to impart a high degree of selectivity and sensitivity to the electrochemical transducer. Different electrochemical devices have been developed for environmental monitoring. The design and advancement of such devices depends on the nature of the analyte, characteristics of the sample matrix as well as sensitivity and selectivity requirements.

1.1.3 Nanoparticles and Chemically Modified Electrodes

Nanoparticles (NPs) are increasingly attracting attention due to their unique properties that differ greatly from those of bulk materials. Nanoparticles have one dimension sized from 1-100

nm. Nanomaterials owe their uniqueness to their mechanical, electrical, optical, and magnetic properties as well as their chemical, catalytic and geometric characteristics- which essentially means they have extremely high surface area per mass [11].

Nanoparticle modified electrodes exhibit advantages over the typical bulk material modified electrode. In the first instance nanomaterials offer a large specific surface area that facilitates the immobilization of more functional molecules on the electrode surface. Secondly, some semiconducting nanomaterials are able to act as promoters, thus accelerating the rate of electron transfer between the target analyte and the electrode substrate. Also, in addition to the novel properties, nanomaterials and nanotechnology yield new approaches to the fabrication of electrodes cost effectively by minimizing materials and waste generated [10, 12, 13].

Electrocatalysis is a process which facilitates electron transfer between the analyte and the surface by an immobilized catalyst. It is this catalytic action that results in faster electrode reactions at lower operating potentials. There are numerous catalytic surfaces that have thus been successfully employed for a variety of environmental monitoring applications, including water-quality parameters (conductivity, dissolved oxygen and pH) [14], trace detection of heavy metals, carcinogens and organic pollutants [15]. The nanomaterial's most used are generally divided into categories based on their chemical nature, namely:

1. Metals;
2. Metal-oxides;
3. Carbonaceous;
4. Polymeric and Dendrimeric; and,
5. Composites.

Many methods have been put forward for the determination of POPs. However, despite the fact that traditional instrumental methods have high accuracy and low detection limits, they present a significant problem in many instances where capacity and funds are limited because they require sample preparation step prior to detection- this is time consuming and tedious.

Presently, instrumental methods of analysis are heavily relied upon for the determination, detection and degradation of POPs. However, the major setback with instrumental techniques is the fact that they are expensive, and are not easily amenable to site applications; in most instances they require extensive pre-treatment sample preparation prior to analyte quantification. Most instrumental techniques have long measurement times and complicated operation and do not indicate whether target analytes are accessible for uptake by living organisms. The health risks posed by POPs require the development of a much simpler, rapid, low cost, robust and reliable method for their detection.

Electrochemical analysis is a powerful technique that offers multiple advantages such as high sensitivity, selectivity, rapid analysis times, reduction in solvent and sample consumption as well as ease of use and low operating costs[16]. Based on this, electrochemical methods are considered very promising techniques for environmental monitoring and protection.

Electroanalytical methods have also shown certain advantages over other analytical methods. Electrochemical analysis allows for the determination of different oxidation states of a compound in a solution and not just the concentration of the compound, thus an abundance of information can be obtained, including electron transfer and chemical kinetics, and the elucidation of reaction mechanisms. Electroanalytical techniques are also capable of producing exceptionally low limits of detection.

1.2 PROBLEM STATEMENT

Persistent organic pollutants (POPs) are a group of organic compounds of natural or anthropogenic origin that resist photolysis, chemical and biological degradation as a result, they persist in soils, sediment, biota and air. These chemicals are characterised by a specific set of physico-chemical properties such that once discharged into the environment they are easily able to accumulate in the biosphere to levels detrimental to living organisms.

Traditional instrumental analytical techniques currently in existence for the determination of POPs include chromatography (TLC, GC, HPLC), spectroscopy (UV-Vis, IR, MS) or hyphenated methods (GC-MS), immunoassay and spectrofluorometry. Despite the fact that conventional instrumental methods have high accuracy and low detection limits, they are expensive, require extensive pre-treatment stages before analyte quantification and are generally not amenable to miniaturization for on-site application.

In view of the considerable health risks to the environment due to POPs, there is a critical need for the rapid detection of trace-level quantities of these compounds. The use of modified electrodes as sensors offers an alternative because of the many advantages such as ease of use, minimal sample preparation, relatively rapid response, low cost, is easily miniaturised and offer a wide linear dynamic range. As a result of these advantages, numerous types of electrochemical sensors have been developed for various types of analytes in the past several years.

One of the key factors in the development of superior performing electrode sensors is the substrates used to modify the electrode surface. Over the past several years carbon based nanomaterials such as graphene and carbon nanotubes have garnered increasing attention for the development of advanced high performance electronics, sensors and fuel-cell applications.

Application of metal-oxide nanomaterials in sensor applications is also very promising due to the fact that metal-oxides provide robust building blocks and offer functionalities such as electrical conductivity and high catalytic activity, thus they have attracted an increasing amount of technological and industrial interest. Despite all of this, the potential electrochemical and electrocatalytic capacity of carbon nanomaterials in combination with metal oxide nanoparticles to form nanocomposites for use as substrates for the modification of electrode surfaces to use in the determination of persistent organic pollutants has not been deeply explored.

The work presented herein details the electron transport and electrocatalytic characteristics of graphene/(oxide)(GR/ GO) and multi-walled carbon nanotubes(MWCNTs) as a support for metal oxide nanoparticles (MONP) grafted onto a glassy carbon electrode (GCE) for the detection of environmentally important analytes, *viz.*: Pyrene, Fluorene, Phenanthrene, Heptachlor and 2-Bromobiphenyl.

1.3 RESEARCH JUSTIFICATION

Based on the need to protect public health and the environment, it is critical to monitor air, soil and water for contaminants such as POPs. It is especially critical to limit their toxicity and accumulation in living organisms. To achieve this, trace-level detection is desirable and this necessitates the development of new methods for detection at low concentrations in the field. A range of analytical techniques such as chromatographic methods, mass spectroscopy, spectrophotometry, fluorimetry, capillary electrophoresis, chemiluminescence have been developed in the past. However, these methods require several derivatization procedures which are time consuming and very expensive. Therefore, there is a need for the fabrication of highly sensitive and selective electrochemical sensor for routine monitoring of POPs in our environment. Electroanalytical chemistry plays a critical role in the protection of our

environment. Electrochemical sensors in particular have shown great promise for the on-site monitoring of the priority pollutants. These devices are of great interest because they can be tailor-made to fulfil the requirements for on-site environmental analysis. They can be easily miniaturized for portability, are inherently sensitive and selective for the detection of electroactive species as compared with the conventional methods such as GC, GC-MS, HPLC etc. that are presently used.

Graphene, as a nanomaterial, has attracted attention in many areas of research for applications in biomedicine, energy, electronic storage devices, catalysis and sensors. Graphene has a high specific surface area; its modification with other functional groups or nanoparticles can be used to increase the interaction of graphene with organic pollutants so they can be detected in solution through catalytic oxidation. Similarly, Nickel oxide and Cobalt oxide based nanocomposites have demonstrated great potential in the applications of electrochemical sensors and supercapacitors and fuel cells [17, 18]. Co_3O_4 and NiO are attractive materials for application as electrode modifiers because of their cost effectiveness, ease of synthesis and high electrocatalytic activity. Therefore, motivation for this study is to explore the combined catalytic properties of graphene/metal-oxide nanocomposites towards trace persistent organic pollutants detection and quantification in our environment (e.g. water). In this work, we propose the development of a sensitive, selective electrochemical sensor for the detection of Pyrene using NiO/Graphene and Co_3O_4/Graphene nanocomposite modified glassy carbon electrode. To the best of our knowledge, the use of these nanocomposite materials for the determination of the PAHs has not been reported.

1.4 RESEARCH AIMS AND OBJECTIVES

1.4.1 Aim

The aim of the research is to explore the sensing properties of Graphene oxide and acid functionalised multi-walled carbon nanotubes used as supports for metal oxides (NiO and Co_3O_4) to form nanocomposite for the electro catalysis and analysis pyrene.

1.4.2 Objectives

The objectives of this project are to:

1. Synthesize graphene oxide nanosheets from graphite flakes and functionalize multi-walled carbon nanotubes via acid treatment

2. Synthesize metal oxide nanoparticles (nickel oxide (NiO) and cobalt (II, III) oxide (Co_3O_4));
3. Synthesize metal oxide|graphene oxide and metal oxide|MWCNT nanocomposites and characterize them using various spectroscopic and microscopic characterization techniques such as: FT-IR, UV-Vis, XRD, EDX, Raman Spectroscopy, SEM and TEM to confirm.
4. To fabricate a sensor by modifying the glassy carbon electrode substrate surface using the synthesized nanoparticles.
5. To use electrochemical techniques to determine the sensor properties of the graphene oxide, metal oxides and the nanocomposite towards persistent organic pollutants' detection and quantification.
6. To explore the synergistic interaction of the metal oxide|graphene oxide and metal oxide |fMWCNT nanocomposite in enhancing the detection of the pyrene.

7. To determine the adsorptive properties of pyrene, as it impacts on it's detection by the sensor by evaluating the adsorption equilibrium constant (K_{ad}) using Langmuir adsorption theory, and determining the electrochemical Gibbs free energy change (ΔG^{o}) due to adsorption.

CHAPTER 2

LITERATURE REVIEW

2.1 ORGANIC POLLUTANTS

Persistent organic pollutants are a group of varied organic chemicals that are persistent in the environment. Their persistence stems from the fact that they have long half-lives, spanning years to decades because they have an innate ability to resist degradation in various media (air, water, sediments, and organisms); are hydrophobic and lipophilic, which allows them to bio-accumulate in living tissues at levels higher than those in the surrounding environment and ultimately, through the food chain; are predisposed to entering the gas phase by volatilisation under environmental temperatures and are subject to long-range transport and as a result are globally distributed and even found in pristine environments , where they have never been used . Animal and human studies have linked a variety of health problems to exposure to POPs, such as reproductive abnormalities, birth defects, immune system dysfunction, neurological defects and cancer [19].

The Governing Body of the United Nations Environmental Programme (UNEP) initially listed 12 POPs, aptly named the “Dirty Dozen” for global banning or severe restriction. The twelve legacy organochlorine substances consist of two byproducts (polychlorinated dibenzo-*p*-dioxins and polychlorinated dibenzofurans (PCDDs/DFs)), one industrial product (polychlorinated biphenyls (PCBs)), and nine pesticides (DDTs, chlordane, heptachlor, aldrin, dieldrin, toxaphene, mirex and hexachlorobenzene(HCB)) [8].

In addition to those listed above, there are numerous other POPs that are environmental pollutants of significant concern. Most are both impervious to degradation and toxic. Some remain in wide spread production and use in both first world and developing countries. Since 1998, the United Nations Economic Commission for Europe has included an additional number of POPs- hexachlorocyclohexanes (HCHs), chlordecone and hexabromobiphenyl and poly aromatic hydrocarbons (PAHs).

The substances not initially listed are now referred to as “emerging POPs”; these are the pollutants that have recently been discovered and believed to be dangerous to both human and wildlife. Typical examples of emerging POPs, include the brominated flame retardants (BFRs), polybrominated diphenyl ethers(PBDEs), perfluorinated compounds and polychlorinated naphthalenes (PCNs) [20].

As a result of the shifts in the manufacturing and industries base to developing countries, it is found that there is an increase in the types and sources of emerging POPs such as PBDEs, which are used as flame retardants in household products, and unintentionally produced substances like polyaromatic hydrocarbons (PAHs), dioxins and furans.

2.2 POLYAROMATIC HYDROCARBONS (PAHs)

Polyaromatic hydrocarbons (PAHs) are often not included in the POPs category despite the fact that they have proven to be persistent in the environment and harmful to humans and wildlife. These compounds are found in natural sources, but in developing countries, their most important sources are vehicles, industries and burning of firewood for cooking. Table 2.1 below lists the Environmental Protection Agency (EPAs) 16 Priority PAHs.

Table 2.1: Toxic PAHs listed on priority list by United States Agency for Toxic Substances and Disease Registry (US EPA), Priority PAHs [21].

Priority PAHs			
(1) Acenaphthene (2) Fluoranthene (3) Benzo(k)fluoranthene (4) Naphthalene	(5) Chrysene (6)Benzo(a)pyrene (7)Acenaphthylene (8)Benzo(a)anthracene	(9) Dibenzo(a,h)anthracene (10)Anthracene (11)Benzo(b)fluoranthene (12) Benzo(ghi)perylene	(13)Phenanthrene (14)Benzo(j)fluoranthene (15) Indeno(1,2,3-c,d)pyrene (16) Pyrene

2.2.1 Poly Aromatic Hydrocarbons and their Physical and Chemical Characteristics

Polyaromatic hydrocarbons (PAHs) are non-polar compounds, also known as polynuclear aromatic hydrocarbons or polyarenes, containing two or more aromatic rings that are fused together by sharing a pair of carbon atoms. The resultant structures are molecules where all hydrogen atoms lie in one plane.

The smallest of these is Naphthalene, formed from two benzene rings ($C_{10}H_8$; M_w= 128.1705 g/mol) and Anthracene with three aromatic rings ($C_{14}H_{10}$; M_W= 178.2292 g/mol) have the lowest molecular weights. The PAHs with four to seven aromatic rings have higher molecular weights.

PAHs are very stable compounds that occur both naturally and as a result of human activities. They generally occur as complex mixtures and not as singular compounds. The physical and chemical characteristics of PAHs vary extensively with molecular weight. The environmentally significant PAHs, are those molecules with two to seven benzene rings and within this range there are a number of PAHs that differ in the number of aromatic ring, the position at which they are fused to each other and number, chemistry as well as the position of substituents on the fundamental ring system. Their difference in behaviour is as a result of the variation in molecular weight; where PAH resistance to reduction, oxidation and volatilisation increases with increasing molecular weight, however, their aqueous solubility decreases [22]. In their pure form, PAHs exist as white, colourless or pale-hued solids with faint odours.

Among the most persistent organic pollutants extensively studied in the environment PAHs are the most pervasive as they occur in air, water, soil as well as plant and animal tissues. Their lipophilicity means they would tend to mix more readily with oil than water; and the substances with higher molecular weight being even less water soluble and less volatile means that PAHs are found adsorbed to soil and sediment particles than water or air [23].

PAHs are only very slightly soluble in water because they are non-polar hydrophobic compounds that do not ionise. Typically PAH solubility in aqueous media decreases with an increase in molecular weight. The low molecular weight compounds are inclined to be more soluble and volatile than the heavier PAHs, which are soluble in most organic solvents. The presence of different moieties on the aromatic ring results in a decrease in solubility, but exceptions exist, *i.e.* benz[a]anthracene is less soluble than both methyl and ethylbenz[a]anthracene. PAH molecules with a linear arrangement are most likely less soluble than perifused molecules. PAHs usually occur as complex mixtures [24] . The molecular weight of PAHs plays a significant role in their behaviour in as far as physical and chemical properties are concerned. PAHs are characterised by high liphophilicity as measured by the water/octanol partition coefficients. The combination of their neutrality, stability and hydrophobic nature means that the concentrations of PAHs dissolved in water are very low; they adsorb onto organic matter in sediment. They show long half-lives, for example, in aerobic sediment, they show half-lives ranging from three weeks for naphthalene to 300 weeks for benzo [a] pyrene [25]. The persistence of PAHs increases with ring number and degree of condensation. PAHs sometimes contain additional fused rings that are not six-sided. Their low vapour pressure means some PAHs are present in the atmosphere at ambient temperature as both gas and particle-associated. Lighter PAHs such as phenanthrene are found in the gas-phase, with the heavier compounds like benzo[a]pyrene (B[a]P), which contains five rings , are totally adsorbed onto particulate matter [21].

2.2.2 Sources and Formation of Poly Aromatic Hydrocarbons

2.2.2.1 Natural Sources

Poly aromatic hydrocarbons in nature are formed via three pathways: (i) high temperature pyrolysis of organic materials; (ii) during the formation of fossil fuels through the low-to-moderate temperature diagenesis of sedimentary organic material and; (iii) direct biosynthesis by microbes and plants [24] .

Fires are by far the largest contributors of PAH volumes from a natural source into the atmosphere. These are forest fires, grassland fires as well as deliberate agricultural burning. The type of fire determines the actual volumes of PAHs discharged into the atmosphere. Meteorological conditions such as wind speeds, temperature and humidity; fuel type- green wood, dry grass, etc. play a role in the degree and variation of PAHs formed. The data regarding these emissions and their contributions to the overall PAH profile are limited [21]. The intensity of the fire, type of organic material burned, type of fire (heading fire vs. backing fire) and type of blaze (wild vs. prescribed or flaming vs. smouldering) determines the particulates emitted from these sources [26].

The concentrations of PAHs in crude oil, coal and oil shale are high. The low temperature combustion (100-150 °C) of organic matter over millions of years (diagenesis) yields bituminous fossil fuels such as coal and crude oil deposits that contain PAHs naturally. The majority of PAHs formed during this process are the alkylated PAHs, with the occurrence of the unsubstituted parent compounds being low in these sources [27]. Besides petroleum bodies like tar sands, in their natural state, fossil fuels contribute a relatively small portion of PAHs to the environment. Because oil deposits exist deep within the Earth's crust, there is little to no chance of them discharging PAHs to the surface. Tar sands are capable of emitting PAHs into both the atmosphere and aquatic surroundings, however since these deposits are few in number, they

are unlikely to make a notable contribution to the global volume of PAHs present in the environment.

The PAHs contained in crude oil and its refined products are highly complex and vary at different sources. The carbon in coal is largely (70-75%) in aromatic form with the six-membered ring aromatics in greater proportion than the five-membered ring fraction. Benz[*a*]anthracene, benzo[*a*]pyrene, dibenzo[*c,d,m*]pyrene, perylene and phenanthrene were identified in coal samples; with naphthalene, phenanthrene detected at levels greater than 10 µg/L and anthracene, benzo[*k*]fluoranthene and dibenzo[*a,h*]anthracene levels were lower than 10 µg/L [28].

2.2.2.2 Anthropogenic Sources

One of the major anthropogenic sources of environmental PAHs, results from the incomplete combustion of organic matter at elevated temperatures. Typical sources of PAHs are the burning of fossil fuels; a typical example being benzo[*a*]pyrene found in vehicle exhaust, furnaces and electrical generators also burn fossil fuels and produce liquid, solid and gaseous wastes that are potentially PAH rich. The production of refined products and hydrocarbon fuels via the catalysis of crude petroleum results in the production of PAHs. Coke is a solid carbon-rich fuel made from the destructive distillation of low-ash, low-sulphur bituminous coal. Its production involves the distillation of coal at high temperatures (~1400 ^{o}C) in a reducing atmosphere; these are perfect conditions for pyrosynthesis of PAHs. Coal tars also contain a variety of PAHs which either originate from the PAHs already present in the coal initially used for production or from the pyrolysis of coal carbons. Another major source of PAHs into the environment, is waste incineration; with PAHs present in the stack gases, solid residues and municipal wastewater and effluent. The ubiquity of PAHs is a direct result of the fact that industrial and domestic processes involve the subjection of large quantities of carbon materials to high temperatures on a

daily basis [29]. Other sources of PAHs as a result of human activity include petroleum and oil spills into water bodies and industrial effluents.

2.2.4 Uses of PAHs

Of the vast number of polyarenes, a few of them are used as intermediate substances in the pharmaceutical, photographic and chemical industries. Naphthalene is used in the production of phthalic anhydride, carbaryl insecticide, beta-naphthol, leather tanning agents, moth repellent and surfactants. Acenaphthene is used as an intermediary in pharmaceutical and photographic industries; and to a limited extent, in the production of soaps, dyes, insecticides, fungicides, plastics and food processing. Anthracene is used as a diluent for wood preserves and an intermediary for dyes. Quinoline is a heterocyclic member of the PAHs, also found in coal tar and present in small amounts in virgin diesel. It is used mainly as an intermediate in the manufacture of hydroxyquinoline sulphate, niacin, dyes, decarboxylation catalysing agent, as a solvent for resins and terpene [29]. Figure 2.1 below shows the structures of the sixteen priority polycyclic aromatic hydrocarbons as listed by the US EPA and WHO priority pollutants.

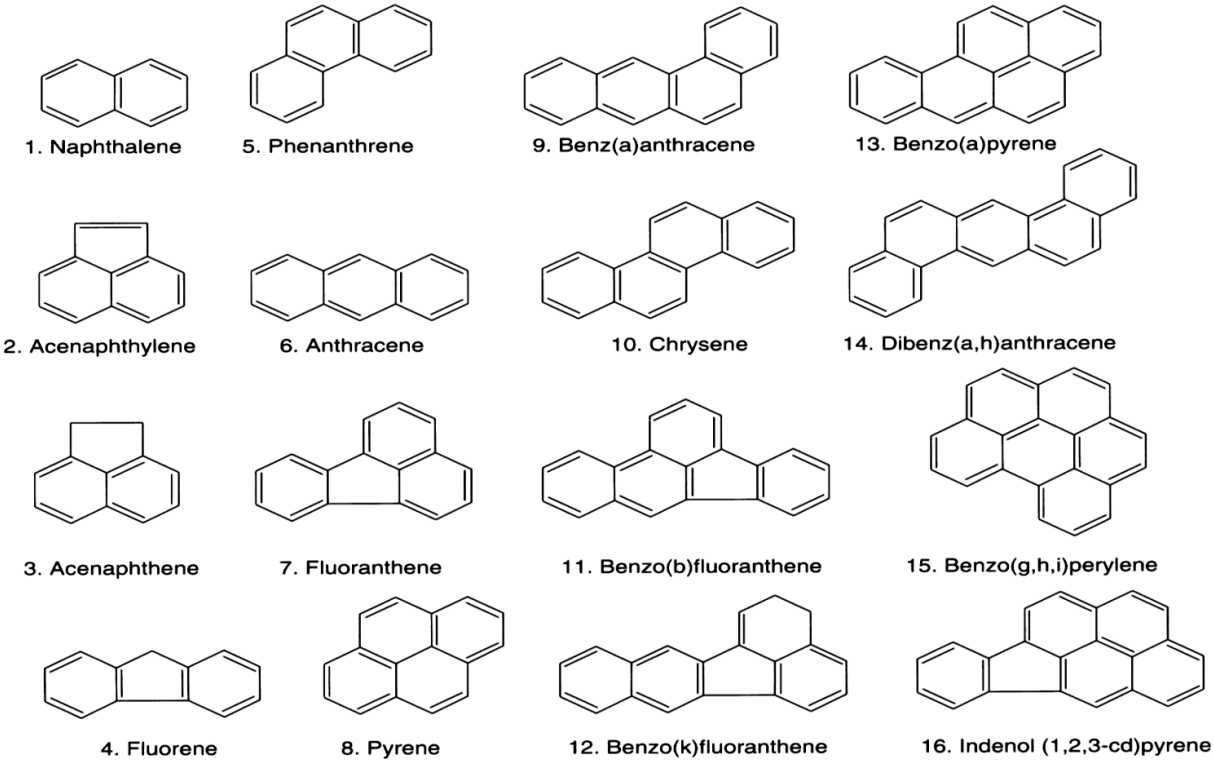

Figure 2.1: Structures of the sixteen priority polycyclic aromatic hydrocarbons as listed by the US EPA and WHO priority pollutants.

2.2.5 Exposure and Health Effects of PAHS

It was in 1775 that British surgeon Sir Percival Pott observed that scrotal cancer in chimney sweeps originated from occupational exposure to soot [30]. A century later, von Volkman reported elevated incidences of skin cancers in individuals working in coal tar industries. It was in the early 1900s that soot, coal tar and pitch are carcinogenic to humans. (Dipple 1985; IARC 1983, 1984a,b, 1985). Experiments conducted on animals showed that the carcinogenic activity of PAHs in vehicle exhaust fumes is associated mainly with the fraction containing compounds composed of four to seven aromatic rings [31, 32] [33]. That is to say that as the molecular weight increases, the carcinogenicity of the PAH also increases, and acute toxicity decreases. Benzo[a]pyrene is the first chemical carcinogen to be discovered. The International Agency for Research on Cancer (IARC) considers several PAHs and their derivatives to be possible human

carcinogens (Table 2.2); the PAHs most known for their severe mutagenic properties are benz[a]anthracene and chrysene ($C_{18}H_{12}$); benzo[b]fluor anthene, benzo[j]fluoranthene, benzo[k]fluoranthene and benzo[a]pyrene ($C_{20}H_{12}$); indeno[1,2,3-cd]pyrene ($C_{22}H_{12}$); and dibenz[a,h]anthracene ($C_{20}H_{14}$) [34].

PAHs are present in all environmental media (air, soil and water). Despite the fact that exposure to PAHs is primarily through the ingestion of contaminated food products, the inhalation of non-occupational polluted air is a growing concern, especially in places with a high population density and the increased rate of industrialization that usually follows. It has been found that the non-occupational levels of PAH exposure are as high as 440 ng/m^3 depending on the location of the study, sampling sites, sampling season, the phase investigated and the number of PAHs measured [35].

The lipophilicity of PAHs means that they are lipid soluble and thus can be absorbed through the epidermis, respiratory and gastrointestinal tract. Upon absorption, PAHs enter the interstitial fluid between the cells, circulate in the blood and are metabolized primarily in the liver and kidney. PAHs differ with respect to distribution patterns and lipophilic properties [36]. Their lipophilic nature allows them to accumulate in breast milk and fatty tissue. However, the liver and kidney are relatively efficient at the excretion of PAHs, this is as a result of the wide distribution of enzymes that transform PAHs into polar metabolites. The hydroxylated metabolites of the PAHs are ultimately excreted in human urine as both free hydroxylated metabolites and as hydroxylated metabolites conjugated to glucuronic acid and sulphate (CDC, 2005).

The toxicity of PAHs stems from the fact that they are potent mutagens, carcinogens and endocrine disrupting substances. PAHs reveal their toxicity following biotransformation to toxic metabolites which can be bound covalently to cellular macromolecules such as DNA, RNA and pro-

teins, which causes cell damage, mutagenesis, teratogenesis and carcinogenesis. After PAH exposure, there is an increase in the number of DNA adducts, as well as some inhibition in RNA and protein synthesis [37, 38]. In recent years it has been found that PAHs have potential as potent neurotoxins. Residents living near dumping sites in Texas and a waste oil processing plant in California were reported to show neurological symptoms [39]. Niu *et al.* (2010) found that the exposure of coke oven workers to B[a]P induced alterations in both emotional and cognitive functions. It was found that the coke oven workers' neurobehavioural function and monoamine, amino acid and choline neurotransmitter levels were reduced [40].

Table 2.2: Carcinogenic classification of PAHs by IARC [38]

Poly aromatic hydrocarbon	Carcinogenic classification
benz[a]anthracene benzo[a]pyrene	Probably carcinogenic to humans
benzo[a]fluoaranthene benzo[k]fluoranthene indeno[1,2,3-cd]pyrene	Possibly carcinogenic to humans
anthracene benzo[e]pyrene chrysene fluoranthene fluorene phenanthrene pyrene	Not classifiable as to their carcinogenicity to humans.

The data available on the uptake of PAHs by terrestrial vertebrates is sparse, however, based on the fact that PAHs are omnipresent in the environment (WHO, 1998) and have been detected in tissues and eggs, it can therefore be concluded that PAHs do in fact occur in free-living vertebrate species, with the dominant route of exposure being via diet. Although, topical exposure must be considered in some instances where incubating birds become oiled and oils is transferred from feathers to the egg shell. The result is embryos being exposed in vivo. Ma *et al. (*1995*)* conducted a study on the uptake of specific PAHs by earthworms- a major food for

most invertebrate-feeding birds and mammals. It was found that fluoranthene and to a lesser degree, phenanthrene were found to be bio accumulated in the earthworms that had been exposed to contaminated soil. Bioaccumulation factors seemed higher in the first two weeks of exposure- worms exposed to 100 mg/kg fluoranthene ranged from 0.022 to 0.623 [41].

Further up in the food chain, bioaccumulation was limited because PAHs induce and are rapidly metabolized by mixed function oxidases. The rapid metabolism of PAHs by birds, for example, means that residues are often not detected in organs and tissues, but PAHs have been detected in some bird species such as herring gulls from two sites in Ontario, Canada at concentrations (μg/kg lipid) of anthracene (0.15), fluoranthene (0.082), pyrene (0.076), naphthalene (0.05), fluorine (0.044), acenaphthene (0.038) and benzo[a]pyrene (0.038) [42]. Peakall *et.al.*1982 [43] found that herring gull nestlings given a single oral dose of Prudhoe Bay crude oil and its aromatic fractions had retarded growth and an increase in adrenal and nasal gland weight within eight days of exposure. The high-molecular weight aromatic compounds produced the greatest effect. The fraction contained a methylated series of chrysenes, benzanthracenes, phenylanthracenes, binaphthyls, and traces of benzopyrenes. However, growth rates were not suppressed following exposure to the fraction containing alkylated naphthalenes, biphenyls, anthracenes, phenanthrenes, and fluorenes [43].

PAHs are endocrine disrupting substances. They cause reproductive toxicity in birds, which is a result of the changes in estrogens. Chronic administration of BaP resulted in complete infertility in female birds, associated with grossly visible changes in the appearance of the ovaries. The results indicated that long-term dosing with BaP alters ovarian structure and function in treated birds and simultaneously aggravated the development of arterial lesions. The BaP-induced atherogenicity in female pigeons could be a consequence of an alteration in estrogen production or of antiestrogenic properties of BaP at the level of the arterial wall [44].

There have been studies conducted on the exposure of PAHs to terrestrial mammals. A variety of PAHs have been found in the livers and kidneys of mammals from areas known to be contaminated with oil. Deer mice from South Carolina and New Jersey, USA were found to have eleven PAHs in their livers, with concentrations ranging from from 0.05 mg/kg for benzo[b]fluoranthene to 4.56 mg/kg for benz[a]anthracene. Although, below the limit of detection, other PAHs detected at (mg/kg) were acenaphthylene (1.91–3.92 mg/kg), acenaphthene (0.10–0.14 mg/kg), fluorine (0.22–0.34 mg/kg), benz[a]anthracene (0.55–4.56 mg/kg), chrysene (0.01–0.32 mg/kg), benzo[b]fluoranthene (0.05–2.64 mg/kg), benzo[k]fluoranthene (0.05–0.07 mg/kg), dibenz[ah]anthracene and indeno[1,2,3–cd]pyrene [45]. PAHs have been found to suppress immune function- as measured by the formation of antibodies. PAH mediated toxicity is indicated by the presence of DNA adducts, and high levels of DNA adduct are associated with increased carcinogenicity. However, that increased concentrations of adducts have been reported in wild mammals, there are limited studies that link adducts with the presence of tumours in free-living mammals [46].

Despite the fact that there are relatively few studies on the exposure to and effects of PAHs in free-living terrestrial and aquatic vertebrates, it is clear that exposure does occur. The studies conducted show that although PAHs are lipophilic, their rapid metabolism by wild vertebrates means that they do not necessarily accumulate to high concentrations. The increased risk of carcinogenicity associated with the formation of adducts in free-living adult wild birds and mammals are the primary toxic effect of exposure to PAHs. The potential ecological significance is in long-living species, where long-term survival, lifetime productivity and success can be affected because PAH exposure has potentially immunosuppressive effects which compromise the ability of adult birds and mammals to withstand environmental stressors such as disease [47].

2.2.6 Fate of Poly Aromatic Hydrocarbons in the Environment

The demonstrated biological effects of PAHs, including acute toxicity, carcinogenicity, mutagenicity, teratogenicity and endocrine disrupting activity dictate the importance of understanding the environmental fate of PAHs. A fundamental step in understanding the fate of pollutants in the environment is tracking their migration through the global environment. It was in 1974 that Rappe suggested that persistent organic pollutants migrate through the atmosphere as gases and aerosols and condense in cold regions [48]. Wania *et al.,*1996 proposed that a global distillation and cold condensation process occurs, where different POPs are deposited in different regions during transit from the point of release towards the North and South Poles. The idea of global fractionation between air, water and soil at ordinary environmental temperatures is consistent with the thermodynamic properties of the compounds involved. The phenomenon is pronounced for POPs of intermediate volatility (volatile enough to evaporate upon release in temperate and tropical latitudes, but whose volatility decreases at colder polar temperatures to cause substantial deposition and partitioning to aquatic and terrestrial media). Thus warm temperatures favour evaporation in tropical and subtropical regions, and cooler temperatures, at high latitudes favour deposition onto soil and water [49]. Furthermore, there are other factors outside of the compounds' thermodynamic properties that prescribe POPs inclination to condense, deposit and accumulate. For example, upon release, PAHs are in the gas phase. Cold temperatures favour adsorption of these substances by condensation or nucleation to particles already present in the atmosphere to form particulate matter, which will ultimately deposit on the surface. Another factor is the natural degradation reactions that slowdown in cold regions, thus allowing POPs to remain intact and in this way, persist. In the same light, cool temperatures prevent the vaporisation of POPs from aquatic systems and promote their condensation and nucleation and the resultant partitioning as particulate phase from the atmosphere to the surface [50].

An estimated 230 000 metric tons of PAHs enter the global environment on an annual basis. The sources are petroleum spills, direct discharge of effluent and waste water from industries and domestic sources, aerial and terrestrial vehicle exhaust fumes and biosynthesis or the slow maturation of organic matter. Upon release, PAHs are more concentrated near densely populated urban areas. Their fate in the environment is largely determined by their physicochemical properties, particularly nonpolarity which is responsible for their lipophilicity and hydrophobicity which are the cause for persistence in the environment [51, 52].

Of the PAHs deposited on the soil, those that are deposited directly on soil or vegetation are likely adsorbed or assimilated by plant leaves and thus entering the animal food chain. For PAHs assimilated by plants, one of two scenarios are likely: the PAHs assimilated by plants may be metabolized and photo-degraded within the plant or for plants growing in areas with high concentrations of PAHs, assimilation exceeds metabolism and degradation, resulting in a situation in which these substances have accumulated in plant tissues [53, 54].

In water, PAHs will either evaporate and return to the atmosphere or descend down the water column. However, the low solubility in water and hydrophobicity of PAHs means that they become rapidly associated with organic and inorganic suspended particles and subsequently settle in sediment at the bottom of water bodies, concentrate in the aquatic biota or undergo photooxidation and biodegradation [55]. Photooxidation and biological transformation by bacteria and aquatic animals are probably the most important decomposition processes in aquatic systems. A large portion of PAHs in aquatic environments are associated with particulate matter and about one third exist in dissolved form. It is these PAHs that exist in the solvated form that will degrade rapidly through photolysis at elevated temperatures and oxygen levels, especially where there is a greater incidence of solar radiation. Those that settle into sediment will ultimately undergo biotransformation and be degraded by benthic organisms.

The PAHs that accumulate in sediments at the bottom of water bodies degrade much more slowly because there is little to no sunlight and oxygen penetrating and thus they will persist for much longer in the oxygen poor sediments [24, 55, 56].

2.3 METAL OXIDES NANOPARTICLES

Application of Metal-oxide nanomaterials in sensor applications is very promising due to the fact that metal-oxides provide robust building blocks, thus they have attracted an increasing amount of technological and industrial interest.

2.3.1 Nickel Oxide (NiO_x) Nanoparticles

Among the transition metal oxide semiconductors, Nickel oxide (NiO) is a p-type semiconductor with a wide band-gap of ~3.7eV at room temperature. It has been investigated for various applications such as energy storage: solar cells, Li^+ ion batteries; electronics applications such as resistive random access memory (RRAM), light emitting diodes (LEDs); analytical chemistry: electrochemical sensors and biosensors [57-61].

Nickel oxide (NiO) nanoparticles have been used by researchers to modify electrodes in combination with various other materials such as graphene, multi-walled carbon nanotubes (MWCNT), ethynylferrocene, carbon paste, metals and mixed metal oxides. However it has been found that many of these applications are either for energy storage- supercapacitor studies [18, 62] and for the electrochemical studies of biomolecules [63]. It was in the early 1970s that Pletcher showed that organic compounds could be partially oxidized over nickel, silver copper and cobalt electrodes covered by their respective oxides [64, 65]. The most intensive studies using NiO nanoparticles for the modification of electrodes and sensor

fabrication has been for the determination of small carbohydrate molecules- especially glucose and some amino acids because NiO is an effective electro-catalyst for biomolecules [66-68].

NiO nanoparticles are an attractive material for application as an electrode modifier and electro-catalyst because of their cost effectiveness, ease of synthesis and high electrocatalytic activity. Research reveals that the electrochemical performance of transition metal oxides is influenced by their microstructures; this results in a dominating kinetic feature involving ion and electron transport in electrodes and at the interface between the electrode and the electrolyte [69].

2.3.2 Cobalt Oxide (Co_3O_4) Nanoparticles

Cobalt oxide nanopowder is a transition metal oxide with a cubic spinel structure in which the Co^{2+} ions occupy the tetrahedral sites and the Co^{3+} ions, the octahedral sites. It has attracted attention because of its outstanding multifunctional physicochemical properties. It is an important antiferromagnetic p-type semiconductor. It is these excellent properties that have allowed Co_3O_4 to find use in lithium ion battery, magnetic storage media, gas sensor, catalysis and electrochemical applications [70-72].

Cobalt oxide based nanocomposites have demonstrated great potential in the applications of electrochemical sensor and supercapacitor [17, 18].

The complex metal oxide spinel structure, despite its difficulties in achieving a high surface area and low resistivity, look very promising as electro-catalysts, because they are relatively cheap, chemically active and thermodynamically stable [73]. Cobalt oxide nanoparticles has been used to modify glassy carbon electrode for the voltammetric nanomolar detection of hydrogen peroxide as well as toxic arsenic(III) nitrite and in the catalysis of various compounds such as ozone and oxygen evolution [74-76].

2.4 GRAPHENE OXIDE (GO) AND MULTI-WALLED CARBON NANOTUBES (MWCNTS)

Graphene is a two dimensional carbon-based nanomaterial made of a single layer of sp^2 hybridized carbon. It is one of the allotropes of elemental carbon. The monoatomic layer of carbon atoms are arranged in a hexagonal (honeycomb) lattice with a carbon-carbon bond-length of ~0.142 nm.s [77]. Graphene electrons are delocalized around the planar structure, which contributes to its various interesting properties such as high charge mobility, remarkable thermal conductivity, superior mechanical tensile strength and a large surface area.

Graphene has a zero band gap which makes it a semi conductive material that finds use in many electronic applications. Graphene has found use in applications such as energy storage devices- solar cells, lithium batteries and supercapacitors, conducting electrodes and gas sensors [78] .

Graphene oxide, however, is also a monolayer material produced by the exfoliation of graphitic oxide, where graphite oxide is synthesised through the chemical oxidation of graphite using any number of oxidants, including concentrated sulphuric, nitric, phosphorous acids and or potassium permanganate based on the Hummers method [79]. Unlike pristine graphite, graphitic oxide is heavily oxygenated and bears, in addition to the carbonyl and carboxyl groups located at the sp^2 hybridized carbon on the edge plane sites, hydroxyl and epoxy groups on the sp^3 hybridized carbons on the basal plane. This abundance of oxygen containing functional groups, affords graphite oxide hydrophilicity and thus allows it to be easily exfoliated to form stable dispersions in aqueous media, consisting mostly of single to few layer sheets (graphene oxide).

Carbon has a wide range of allotropes in different dimensions. For example, Fullerene is the zero dimension (0D) form. It is a fairly large molecule of 60 carbon atoms bound in icosahedron geometry to form a sphere. In one dimension, carbon atoms arrange themselves as single-

walled carbon nanotubes. These consist of a piece of graphene rolled in on in on itself to form a cylinder. They are well-ordered hollow graphitic cylinders made of sp^2 hybridized carbon atoms. Multi-walled carbon nanotubes are made from sheets of graphene rolled into a cylinder to form numerous concentric tubes that share a common longitudinal axis [80].

The high aspect ratios, high mechanical strength, high surface areas excellent chemical and thermal stability intense electronic and optical properties of graphene and multi-walled carbon nanotubes, make them important transducer materials in electrochemical sensors, gas detection, transparent conducting electrodes, composites and energy storage devices such as supercapacitor and lithium ion batteries. Decreasing the size of graphene oxide into narrow ribbons generates a band gap and confers semiconductor properties for application in transistors. An interesting property of graphene oxide is its capacity for charge carriage. By removing oxidized and amorphous carbon groups that make GO insulating, it can be made to electrically conducting [78]. It has been found that graphene and carbon nanotubes exhibit higher electronic properties and device performance and have potential as an alternative for future electronics [80]. Based on this, it is worth comparing the electrochemical behaviour of these carbon nanomaterials in an environmental application.

2.5 CHEMICALLY MODIFIED ELECTRODES FOR POLLUTANTS DETECTION

The purpose of a chemical sensor is to provide reliable information about the chemical composition of the surrounds. In an ideal situation, this device is able to respond continuously without perturbation of the sample. In the same vein, an electrochemical sensor, the analytical information is in the form of an electrical signal that results from the interaction of the target

analyte and the electrode surface [81]. This is the very basis of electrochemical analysis: the reaction on an electrode surface.

In order to impart a high degree of selectivity and sensitivity to electrochemical transducers, chemical layers or substrates can be used. An electrode can be modified by the immobilization of substrates that change the electrochemical characteristics of the bare surface. Depending on the application, any number of substrates can be used such as noble metals, carbon, semiconducting materials and composites - have excellent characteristics as a result of the synergy of the combined materials.

Ideally a sensor has characteristics such as specificity for the target analyte, sensitivity to changes in target analyte species concentration, fast response time, extended lifetime of several months and low cost manufacture.

Nanomaterial modified electrodes are proving to have advantages compared with their bulk substrate counterparts. The reason for this is that nanomaterials offer a huge specific area that allows for the immobilization of more functional molecules on the electrodes. Nanoscale semiconductor materials may act as promoters of electrochemical communications. This is achieved when the substrate mediates electron transfer between the target analyte and the surface.

In as far as environmental protection and pollution control go there has been progress made as a result of the combination of nanotechnology and breakthroughs in electrochemical techniques. This has allowed the introduction of powerful reliable devices used in pollution control and environmental monitoring.

The sensing ability of nanoparticles is directly related to their ability to catalyse the oxidation/reduction reaction of the target analyte by increasing the rate of electron transfer

and thus the reaction taking place at lower operating potentials. Various catalytic surfaces have been used for facilitating the detection of environmentally relevant analytes [10]. Recently we reported on the sensing ability of Prussian blue (PB) and Fe_2O_3 nanoparticles doped graphene oxide towards two environmentally relevant analytes, *viz.* nitrite and nitric oxide [82], and it was found that the sensor compared favourably with values reported in other studies: LoD ~ 6.60 µM and 13.04 µM for NO_2^- and NO^- on the Pt-GO-Fe_2O_3; and 16.58 µM (NO_2^-) and 16.50 µM (NO^-) on the Pt.-GO-PB electrode.

Other studies on the detection of persistent organic pollutants by Tovide.*et.al* [83] , Mailu.*et.al*[84] and Rassie.*et.*al [85] were conducted using graphenated polyaniline tungsten oxide nanocomposite, Silver-Gold alloy NPs- overoxidized polypyrrole and dendritic polythiophene composite sensors for the detection of phenanthrene and anthracene. They obtained LoD values of 0.123 pM, 0.167 µM and 19 nM.

2.6 METHODS OF DETERMINING PERSISTENT ORGANIC POLLUTANTS

Many methods have been put forward for the determination of POPs. Commonly employed techniques for the determination of POPs are based on phosphorimetry methods [86] and chromatographic techniques such as Gas chromatography (GC) coupled with high resolution mass spectrometry (HRMS)[87] and high performance liquid chromatography coupled to different types of detectors such as photodiode array (HPLC-PDA) [88], electron capture detector (ECD) [89].

Despite the fact that chromatography based methods have high accuracy and low detection limits, they present a significant problem in many instances where capacity and funds are limited because they require sample preparation step prior to detection- this is time consuming

and tedious. Other techniques for the detection and determination of POPs include Surface Plasmon Resonance (SPR), where the enhancement of the SPR effect of noble metals has been used for the trace detection of POPs [90]. The detection using SPR presents high sensitivity with reduced measurement time, however using SPR to detect trace POPs and heavy metals is difficult because it is critical to enhance the SPR signal. Another sophisticated technique that has shown great potential as an analytical technique for the detection of POPs, has been used for the trace-level detection of PCBs, is Surface Enhanced Raman Spectroscopy (SERS). SERS shows promise as an analytical technique, because of the unique molecular signals presented by structurally similar analyte species and the minimal interference of scattering from water when sampling in aquatic environments [91].

Fluorescent detection has been used in bio sensing, primarily because it can be carried out with an ordinary spectrofluorometer and the limits of detection can be fairly low. Recently, the method has been applied for the detection of pollutants in water. However, because the intrinsic fluorescence of certain pollutants is weak and organic pollutant molecules exact stringent requirements on the optical systems, there is a need for the development of new methods for the detection of POPs [92].

Presently, instrumental methods of analysis are heavily relied upon for the determination, detection and degradation of POPs. However, the major setback with instrumental techniques is the fact that they are expensive, and are not easily amenable to site applications; in most instances they require extensive pre-treatment sample preparation prior to analyte quantification. Most instrumental techniques have long measurement times and complicated operation and do not indicate whether target analytes are accessible for uptake by living organisms. The health risks posed by POPs require the development of a much simpler, rapid,

low cost, robust and reliable method for their detection. Electrochemical method provides simple and low cost analytical procedures for the detection and quantification of POPs.

2.6.1 Electrochemical methods

Electrochemical analysis is a powerful technique that has found utility in the metal, pharmaceutical, food and beverage industries as well as environmental applications. Electroanalysis offers multiple advantages such as high sensitivity, selectivity, rapid analysis times, reduction in solvent and sample consumption as well as ease of use and low operating costs [16] . Based on this, electrochemical methods are considered very promising techniques in the endeavour for environmental monitoring and protection. It was after the development of increasingly sensitive pulse methods, that electroanalytical methods found use in studies involving industrial and environmental applications as well as drug analysis.

There are only three basic electrochemical signals used in electrochemical techniques: potential, current or charge; these serve as the analytical signal. Electrochemical techniques are broadly divided into two categories: bulk techniques, which deal with the property of a solution in a cell; and interfacial techniques, in which the potential, charge or current depends on the species present at the interface between an electrode and the solution at which it sits. Interfacial techniques are those applied in detection and determination. These are generally based on the concept of continuously changing the applied potentials to the electrode-solution interface and measuring the resulting current.

In most electrochemical techniques, there are three electrodes – the working electrode, the reference electrode and the counter (or auxiliary) electrode. The three electrodes are connected to a potentiostat, an instrument which controls the potential of the working electrode and measures the resulting current. In one typical electrochemical experiment, a potential is applied to the working electrode and the resulting current measured then plotted

versus time. In another, the potential is varied and the resulting current is plotted versus the applied potential.

Electroanalytical methods have also shown certain advantages over other analytical methods. Because electrochemical analysis allows for the determination of different oxidation states of a compound in a solution and not just the concentration of the compound, an abundance of information can be obtained, including electron transfer and chemical kinetics, and the elucidation of reaction mechanisms. Electroanalytical techniques are also capable of producing exceptionally low limits of detection. The other important advantage of this method is its low cost and robustness.

CHAPTER 3

EXPERIMENTAL

3.1 MATERIALS AND REAGENTS

Pristine multi-walled carbon nanotubes (95% purity, 10-20 nm); natural graphite flakes and the salts of the metals, nickel chloride hexahydrate ($NiCl_2.6H_2O$); cobalt nitrate hexahydrate ($Co(NO_3)_2.6H_2O$), ammonium carbonate ($(NH_4)_2CO_3$); hydrated potassium hexacyano ferrite(II) ($K_4[Fe(CN)_6].3H_2O$) and potassium hexacyano ferrate(III) ($K_3Fe(CN)_6{\cdot}6H_2O$); are purchased from Sigma-Aldrich. Potassium chloride (KCl); acetone (C_3H_3O); ethanol (C_2H_5OH); isopropyl alcohol (C_3H_7OH); sulphuric acid (H_2SO_4); phosphoric acid (H_3PO_4); nitric acid (HNO_3); hydrochloric acid (HCl); hydrazinium hydroxide (N_2H_5OH); ammonia solution ($NH_3{\cdot}H_2O$); sodium nitrate ($NaNO_3$); potassium permanganate ($KMnO_4$); 30% hydrogen peroxide (H_2O_2) and other reagents were of analytical grade and obtained from Sigma-Aldrich and Merck chemicals respectively.

Ultra-pure water of resistivity 18.2 MΩcm was obtained from a Milli-Q Water System (Millipore Corp., Bedford, MA, USA) and was used throughout for the preparation of solutions. 0.1 M phosphate buffer (PBS) pH 7.0 was prepared using sodium hydrogen phosphate di-hydrate ($NaH_2PO_4.2H_2O$) and di-sodium hydrogen phosphate di-hydrate ($Na_2HPO_4.2H_2O$) or their potassium salts. The pH was adjusted with 0.1 M H_3PO_4 or NaOH. All solutions were prepared using double distilled deionised water and purged with pure nitrogen to eliminate oxygen and any form of external oxidation during experiment. All other reagents were of analytical grades and were used as received from the suppliers without further purification. Electrochemical experiments were performed with nitrogen-saturated 0.1M PBS and 1M HCl as supporting electrolytes.

Glassy carbon electrode (3 mm diameter) was purchased from CH Instruments USA. Polishing pads were obtained from Buehler, IL, USA and Alumina micro powder (1.0, 0.3 and 0.05 µm alumina slurries) was used for polishing the glassy carbon electrode (GCE).

3.2 PREPARATION OF MATERIALS

3.2.1 Synthesis of Graphene Oxide

Graphene oxide was synthesised using the modified Hummer's Method [79, 93]. Typically, 60 mL concentrated sulphuric acid was added to 2.5 g of graphite flakes mixed with 1.25 g sodium nitrate and were mixed in a 250 mL flask and stirred for 30 minutes in an ice bath. About 7.5 g of potassium permanganate was slowly added to the suspension with the reaction mixture kept below 10 ^{0}C. It was important to maintain the rate of addition in order to prevent the reaction mixture from exceeding 10 ^{0}C. The suspension was removed from the ice bath and vigorously agitated overnight at room temperature. About 75 mL of deionised water was added and stirred at 98 ^{0}C for a day. The mixture was observed to gradually thicken with lessening effervescence. The slurry was allowed to cool, followed by quenching with excessive amounts of deionised water and 30 mL of a 25% hydrogen peroxide solution was added to the mixture to reduce residual potassium permanganate and manganese dioxide to the colourless manganese sulphate. The solution was filtered and washed with 800 mL of 5% hydrochloric acid /deionised water to remove residual metal and sulphate ions. The filtrate was dried in an oven at 60 ^{o}C for 24 hours to obtain graphene oxide.

3.2.2 Synthesis of Funtionalised MWCNTs

The pristine MWCNTs were purified and functionalised with acid functional groups (CNT-COOH) according to reported procedure [94-96], by refluxing a known weight of the MWCNTs in 2.6 M HNO_3 for 48 hours, after which the slurry was diluted in water and filtered. The product was washed with copious amount of water until the pH of the MWCNT slurry became neutral, and subsequently centrifuged. The product was dried in an oven at ~ 40 ^{o}C. The residue was ultrasonicated at 40 ^{0}C in a mixture of concentrated H_2SO_4 and HNO_3 (3:1, v/v) for 24 h. The

material was filtered again, washed with copious amounts of water and dried. Finally, the suspension was stirred at 70 ^{0}C in a mixture of concentrated H_2SO_4 and 30% aqueous H_2O_2 (4:1, v/v) for 4 hours. The product was filtered and washed with copious amount of water until the pH of the filtrate was neutral. The black solid material obtained was dried in an oven over night and stored in an air-tight container.

3.2.3 Synthesis of Nickel Oxide Nanoparticles

Nickel (II) oxide (NiO) nanoparticles were prepared using the method described by Xiang *et al*. [97] Briefly, 100 mL of precipitation solution, ammonium hydrogen carbonate was dropped at the rate of 5.0 mL min $^{-1}$ into 50 mL of 0.5 M nickel (ii) ions solution. During precipitation, the suspension was kept at constant temperature (40 °C), and constant stirring (800 rpm) for 1 hour.

The precipitate formed was washed with distilled water and copious amounts of ethanol several times to remove any adsorbed ions such as NH_4^+, Cl^-, NO_3^-, CO_3^{2-}, and OH^-. The precipitate was oven-dried at 105 ^{o}C for 12 hours, and later heated in air at 400 ^{o}C for 1 hour. The product was pulverised and used for analysis.

3.2.4 Synthesis of Cobalt Oxide Nanoparticles

Cobalt (II, III) oxide nanoparticles were synthesized using the method described by Yao *et al.* [98] About 6.0 g of cobalt (II) nitrate hexahydrate was dissolved in 200 mL isopropyl alcohol-water (1:1 *v/v*) solution in a three-necked round bottom flask. 50 mL of isopropyl alcohol-ammonium hydroxide solution was added to the solution and aged for 6 hours to ensure complete precipitation. The precipitate was filtered under vacuum at 70 ^{0}C. The cobalt oxide was obtained after calcining the cobalt hydroxide precursor at 500 ^{0}C in pure nitrogen gas for 4 hours.

3.2.5 Preparation of Modified electrodes

Electrode modification was achieved using the drop-cast method. Firstly, the glassy carbon electrode was cleaned by gentle polishing in aqueous slurry of alumina nanopowder on a silicon carbide-emery paper followed by a mirror finish on a Buehler felt pad. The electrode was later subjected to ultrasonic vibration in water, and then absolute ethanol to remove residual alumina particles that were trapped on the surface. Separate suspensions of the individual nanomaterials and nanocomposites were prepared by mixing about 5 mg each of the respective carbon nanomaterials (CNM) *viz.* GO or fMWCNT with either of the metal oxide (MO) nanoparticles *viz.* Co_3O_4 or NiO in about 1 mL DMF. About 10 µL drops of the prepared nanocomposite were dropped on the bare GCE and dried in an oven at 50 ^{0}C for 2 minutes to obtain GCE–CNM–MO electrodes. All the procedures involved drop-drying a thin film of the MO, GO, fMWCNT, fMWCNT/MO or GO/MO nanocomposite onto the glassy carbon electrode (GCE) in preparation for analysis. The electro active species surface coverage area of the electrodes was determined in the 5 mM ($[Fe(CN)_6]^{3-/4-}$) redox probe and estimated by using the relationship; Q = nFAΓ [99].

3.3 MEASUREMENTS AND INSTRUMENTATION

The infrared and ultra-violet-visible spectra of the graphite flakes, graphene oxide, multi-walled carbon nanotubes, metal oxides and nanocomposites were obtained using Fourier Transform Infrared spectrophotometer (Agilent Technology, Cary 600 series FTIR spectrometer, USA), and UV-visible spectrophotometer (Agilent Technology, Cary series UV-vis spectrometer, USA). The Raman spectra were obtained using Xplora Horiba Raman Spectrometer (Olympus BX41 microscope, UK). The morphology images of the synthesised carbon nanomaterials and metal

oxide nanoparticles were obtained using transmission electron microscopy (TEM) Tecnai G2 Spirit FEI (USA). High resolution scanning electron microscope (HRSEM) images were obtained using the Zeiss Ultra Plus 55 HRSEM (Germany), while the energy dispersive x-ray spectra (EDX) were obtained from NORAN VANTAGE (USA). The X-ray powder diffraction data were collected on a Röntgen PW3040/60 X'Pert Pro X-ray diffractometer using Ni-filtered Cu Kα radiation (k = 1.5405 A) at room temperature. The samples were identified using X'Pert Highscore plus software. The voltage and current is: 35 KV and 50 mA.

Electrochemical experiments were carried out using an Autolab Potentiostat PGSTAT 302 (Eco Chemie, Utrecht, and The Netherlands) driven by the GPES software version 4.9. Impedimetric spectroscopy (EIS) measurements were performed with Autolab Frequency Response Analyser (FRA) software between 1Hz - 100 kHz using a 5 mV rms sinusoidal modulation with the solution of the analyte at their respective peak potential of oxidation (vs Ag|AgCl in sat'd KCl). A Ag|AgCl in saturated KCl and platinum wire were used as reference and counter electrodes respectively. The FRA software allowed the automatic fitting of the raw EIS data to equivalent circuit models using a non-linear least squares (CNLS) method based on the EQUIVCRT programme [100] *with Krammers-Kronig rule check*. Electrochemical experiments were also carried out in supporting electrolyte solution containing different concentrations of the analytes: Pyrene and Heptachlor respectively. Bare GCE and modified electrodes are used as working electrode. A Ag|AgCl in saturated KCl and platinum wire were used as reference and counter electrodes, respectively. A Crison pH meter, Basic 20+ model, was used for pH measurements. All experiments were performed at 25±1◦C while the solutions were de-aerated with N_2 gas before every electrochemical experiment.

Electrochemical measurements involved the loading (by drop-casting) a thin film of the metal oxide, carbon nanomaterial or metal oxide-carbon nanomaterial nanocomposite onto the

surface of the prepared bare GCE electrode in preparation for analysis. A description of the electrode modification process is discussed *vide infra*.

3.4 CHARACTERISATION

3.4.1 Structural and Morphological Characterisation

The morphologies of graphene oxide, functionalised multi-walled carbon nanotubes, nickel oxide, cobalt oxide, and the various nanocomposites (GO/NiO, GO/Co_3O_4, fMWCNT/NiO and fMWCNT/Co_3O_4) were characterised using FT-IR, UV-Vis, Raman, XRD, EDX, SEM and TEM as previously described in section 3.3 to determine the successful synthesis of the nanoparticles and their composite. The results obtained are discussed in Chapter 4.

3.4.2 Electrochemical Characterisation

The preliminary electrochemical experiments were conducted in order to establish the successful modification of the bare GCE and the GCE modified electrodes. The electrochemical measurement and behaviour (electron transport kinetics) of graphene oxide, functionalised multi-walled carbon nanotubes, nickel oxide, cobalt oxide, and the various nanocomposites (GO/NiO, GO/Co_3O_4, fMWCNT/NiO and fMWCNT/Co_3O_4) modified electrodes were studied in a phosphate buffer (PBS) solution (pH 7) and a solution containing an outer-sphere redox probe 5 mM $[Fe(CN)_6]^{3-}/[Fe(CN)_6]^{4-}$ using cyclic voltammetry (CV) and electrochemical impedance spectroscopy (EIS). Bare and modified GCE electrodes were used as the working electrode. Ag|AgCl, sat'd KCl and platinum electrodes were employed as reference and counter electrodes respectively. The results obtained are discussed in Chapter 4.

3.4.2.1 Cyclic Voltammetry (CV)

Cyclic voltammetry **(**CV) experiments were done by running the bare and the modified electrodes first in the PBS solution, and repeated in the $[Fe(CN)_6]^{3-}/[Fe(CN)_6]^{4-}$ redox probe within the potential window of -0.2 to 1.2 V at a scan rate of 25 mV/s. From the voltammograms obtained, the peak current (Ip), peak potential (Ep), formal potential ($E^{o'}$) ΔE, and Ip_a/Ip_c for the electrodes were determined and these parameters provided insight into the electron transport properties of the respective electrodes.

3.4.2.2 Electrochemical Impedance Spectroscopy

The EIS experiment was conducted by running the bare GCE and the modified electrodes in the PBS, and repeated in the $[Fe(CN)_6]^{3-}/[Fe(CN)_6]^{4-}$ solution ($E_{1/2}$ 0.2 V vs. Ag|AgCl in sat'd KCl) between 100 kHz and 0.1 Hz using a 5 mV rms sinusoidal modulation. The results were plotted in the form of Nyquist plots. The charge transfer resistance (R_{ct}) which controls the electron transfer kinetics of the redox probe at the electrode interface is determined from the EIS fitting. The results obtained are discussed in Chapter 4.

3.5 ELECTROCATALYTIC AND ELECTROANALYTICAL STUDIES

3.5.1 Electrocatalytic Procedure

Experiments for electrocatalytic oxidation of Pyrene was carried out using N_2 purged 1M HCl solution. For example, a Pyrene stock solution of 0.005 M was prepared by dissolving 0.05056 g in 50 cm^3 of ethanol:water (80:20) and diluted to the required concentration using 1M HCl as the supporting electrolyte. The cyclic voltammetry experiment was performed over the potential range of 0.0 V and +2.0 V to monitor the electrocatalytic oxidation of Pyrene using the

modified electrode. A comparative study of the electrocatalytic behaviour of the different modified electrodes towards the analyte was investigated. From the CV experiments, electrochemical parameters such as peak current (Ip), peak potential (Ep), E and formal potential ($E^{o'}$) were measured and discussed. In each instance, the bare or modified electrode is the working electrode while Ag|AgCl, sat'd KCl and platinum electrodes are the reference and counter electrodes respectively. EIS experiment was done by fixing the peak potential (E_p) at which the analyte was best catalysed (vs Ag|AgCl, sat'd KCl) or its half potential ($E_{1/2}$) especially for a reversible electrocatalytic process. The results obtained were discussed in Chapter 4.

3.5.1.1 Electrochemical Impedance Spectroscopy

The EIS experiment was conducted by running the bare GCE and the modified electrodes in 16 x 10^{-9} M Pyrene solution ($E_{1/2}$ 1.3 V vs. Ag|AgCl in sat'd KCl) between 100 kHz and 0.1 Hz using a 5 mV rms sinusoidal modulation. The results were plotted in the form of Nyquist plots. The charge transfer resistance (R_{ct}) which controls the electron transfer kinetics of the analyte at the electrode interface is determined from the EIS fitting. The results obtained were discussed in Chapter 4.

3.5.2 Electroanalysis Procedure

3.5.2.1 Effect of Scan Rate

The effect of scan rate (5 - 1000 mVs^{-1}) on the electrode kinetics during analyte oxidation was investigated using the best electrode from the electrocatalytic experiment. Several kinetic parameters such as E_p, I_p, the peak-to-peak separation (ΔE_p) were obtained. The plot of the anodic peak current (I_{pa}) against square root of scan rate ($v^{1/2}$) was determined and the result obtained discussed in Chapter 4.

3.5.2.2 Concentration Study

A stock solution of 5 x 10^{-3} M of Pyrene was prepared by dissolving 0.05056g in 50 mL of ethanol /water (80:20 v/v). A series of solutions were prepared from the stock solution in order to obtain 1.0 x 10^{-9} – 1.0 x 10^{-7} M using 1 M HCl as the supporting electrolyte.

For the electrocatalytic oxidation of Pyrene, 25 mL solution of the prepared series solution was poured into the electrochemical cell consisting of the fMWCNT-Co_3O_4 nanocomposite modified glassy carbon as the working electrode, platinum counter electrode and Ag/AgCl (sat'd KCl) reference electrode. The solution was degassed with nitrogen for 10 minutes before the experiment.

Cyclic voltammetry characterisation of the modified electrode was carried out at scan rate of 25 mV/s in a potential window of 0.0 V to final potential 2.0 V. The response in the absence and presence of Pyrene was monitored. The solution was stirred for 5 minutes after each addition of serial solution of Pyrene. The change in the catalytic current as well as the potential at which oxidation occurred was then monitored after every addition of each analyte.

CHAPTER 4

RESULTS AND DISCUSSION

4.1 Spectroscopic and Microscopic Characterisation

4.1.1 Spectroscopic Characterisation

(a) Fourier Transform Infrared (FT-IR) spectroscopy is an invaluable technique for structure determination and verification. It is a well-established technique that uses infrared radiation. As a characterisation tool, it is used to identify compounds and elucidate sample composition and structure.

Infrared spectroscopy uses the fact that molecules have specific vibrational frequencies at which they vibrate that correspond to discrete energy levels. This makes IR spectroscopy an ideal technique for nanoscale characterization: it is able to measure which bonds are in a material, and subsequently yield important insight about surface functionalisation of nanomaterials, but it can also assist in identifying the points of interactions and modes of adsorption of nanoparticles [101].

Figure 4.1 shows the FT-IR spectra of the starting material: natural graphite flakes (GF) and the graphene oxide (GO). The GF spectrum shows characteristic peaks at 2082, 2316, and 2622 cm^{-1} respectively. The sharp peak observed at 2082 cm^{-1} is from the unoxidized sp^2 C=C bonds. Upon treatment of the GF with oxidizing agents, the peaks at 2082 and 2316 cm^{-1} shifted to lower absorption bands: 2071 and 2267 cm^{-1} respectively; with reduced intensity in the GO. The emergence of new peaks at absorption bands 1008, 1396, 1556, 1695, 1870 and 3052 cm^{-1} respectively, suggests that modification of the natural graphite was successful. The peaks observed can be attributed to the presence of several functional groups: C-O vibrations (1187 cm^{-1}); the C=O and C=C stretching vibration (1556, 1695, 2071 cm^{-1}), and O-H (3052 cm^{-1}) stretching vibration [102]. When compared to the graphite flakes, it can be seen that GO is heavily oxygenated with the hydroxyl and carbonyl groups from the carboxylic acid. The

presence of these oxygen-bearing groups is indicative of successful oxidation of the natural graphite flakes.

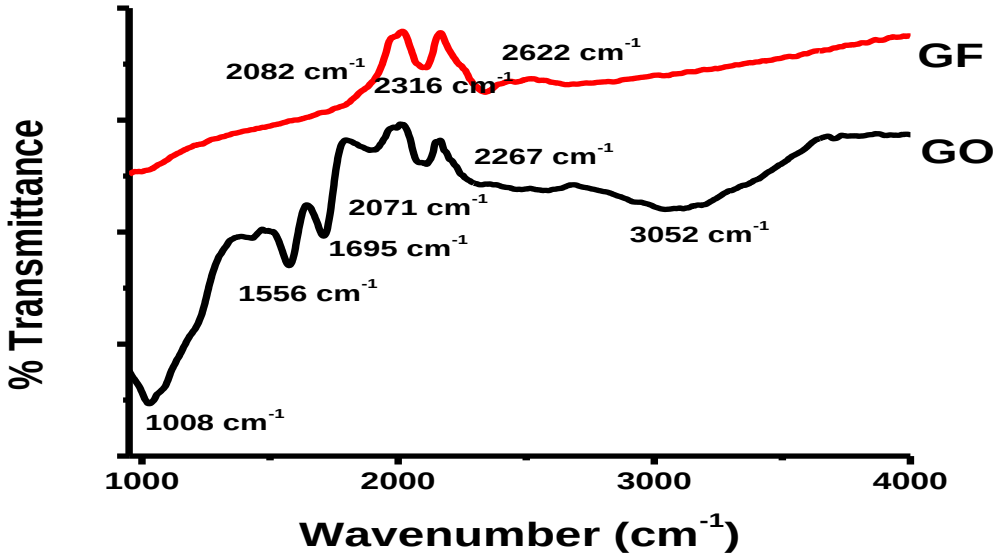

Figure 4.1: FTIR spectra of Graphite flake (GF) and Graphene oxide (GO)

(b) Raman spectroscopy is a light scattering technique in which an excitation laser is focussed on the material of interest. The interaction of the light photons with the material scatters the light at a slightly different frequency. It is this slight shift in frequency, aptly named the Raman shift, which provides the materials' unique fingerprint. Raman spectroscopy has become a powerful and non-destructive technique used for examining the ordered and disordered structures. Thus it can be used to observe the transformation in the structural pattern during chemical synthesis of graphite to graphene oxide and the oxidation of MWCNT. Figure 4.2 shows the Raman spectra of (a) natural graphite, (b) graphene oxide, while figure 4.3 shows that of the pristine and functionalised MWCNT.

The spectrum obtained for the graphite shows Raman bands at 1583, 2334 and 2502 cm^{-1}. The strong G band observed at 1583 cm^{-1} corresponds to the stretching of the C-C bonding. It is a

primary-in plane vibrational mode that is characteristic of natural graphite and has been reported [103] and corresponds to the first order scattering of E_{2g} mode. The bands observed at 2334 and 2502 cm^{-1} are second-order overtones in a different in-plane vibration and have been attributed to overtones of Raman forbidden fundamentals [104].

The Raman spectrum of GO (Figure 4.2 (b)) show the D ~ 1340 cm^{-1} and G ~ 1585 cm^{-1} bands respectively. The D-mode appearing at 140 cm^{-1} is supposedly caused by the disordered structure in sp^2-hybridized carbon materials. The blueshift in the G-mode shows the transformation from graphite to graphene oxide (1583 to 1586 cm^{-1}) and implies the successful formation of GO.

Table 4.1 Comparison of the band positions in the Raman spectra of the pristine and functionalised MWCNTs.

Raman Parameter	Pristine MWCNT	Functionalised MWCNT
D	1346 cm^{-1}	1364 cm^{-1}
G	1587 cm^{-1}	1598 cm^{-1}
D'	1628 cm^{-1}	1631 cm^{-1}
G'	2691 cm^{-1}	2697 cm^{-1}
D+G	2905 cm^{-1}	2922 cm^{-1}

Raman spectroscopy is a very valuable tool for the characterisation of carbon nanomaterials. It can be used as the first step in characterising carbon nanotubes. Raman analysis was performed to reveal the structure before and after the functionalisation of the multi-walled carbon nanotubes (Figure 4.3). Both the pristine and functionalised MWCNT have four major characteristic bands *viz.* D, G, G' and D+G which have been cited in literature [105].

It is these bands that can be used to determine the density of structural defects and thereby, the degree of oxidation of the MWCNT after the harsh acid treatment. As can be seen in Figure

4.3, both pristine and functionalised MWCNT have a strong G-band located at 1587 and 1599 cm^{-1} respectively.

The G-band is caused by in-plane tangential stretching of the ordered C=C bonds and it is attributed to the graphite band common to all sp^2 systems [106]. Another characteristic feature of MWCNTs that appears in the spectra is the D-band at 1346 and 1364 cm^{-1} for pristine and treated MWCNT respectively. It is defect dependent and it is assigned to the defects and disorder in the carbon structure. In order to trace the modification of the MWCNT during acid treatment requires a certain number of defects in the structure. The analysis of the bands is critical because these features are strongly dependent on the oxidation process. Figure 4.3 shows that the line shapes of both the G and D bands are mostly preserved after acid treatment. However, both bands are affected and shift towards higher wavelength with regards to the pristine MWCNT. This observed shift of the Raman response of the treated MWCNT could be caused by doping effects (electron doping) upon acid treatment. The lower upshift for the G-band (11 cm^{-1}) can be attributed to the high degree of crystallinity of the sample, while the greater upshift (18 cm^{-1}) observed for the D-band could be attributed to the fact that the nitric and sulphuric acid used create defective sites in the carbon nanotube wall structure, resulting in the formation of carboxyl and carbonyl groups on the surface of the nanotubes[107] that inherently lead to greater modifications in the defect band [108]. Other features observed in the Rama spectra are the D'-bands (1628 and 1631 cm^{-1}); the G'-bands (2691 and 2697 cm^{-1}) and the D+G (2905 and 2922 cm^{-1}) in the pristine and treated MWCNT respectively. The D'-bands appear as slight shoulders on the G-bands at higher frequencies and are also induced by disorder and defects[95]. The G'-bands originate from a double resonance process or what is called a second-order Raman scattering process. The G'-band shows an upshift, expansion and an increase in intensity after the MWCNTs are treated with acid. The explanation proffered for the evolution of the Raman spectrum is that oxidation of the

MWCNTs with acid stimulates stronger charge transfer which translates into the Fermi level shift.

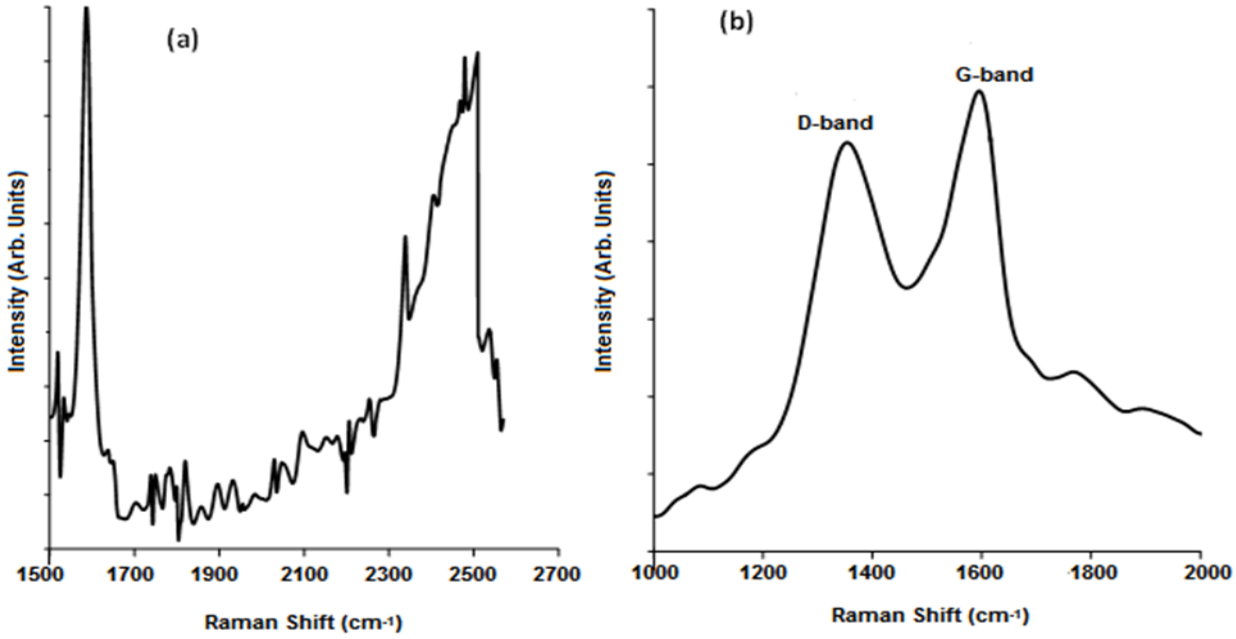

Figure 4.2: Raman spectra of (a) Graphite flake GF (b) Graphene oxide GO.

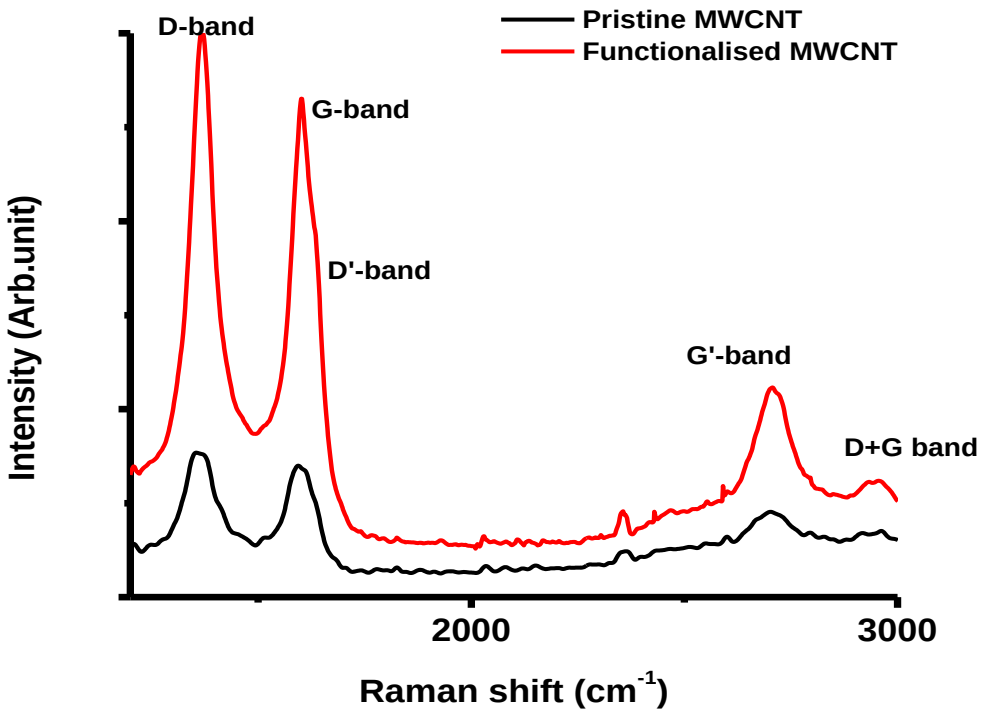

Figure 4.3: Raman spectra of Pristine MWCNT and functionalised MWCNT.

(c) Ultraviolet-Visible (UV-Vis) spectroscopy has been widely used to quantitatively characterize both organic and inorganic nanoscale molecules [109]. Like other forms of spectroscopy it is based on the interaction between electromagnetic radiation and matter. UV-Vis spectroscopy is used to quantify the light absorbed and transmitted by the sample: the electromagnetic waves in the ultraviolet and visible ranges are used to irradiate the sample, and the absorbed light is analysed through the resulting spectrum. The intensity of the incident and transmitted light is measured and these measurements are compared at each wavelength in order to quantify a samples' wavelength dependent extinction spectrum.

UV-Vis spectroscopy is used to identify the components of a substance, determine the functional groups in molecules. Samples absorb the UV-Vis light which serves to energise the electrons and promotes them to higher orbitals [110].

Nanoparticle optical properties are sensitive to size, shape, concentration agglomeration state and refractive index at the particle surface, and as such, UV-Vis spectroscopy is invaluable for identifying and characterizing nanoscale materials [111]

Figure 4.4 shows the UV-Vis spectra of natural graphite and graphene oxide; UV-Vis is used to determine the characteristic features that are used as means of identification and to observe if the modification of graphite to graphene oxide has in fact taken place. Their maximum absorptions occur at 225 and 232 nm for GF and GO respectively. These maxima are attributed to the $\pi \rightarrow \pi^*$ transitions of aromatic C=C bonds. In addition to the absorption maximum at 232 nm for GO, there is a shoulder at ~315 nm (inset) that can be ascribed to $n \rightarrow \pi^*$ transitions of C=O bonds present in carboxylic acid and carbonyl groups present at the edge of the GO. This is a positive indicator that the graphite has been oxidized [112].

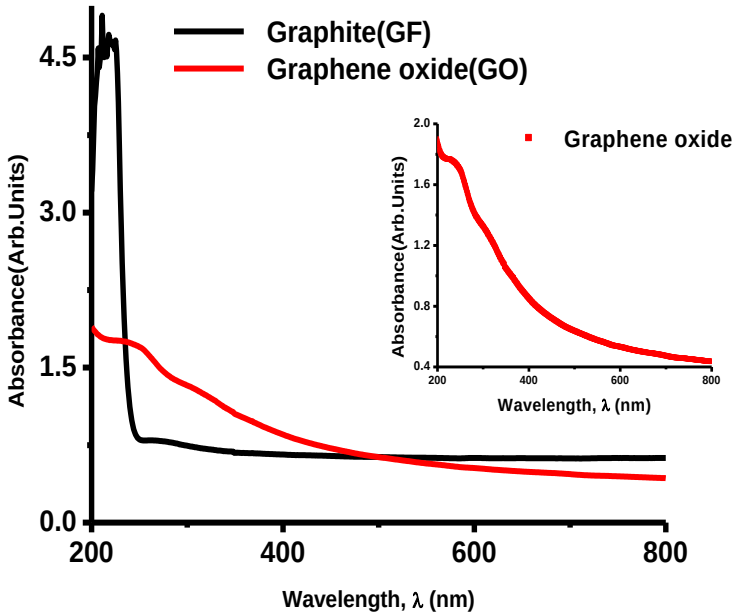

Figure 4.4: UV-Vis spectra of Graphite flake (GF) and Graphene oxide (GO). Inset shows UV-Vis spectrum of GO

The formation of nickel oxide nanoparticles was identified by FTIR spectroscopy. Figure 4.5 presents the FTIR spectra of (a) $Ni(CO_3)_2$ $Ni(OH)_2$ precursor, (b) NiO nanoparticles. The IR spectrum of the precursor is typical of hydrated basic carbonates. The spectrum of the $Ni(CO_3)_2{\cdot}Ni(OH)_2$(s) precursor shows several peaks: 539.98, 588.19, 761.75, 854.32, 1043.32, 1965.14, 2001.78, 2152.20, 2420.27, 2493.54, 2917.82, 3201.31, 3450.08 and 3693.08. The broad high wavenumber absorption bands (3450.08 - 3639.08 cm^{-1}) are attributed to the O-H bond stretching vibrations and other O-H containing compounds, which also imply the presence of water in the structure. The more prominent mid-low wavenumber absorption bands in the 1970-800 cm^{-1} region relate primarily to the internal modes of the carbonate ion. The band occurring at 1043 cm^{-1} may relate to the components of the v_1 symmetric stretch of CO_3^{2-}.The lower wavenumber bands may relate to the v_4 out of plane bend (761.75 cm^{-1}) and the v_2 in-plane bend (854.32 cm^{-1}) of CO_3^{2-} [113]. The broad symmetrical bands appearing at (2152.20-2493.54 cm^{-1}) indicate the existence of CO_2 that is derived from powder samples prepared in

air. The strong absorption band at the lowest wavenumbers (539.98-588.19 cm^{-1}) is assigned to the Ni–O stretching vibrations, indicative of the Ni–O structure presented in the hydrated basic nickel carbonate precursor [114].

The disappearance of the peaks in Figure 4.5 (b) after the precursor was calcined, indicates successful transformation of the $Ni(CO_3)_2{\cdot}Ni(OH)_2$ into NiO. The prominent peak occurring at 539.98 - 580.48 cm^{-1} is assigned to the Ni-O stretching vibrational mode. The band at 539.98 cm^{-1} reveals the presence of NiO. The radical reduction in the intensity of the broad band at 3639.08 - 3450.08 cm^{-1} in the precursor, to 3515.65 cm^{-1} in NiO confirms that most of the hydroxyl groups have been transformed to oxide. The low intensity bands at 1334.52 and 1429.02 cm^{-1} are ascribed to the CO_3^{2-} anion. The minor peaks at 1612.22 and 1965.13 cm^{-1} are as a result of the deformation of the H_2O molecule absorbed from the air during the preparation of the NiO powders [115].

Figure 4.5 (c) shows the UV-Vis absorption spectrum for $NiCO_3{\cdot}Ni(OH)_2$ and NiO nanoparticles. As can be seen, the precursor is characterised by a sharp peak at 269 nm (4.62 eV), while NiO nanoparticles have a strong absorption at 329 nm. The absorptions in the UV-region are ascribed to band gap absorptions in both the basic nickel carbonate and the nickel oxide nanoparticles. The band gap energy (E_g) can be estimated using the optical absorption spectrum and Einstein's energy equation:

$$E_g = h \times {}^{C}/_{\lambda} \qquad 4.1$$

Where h is Planck's constant (6.626 $x10^{-34}$Js), C= speed of a photon (3.00x 10^8m/s) and λ is the wavelength (nm).

The band gap for the NiO nanoparticles is ~ 3.78 eV, which is close to the reported value (3.55 eV) [116]. The band gap of nanoscale NiO shows a slight blueshift compared to that of bulk NiO (~3.65eV) and this is reported to be due to quantum size effects [117]

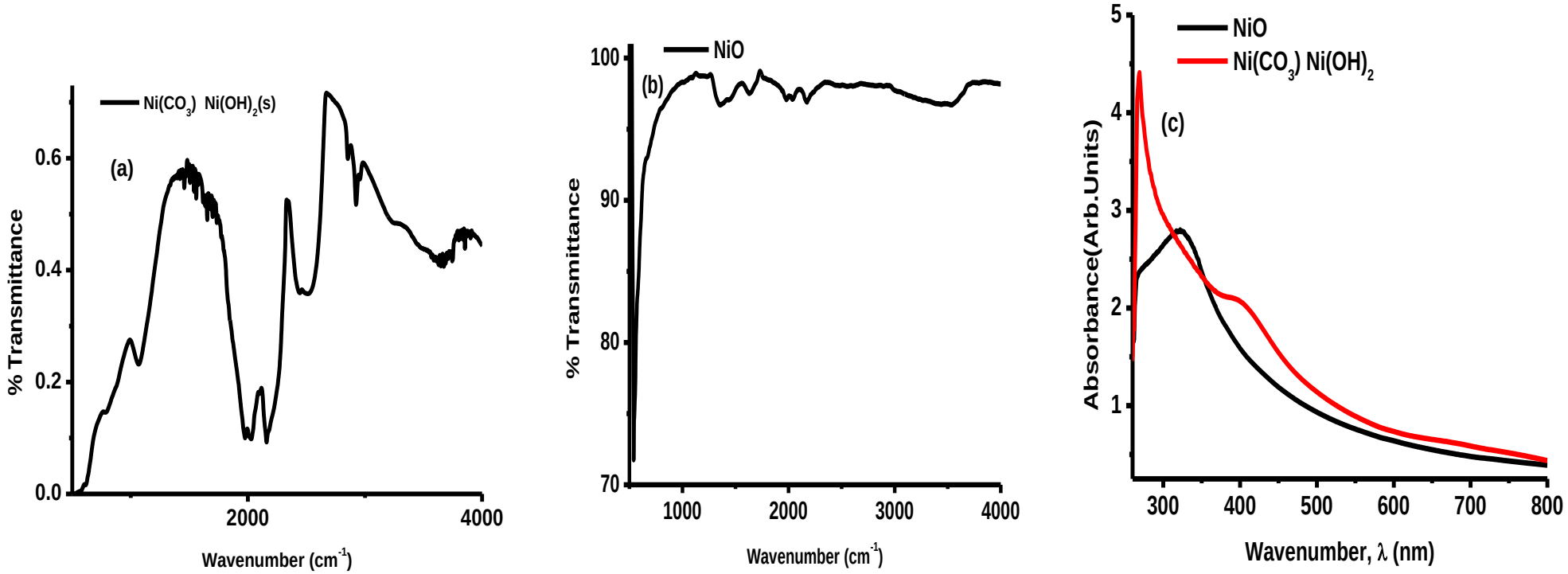

Figure 4.5: FTIR spectra of (a) $Ni(CO_3)_2$ $Ni(OH)_2$(s) precursor and (b) NiO nanoparticles. (c) Comparative UV/vis spectra of $Ni(CO_3)_2$ $Ni(OH)_2$(s) precursor and NiO nanoparticles

The FT-IR spectra of the Cobalt hydroxide ($Co(OH)_2$) precursor and Cobalt oxide (Co_3O_4) are shown in figure 4.6 (a). The spectrum of the $Co(OH)_2$ precursor shows a broad asymmetrical peak at 3205 - 3496 cm^{-1} corresponding to the O-H stretching vibrations of the interlayer water molecules. The peak at 1313 - 1443 cm^{-1} is the characteristic absorption band of intercalated nitrate. The high intensity, low wavenumber peak at 631 cm^{-1} is assigned to the Co-O-H stretching vibrations [118]. After calcination most of the bands associated with the precursor disappear. A stretching frequency at 3367 cm^{-1} and a weak band at 1604 cm^{-1} are evidence of the presence of O-H groups due to the absorption of moisture in the air during powder sample preparation [119]. Two strong absorption bands have appeared at 563 and 665 cm^{-1} and these bands confirm the spinel structure of Co_3O_4. The 665 cm^{-1} (v_1) band is ascribed to the Co-O stretching vibration mode of M-O in a tetrahedrally coordinated site. The band at 563 cm^{-1} (v_2) can be assigned to the octahedrally coordinated M-O, in which M is Co^{3+} [120] . The disappearance of bands associated with the precursor confirms successful transformation of $Co(OH)_2$ to Co_3O_4 after calcination.

Figure 4.6 (b) and (c) show the UV-Vis absorption spectra of the $Co(OH)_2$ precursor and the calcined Co_3O_4. The cobalt hydroxide precursor formed had a blue-green hue typical of the α-phase hydroxide. The $Co(OH)_2$ has a sharp peak at 268 nm, a shoulder appearing at 311 nm and a broad low absorbance peak at ~650 nm. The low wavelength absorption bands are associated with the O^{2-} to Co^{2+} charge transfer process. The broad peak at ~ 650 nm is close to those reported for tetrahedral Co(II) complexes [121], and it is this peak responsible for the blue-green hue of the cobalt hydroxide precursor. The UV-Vis spectrum for the Co_3O_4 exhibits strong absorption bands at 273, 320, 481 and 772 nm, which have been ascribed to ligand-metal charge transfer events. The absorption bands seen at 273 and 320 nm are assigned to the O^{2-} to Co^{2+} charge transfer process, while the bands at 481 and 772 nm are due to the O^{2-} to Co^{3+}

charge transfer process. The Einstein energy equation aforementioned can be used to estimate the band gap. The absorption bands in Figure 4.6 (c) yield two E_g values for Co_3O_4: 3.88 and 2.58 eV. The band gap energy values reported herein are greater than those of bulk Co_3O_4 (E_g= 3.17 and 1.77 eV, respectively) [122] This blueshift can be related to quantum confinement effects and/ or small size effects of the Co_3O_4 nanoparticles [123]

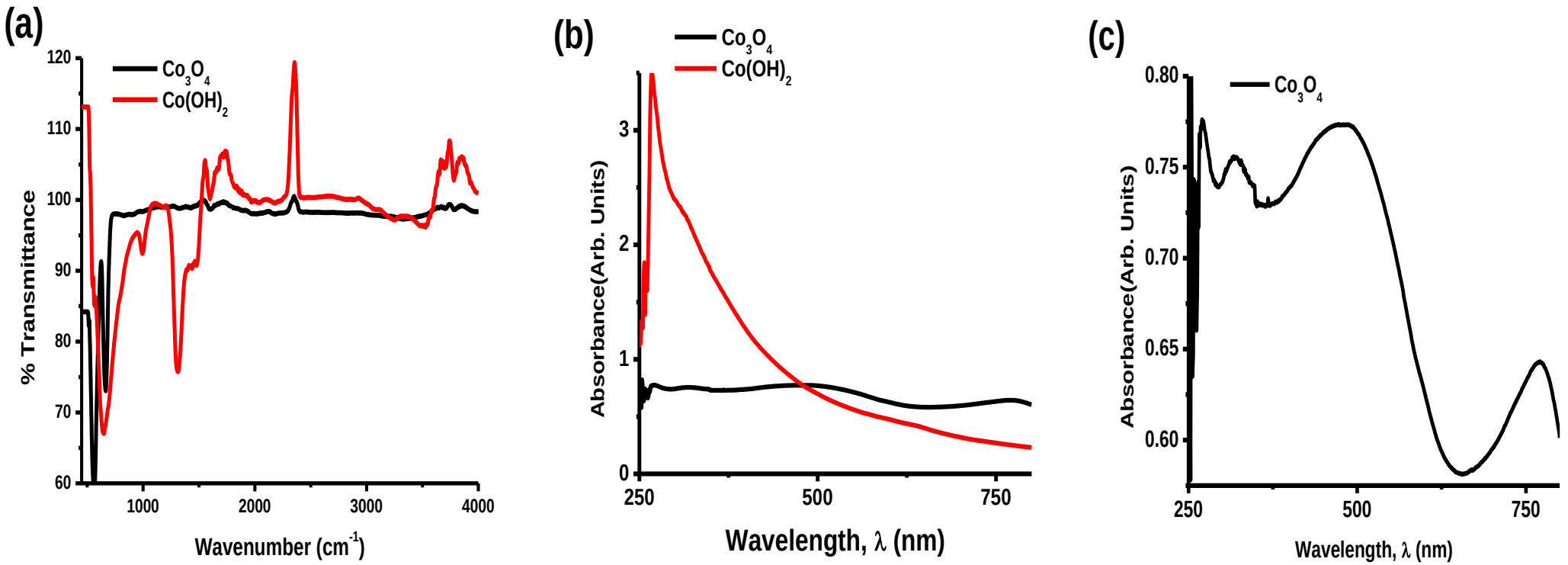

Figure 4.6: FTIR (a) and UV-Vis (b) spectra of $Co(OH)_2$ precursor and Co_3O_4 nanoparticles, and UV-Vis spectrum (c) of the calcined Co_3O_4.

X-ray diffraction is a rapid analytical based on the constructive interference of monochromatic X-rays by a crystalline sample. The interaction of the incident rays with the sample produces constructive interference and a diffracted ray when conditions satisfy Braggs Law, which relates the wavelength of the incident rays to the diffraction angle and lattice spacing in the crystalline sample. When a sample is scanned through a range of 2θ angles, all possible diffraction directions of the lattice can be attained. XRD is used for analysis of nanostructures because the width and shape of the diffracted rays yields information about the substructure of the materials such as crystallite size, microstrain of the lattice, dislocation structures, phase identification of the crystalline materials, unit cell dimensions, etc. [124]. Depending on the information required, there are several approaches used to analyse the X-ray diffraction line profiles. The most widely applied methods are the Scherrer, Williamson-Hall and Warren-Averbach methods. The Scherrer method is simplistic and appropriate in situations where microstrain is deemed negligible, such as when nanoparticles are obtained via chemical methods as opposed to methods that impart intense plastic deformation, such as mechanical milling- wherein the microstrains to the crystalline lattice cannot be ignored and thus the Williamson-hall or Warren-Averbach methods should be used [125].

Because X-ray diffraction line broadening is influenced by the crystallite size and internal strains [126], the Scherrer method was used; where the crystalline size was calculated using the Scherrer formula:

$$D = \frac{K\lambda}{B\ Cos\theta} \qquad 4.2$$

Where *D* is the coherent scattering length (crystalline size); *K* is a constant whose value is approximately 0.9; *B* the width peak B (in rad) was determined as full width at half-maximum (FWHM).

The XRD profiles of natural graphite (GF), graphene oxide (GO), pristine and acid treated MWCNT, NiO and Co_3O_4 are presented below in figure 4.7. The XRD results presented in figure 4.7 (a) and (b) are related to the process of exfoliation and intercalation of oxygen and various molecular species or ions into the graphite to form graphene oxide. The interlayer space (3.38 Å; 002) of the GF (figure 4.7 (a)) exhibits an intense peak at $2\theta = 26.29^{O}$ and a weaker peak at $2\theta = 54.43^{O}$ that are attributed to the reflections of the graphitic layers of carbon atoms tightly packed and held together by van der Waals forces. During oxidation (figure 4.7 (b)), several oxygen containing groups, including C=O, -COOH, OH and C-O-C were introduced at the edges of basal planes of the graphite structure as has previously been shown in the FT-IR spectra. This manifests as an expansion (3.49Å; 002) - a result of the combination of displacement of the carbon atoms, where carbon hydrolyzation occurs and sp^2 bonds change to sp^3 bond. Simultaneously, H_2O, NO_3^- SO_4^{2-} ions insert themselves into the graphene layers and induce the observed increase in interlayer spacing. Furthermore, it was found that after the harsh oxidative treatment, the particles become smaller (GO ~ 46 nm and GF 150 µm). Furthermore, an additional peak appears in the GO profile at $2\theta = 11.47^{O}$, which corresponds to the diffraction of graphene oxide, and the intensity of the (002) diffraction line at $2\theta = 25.53^{O}$ drastically diminished, which is indicative of thorough oxidation of the staring material [127,128].

Figure 4.7(c) shows the XRD patterns of the pristine MWCNT and functionalised MWCNT. The profile for the pMWCNT shows a sharp reflection at $2\theta = 25.75^{O}$ and 25.22^{O} that are characteristic of MWCNT; these can be indexed as the C (002) reflection by the hexagonal graphitic structure. After the acid treatment, the profile remains largely unchanged and this is because generally, well crystallised carbon materials are unaffected by acid treatments. Therefore, the fact that the peak at (2θ) 25.22^{O} remains sharp, indicates that the graphite

structure of the MWCNTs was oxidized without any significant damage since any decrease in the order of crystallinity in MWCNTs will impart broadening and downshift of the peaks [129].

The XRD profiles of the synthesized NiO and Co_3O_4 nanoparticles are shown in figures 4.7 (d) and (e), respectively. The XRD characterization confirms that NiO nanocrystallites of cubic phase have been obtained with high purity and high crystallinity. The reflections can be perfectly indexed to the face-centred cubic (fcc) crystalline structure of NiO, not only in terms of peak position, but their relative intensity of the peaks [130, 131]. There are five characteristic diffractions for NiO at (2θ) 37.24, 43.36, 62.88, 75.43, 79.50^O, each corresponding to the (111), (200), (220), (311) and (222) crystalline planes of NiO [66]. The XRD profile indicates that the synthesized NiO is very pure and occurs in single phase. The average grain size, from the X-ray line broadening, as calculated using the Scherrer integral breadth method, has been estimated as 23.77 nm, with the crystallite sizes ranging from 16.97- 30.58 nm.

The XRD profile for cobalt oxide figure. 4.7 (e) shows broad weak diffraction peaks at (2θ) 19.20, 31.57, 36.99, 45.01, 59.66, 65.47, and 94.42^O. These reflections can be indexed to the crystalline face-centred cubic (fcc) phase Co_3O_4 of Fd-3m (227) space group which are in agreement with the literature [123]. The reflections coincide with the (111), (220), (311), (400), (511), (440) and (533/520). There were no peaks attributable to impurities, indicating that the final product is of high purity. The diffraction peaks are broad, and this can be ascribed to the small size effect characteristic of nanoparticles. The mean grain size was estimated using the Scherrer formula and the X-ray line broadening of the diffraction peaks. The crystallite sizes range from 23.61-61.90 nm, and the mean size of the particles is estimated to be approximately 45.56nm.

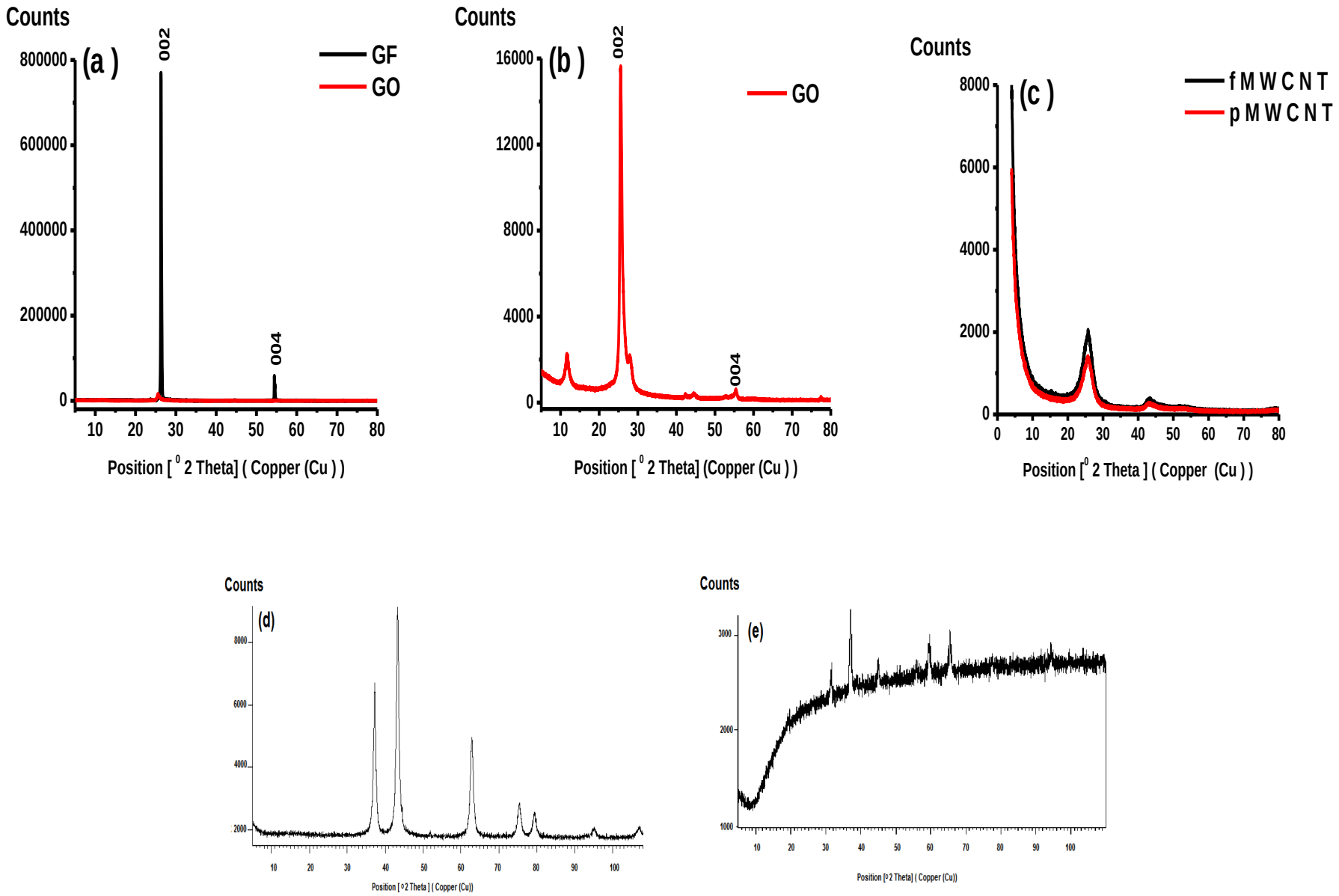

Figure 4.7: XRD spectra of (a) GF and GO, (b) GO, (c) pristine and functionalised MWCNT (d) NiO nanoparticles and (e) Co_3O_4 nanoparticles.

(d) Energy dispersive X-ray (EDX) analysis is a quantitative technique used to analyse surface elements and estimate their relative proportions at different positions on the sample surface, and thus yielding an overall map of the sample. EDX is used for the elemental analysis of sample. It is often use in conjunction with SEM. By virtue of the fact that EDX relies on probing a sample via the interactions between electromagnetic radiation and matter, it is thus considered a type of spectroscopy. The technique uses an electron beam, typically, 10-20 keV, incident on a sample. This in turn causes X-rays to be emitted from the material. The energy of the emitted X-rays is characteristic of a specific atom, thus elemental analysis [132] [110].

Figure 4.8 presents the Energy dispersive X-ray (EDX) spectra of the nanocomposites used as electrode modifier substrates obtained with SEM. The elemental composition of the GO-NiO (A) and GO-Co_3O_4 (B) show the dominant presence of nickel and cobalt respectively. The occurrence of intense oxygen peaks indicates that the metals are in their oxide forms and that the GO has in fact been oxidized and has oxygen containing moieties that were introduced at the edges of the graphite basal planes. The presence of other elements at trace levels are ascribed to the ionic species that have been inserted into the graphene interlayer spaces during oxidation and washing.

Figures 4.8. (C) and (D) are the EDX profiles for the acid treated MWCNT-MO nanocomposites; where figure 4.8 (C) is the fMWCNT-NiO and figure 4.8 (D) is the fMWCNT-Co_3O_4 . The incidence of Ni and Co peaks in (C) and (D), respectively confirms the presence of the respective metal nanoparticles. The oxygen peaks show that the metals exist in their oxide forms. The pronounced S peaks are due to the sulphur from the harsh H_2SO_4 treatment and any remaining SO_4^{2-} ions present after the MWCNT were washed.

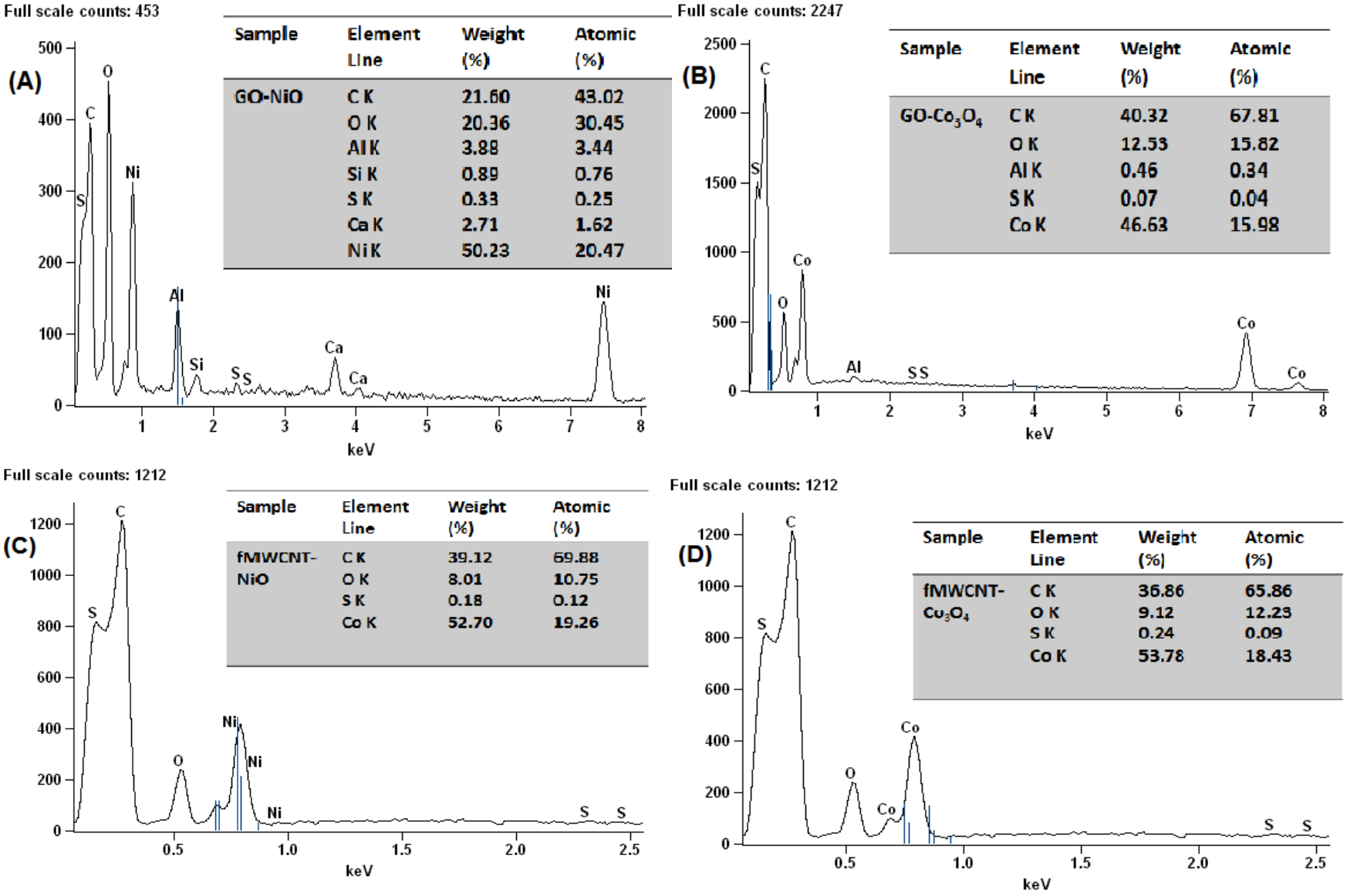

Figure 4.8: EDX spectra of (A) GO-NiO, (B) GO-Co_3O_4 (C) fMWCNT-NiO, (D) fMWCNT-Co_3O_4 nanocomposites. Insets are the tables of quantities.

4.1.2 Microscopic Characterisation

(a) Transmission electron microscopy (TEM) is a vital characterisation tool especially useful for imaging nanoscale materials in order to obtain quantitative measure of the particle size, particle size distribution and morphology.

TEM imaging is a type of electron microscopy. It involves the transmission of a beam of electrons through an ultra-thin sample. These electrons interact with the sample as they pass through. Collection of transmitted electrons forms an image. Because electrons are used as opposed to light to illuminate the sample, TEM yields higher resolution images than light-based imaging techniques. The image formed as a result of the electrons' interaction with the sample is magnified and focussed onto an imaging device, such as a fluorescent screen on a layer of photographic film. Successful imaging depends on the contrast of the sample relative to the background. This is achieved by drying samples on a copper grid that is coated with a thin layer of carbon. This creates a situation in which, materials with electron densities higher than amorphous carbon are easily imaged. TEM is a versatile characterisation method. It has found use in environmental studies, cancer research, virology and materials science [133].

(b) In a similar fashion to TEM, scanning electron microscopy (SEM) uses a high energy electron beam, but the beam is scanned over the sample surface and the back-scattered electrons form the image. SEM provides information about surface morphology. SEM analysis finds application in failure analysis, physical and chemical analysis of surfaces, microstructural analysis and particle analysis [134].

The low magnification SEM micrographs of the starting material, natural graphite flakes and the exfoliated graphene oxide are shown in figure 4.9 (a-d). The graphite flakes are circular flaky platelets (a). The prominent form (crystal face) visible is the basal pinacoid (0002). The corresponding image (c) is the flake edge, showing the compact layers with perfect terraces

[135]. After oxidative treatment, the layers of the flakes wrinkle and the edges separate as can be seen in (b) and (d) respectively.

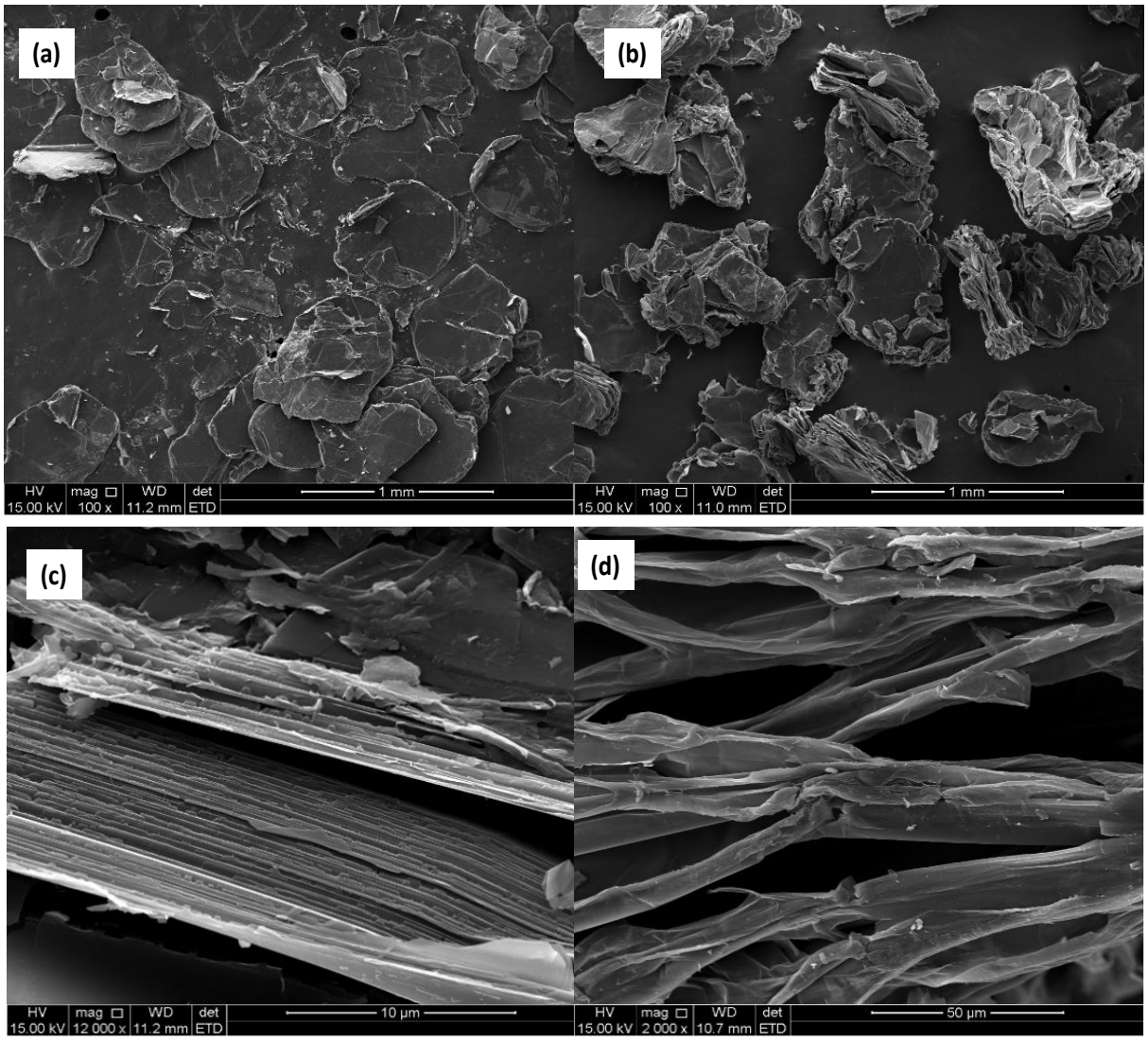

Figure 4.9: SEM image of (a) Graphite flake G (b) Graphene oxide GO (c) Lateral view of GF layers and (d) lateral view of GO.

Transmission electron microscopy (TEM) was used to detect possible morphological changes on the MWCNT after the acid treatment. Figure 4.10.1 shows the TEM images of the pristine (a & c) and oxidized (b & d) MWCNT at low magnification. Figure 4.10.2 (a & b) show high magnification TEM and low magnification SEM (fig 4.10.2 (c & d)) images of pristine (c) and functionalised (d) MWCNT. It is observed that the as-received MWCNTs are surrounded by amorphous carbon on the outer walls. The pMWCNT have thicker walls, they vary in diameter

and show tight kinks. Despite oxidation with strong oxidants such as nitric and sulphuric acid, the MWCNTs remain intact and retain their length, which indicates that the treatment is not destructive, while simultaneously producing a highly purified material as has been shown by other techniques such as Raman spectroscopy. It was observed that the combination of acid treatment and sonic vibration removes impurities such as amorphous carbon and metal catalyst used during the synthesis of pMWCNT. In addition, the fMWCNT are exfoliated, and this is seen as a reduction in diameter, a straightened and relaxed appearance [107, 136].

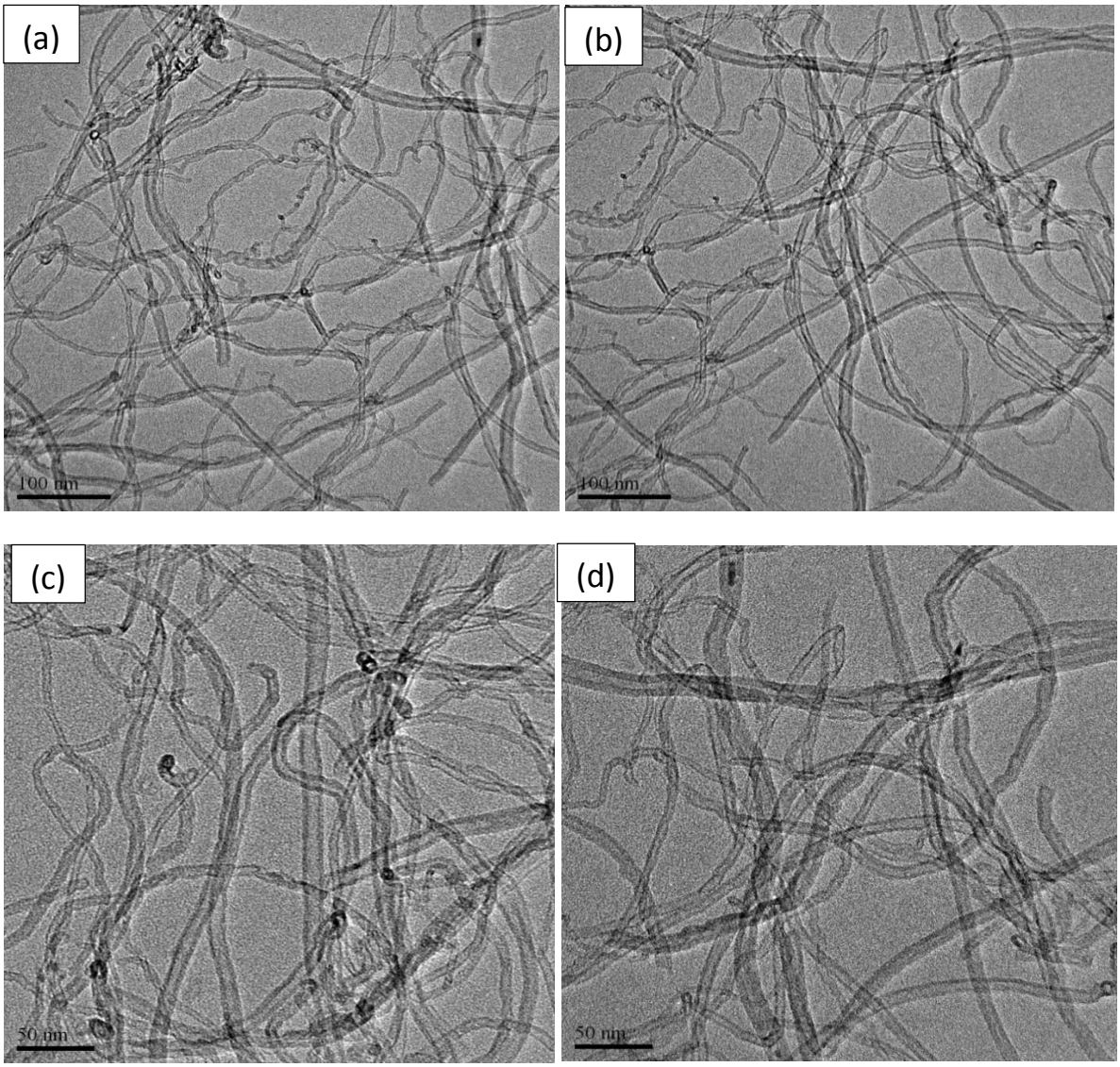

Figure 4.10.1: TEM images of (a & c) pristine and (b & d) functionalised MWCNT from low to high magnification.

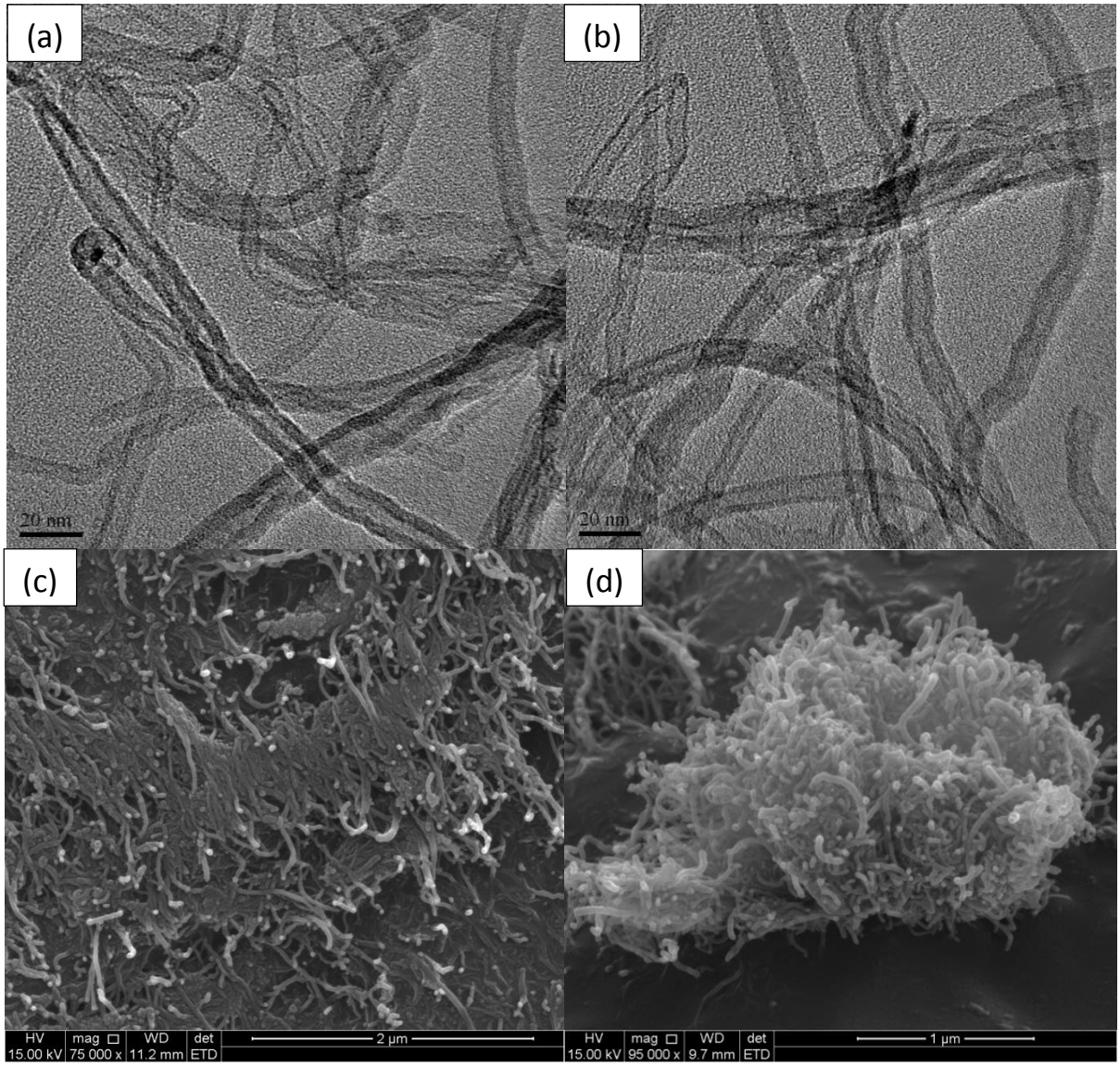

Figure 4.10.2: High magnification TEM images of (a) pristine and (b) functionalised MWCNT. SEM images of (c) pristine and (d) functionalised MWCNT.

Figure 4.11.1 presents the SEM micrographs of (a) $NiCO_3 \cdot Ni(OH)_2$(s) precursor, (b) NiO nanoparticles and figure 4.11.2, the TEM images of NiO at low (a) and high (b) magnification. From the SEM images the surface morphology of the basic nickel carbonate precursor (a) can be seen. The $NiCO_3 \cdot Ni(OH)_2$ generally has spherical aggregated microspheres and these are made up of numerous nanospheres. After calcination, the particles were drastically reduced in size to uniform discrete NiO nanospheres. The TEM images showed that the NiO particles appeared crystalline and evenly distributed. The NiO particles are hexagonal, with the average

particle size for NiO estimated as 26.50 nm. The reported particle sizes were obtained after calibrating the scale of the TEM image using the Image J. Tool for Windows. The particle size 26.50nm for NiO agreed closely with the 23.77 nm estimated using XRD and the 24 nm for NiO nanoparticles [130] made via surfactant assisted synthesis, but larger than the 13 nm reported NiO prepared by calcination of ammonium precipitates [137]. The particle size histogram was determined by counting 107 particles in a randomly selected region on the image. The histogram from the TEM analysis is shown as an inset in Figure 4.11.2 (a). It can be seen that the particles have a uniform spherical morphology and an even size distribution.

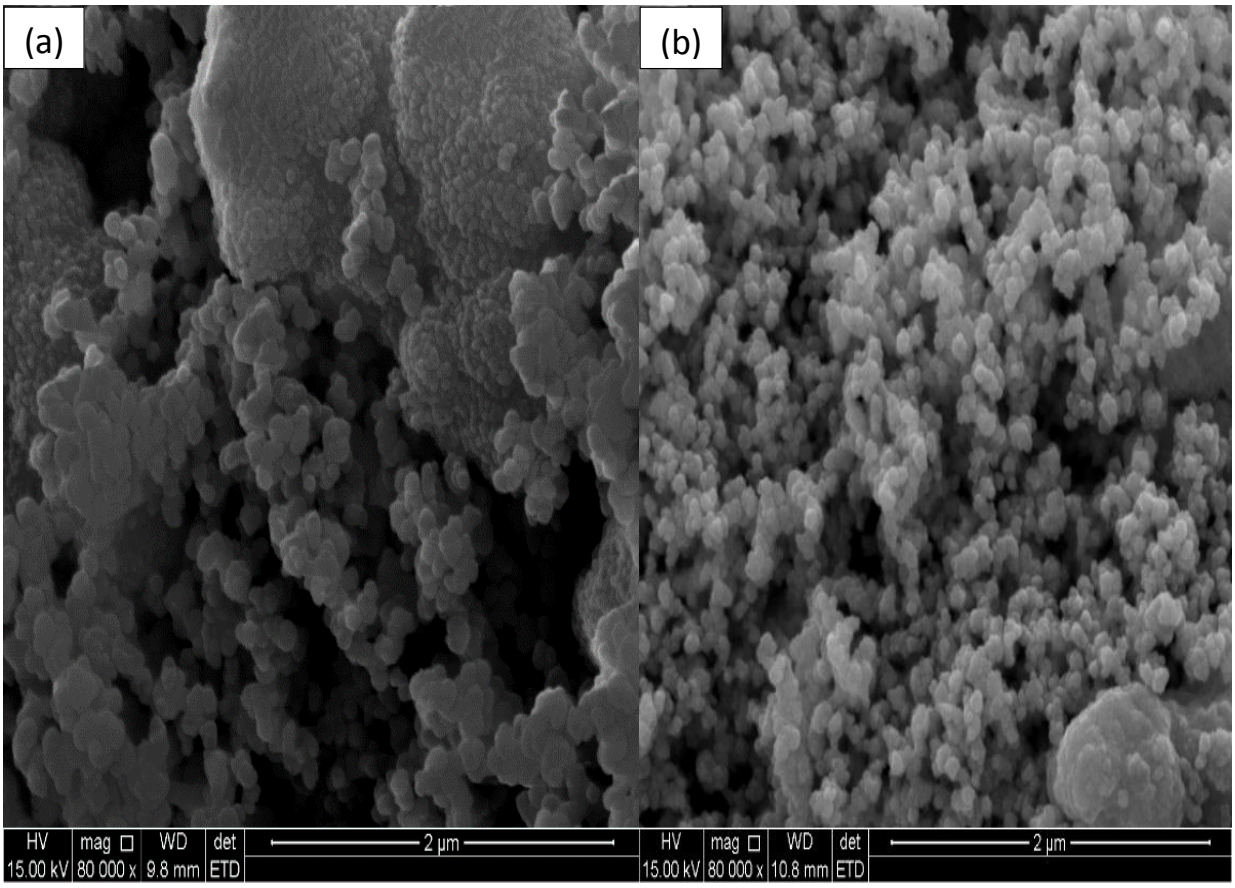

Figure 4.11.1: SEM image of (a) $NiCO_3 \cdot Ni(OH)_2$(s) precursor and (b) NiO nanoparticles.

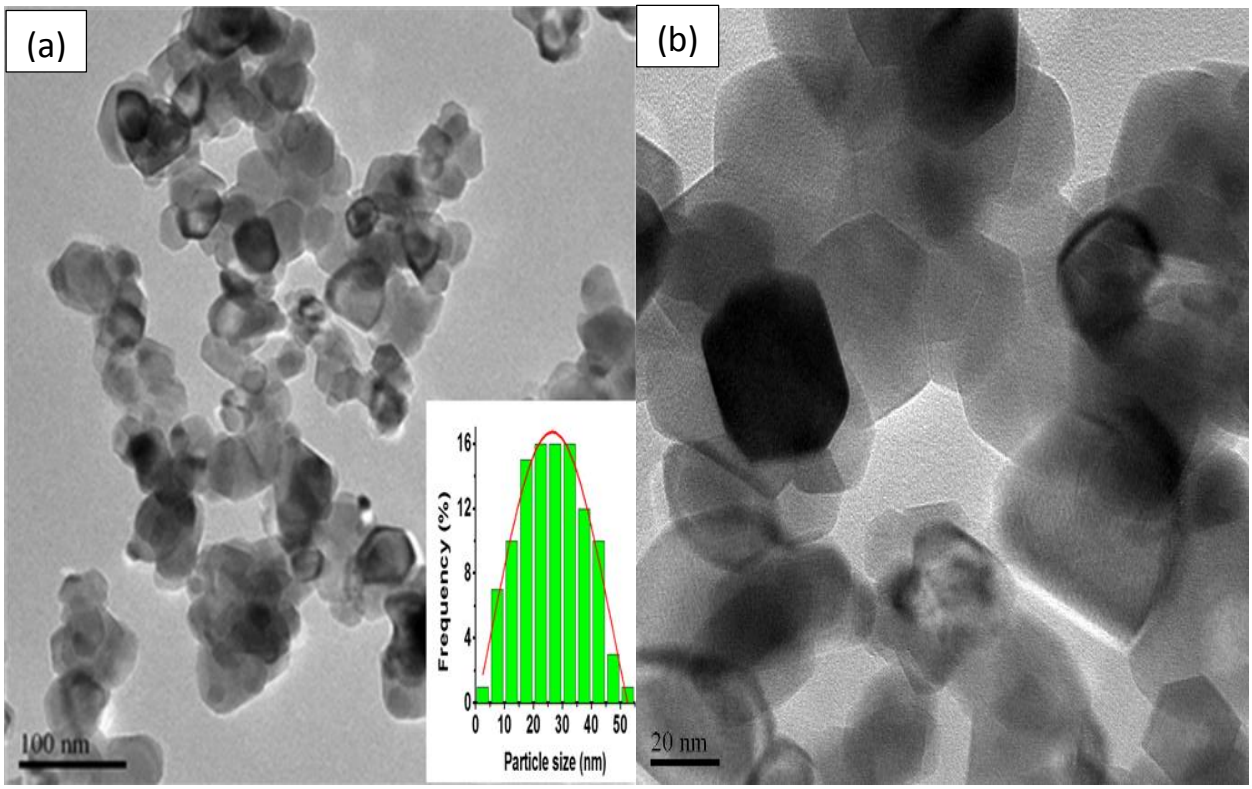

Figure 4.11.2:. TEM images of low (a) and high (b) magnification for NiO nanoparticles. . Inset shows particle size distribution histograms determined from TEM image.

Figure 4.12, shows the SEM images of the cobalt hydroxide precursor (a) and cobalt oxide (b) nanoparticles and TEM images of the low (c) and high (b) magnification cobalt oxide nanoparticles. Figure 4.12 (a) illustrates that the sample contains monodisperse flowerlike microstructures. The spherical microflowers are constructed of uniform hexagonal platelets. After calcination (figure 4.12 (b)), it can be seen that the Co_3O_4 shape changes from the sheet morphology, to clusters of spheres. TEM analysis revealed that the samples consisted of fine porous particles with spherical and irregular shapes with sizes ranging from ~10-70 nm. The size distribution of the Co_3O_4 nanoparticles was investigated from the particles visualised using Image J tool for Windows. The scale of the TEM image was calibrated and the particle size histograms were determined by counting more than 100 particles in a randomly selected region on the image. The histogram from the TEM analysis is shown as an inset in Figure 4.12 (c). It is

evident that the particles have an inhomogeneous morphology and a relatively narrow size distribution.

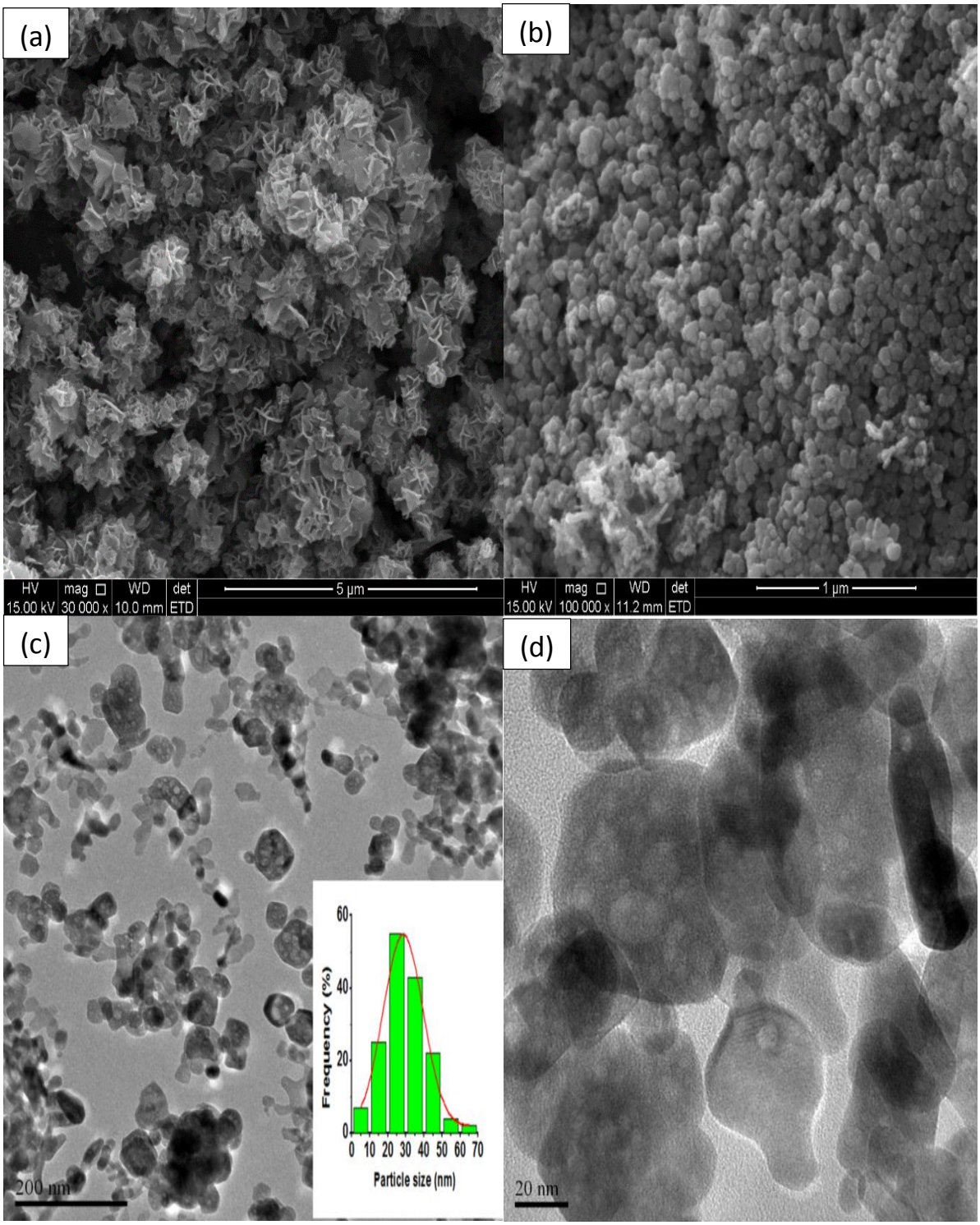

Figure 4.12: SEM image of (a) $Co(OH)_2$ precursor and (b) Co_3O_4 nanoparticles. TEM images of low (c) and high (d) magnification for Co_3O_4 nanoparticles. Inset shows particle size distribution histograms determined from TEM image.

Figure 4.13 (a-d) presents the SEM images of the various nanocomposites and their typical morphologies. Figures 4.13 (a) and (b) show the very well exfoliated and wrinkled graphene oxide sheets, densely decorated with (a) NiO and (b) Co_3O_4 nanospheres. The SEM images of the fMWCNT-MO composites (figure 4.13 (c) NiO and (d) Co_3O_4) show that the composites have been successfully formed, with the metal oxide nanoparticles embedded in the fMWCNT bundles. The modifying substrates composed of the carbon nanotubes and metal oxides appear as rough, porous aggregates with a large surface area. The fMWCNT are entangled and form a closely connected network, which allows the MWCNT to create a relatively dense film on the GCE.

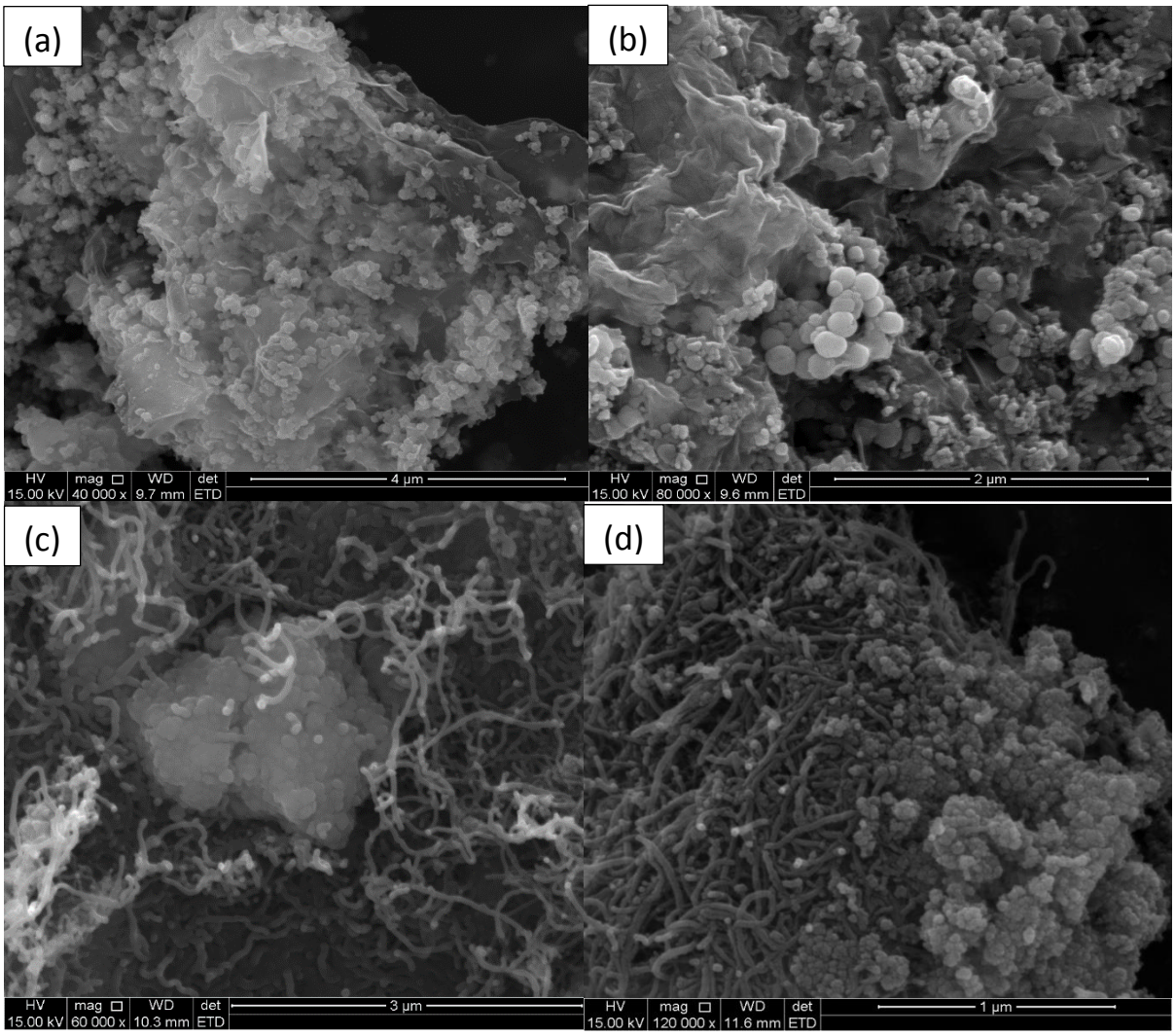

Figure 4.13: SEM image of (a) GO-NiO nanocomposite (b) GO-Co_3O_4 nanocomposite (c) MWCNT-NiO nanocomposite and (d) MWCNT- Co_3O_4 nanocomposite.

4.2 ELECTROCHEMICAL CHARACTERISATION

In order to confirm the modification of the GCE and to determine the electron transport properties of the modifier substrates, cyclic voltammetric and impedimetric studies of the bare and modified GCE were carried out in pH 7.0 0.1 M PBS electrolyte and a solution containing 5 mM $[Fe(CN)_6]^{3-/4-}$ redox probe. Figure 4.14 (a - c) show the results of the studies carried out in the electrolyte. The casting of GO, fMWCNT, Co_3O_4 or NiO enhances the current, relative to the unmodified GCE in the electrolyte. The nickel oxide based electrodes display an improvement in the current response, however, the GCE-fMWCNT-Co_3O_4 is characterised by the largest current response relative to the other electrodes, nearly ten times that of the GCE-GO-Co_3O_4 and all the NiO based electrodes. This indicates that the electrochemical performance is enhanced by the synergy between the fMWCNT and the Co_3O_4 nanoparticles.

Similar electrochemical behaviour is observed in the $[Fe(CN)_6]^{3-/4-}$ solution, where the cyclic voltammetric responses of each electrode show the characteristic one-electron reduction-oxidation couple in the region of 0-0.4 V associated with[$(Fe(CN)_6]^{-3/-4}$. Various electrochemical parameters such as formal potential ($E_{1/2}$/V), peak-to-peak separation potential (ΔEp/ V), the ratio of anodic and cathodic peak current (Ip_a/Ip_c) and surface coverage (Γ/ mol/cm^2) are summarised in Table 4.2 (relevant equations shown in appendix I). The electrodes show Ip_a/Ip_c values that vary near 1 and inspection of the corresponding voltammograms shows voltammetric reversibility. The peak-to-peak separation (ΔE_P) values indicate that electron transport is fastest at the GCE-GO (85 mV/s) and slowest at the GCE-NiO (408 mV/s) electrode. As in the phosphate buffer solution, the GCE-fMWCNT-Co_3O_4 is associated with the largest current response, and in both the electrolyte and $[Fe(CN)_6]^{3-/4-}$ solution, the GCE-NiO has the lowest current response(second to the GCE).

The GCE-fMWCNT-Co_3O_4 and GCE- Co_3O_4 show broad peaks in the 0.9-1 V region. The anodic peaks (~0.97 V) and cathodic peaks (~0.93 V) can be ascribed to the oxidation of Co_3O_4 which results in the formation cobalt oxyhydroxide and the Co_3O_4/Co_2O_3 redox process [74, 138].

$$Co_3O_4 + H_2O + OH^- \Leftrightarrow 3CoOOH + e^-$$

The GCE-fMWCNT-NiO shows a weak anodic peak at 0.62 V and a broad cathodic peak at 0.42 V. These can be attributed to the redox process of the surface confined Ni(II)/Ni(III), where the following reaction takes place at the surface of NiO [139] :

$$NiO + OH^- \Leftrightarrow NiOOH + e^-$$

An interesting and unexpected observation is made; where in an ideal situation one expects the CVs of the model redox couple to exhibit sharp, symmetric anodic and cathodic peaks with a $\Delta E_p \approx 59$ mV for a fast one-electron process, however large peak separations with $\Delta E_p > 59$ mV are observed for all electrodes, suggesting that an intermediate between a reversible and irreversible redox process- a quasi-reversible process has occurred, which is characterised by sluggish electron transfer kinetics. The variance of the ratio of the anodic and cathodic peak currents from unity can be ascribed to chemical reactions that coincide with the redox process especially those of the metal oxide based electrodes. The GCE modified with metal oxide layers showed poor responses: the GCE-NiO electrode shows an irreversible process with marked peak potential separation (the largest $\Delta E_p = 408$ mV) and a pointedly diminished cathodic peak, resulting in the large $Ip_a/Ip_c = 1.21$; and the Co_3O_4 modified GCE displays the second largest $\Delta E_p = 143$ mV and the smallest peak current ratio of 0.56.

Table 4.2 Summary of voltammetric data obtained for the modified electrodes in 5mM $[Fe(CN)_6]^{-3/-4}$ in 0.1 M PBS.

Electrode	$E_{1/2}$ (mV)	ΔE_p (mV)	E_{fwhm} (mV)	I_{pa}/I_{pc}	10^{-9} Γ (mol.cm^{-2})	I_{pa} (µA)	E_{pa} (mV)
GCE	214	225	183	1.06	-	53.3	325
GCE-GO	217	85	208	0.85	51	32.6	257
GCE-fMWCNT	233	123	234	1.02	411	251	298
GCE-Co_3O_4	219	143	212	0.56	58	42.6	290
GCE-NiO	204	408	269	1.21	89	49.1	401
GCE-GO-Co_3O_4	243	100	200	1.03	48	73.6	291
GCE-GO-NiO	261	110	186	0.88	49	95.4	316
GCE-fMWCNT-Co_3O_4	238	112	139	0.96	117	295	294
GCE-fMWCNT-NiO	233	120	193	0.96	260	185	298

The electrode modified with fMWCNT shows a signal nearly eight times greater than those modified with GO (figure. 4.15 (d)). This higher signal enhancement by the MWCNT is due to the differences in the structures of the two carbon nanomaterials. That is to say, the idealized structure of graphene is two-dimensional with sp^2 hybridized carbon atoms joined by covalent bonds to form a flat honeycomb lattice [140]. However in practice, the structure comprises stacks of graphene layers containing different numbers of atomic sheets to yield a three-dimensional structure. Furthermore, the structure is never atomically flat and so the sheets tend to curl and fold and form corrugated sheets. Graphene oxide is heavily oxygenated and

bears various oxygen-containing groups on both the sp^3 hybridized carbons on the basal plane and the carbonyl and carboxyl groups located on the sp^2 hybridized carbons at the sheet edges as shown previously. It is from these peripheral edges that the electron transfer of graphene originates and is dominant as opposed to its side, where the peripheral edges behave electrochemically in the same way as edge-planes of three-dimensional highly-ordered pyrolitic graphite (HOPG) and the "sides" behave like the electrochemically inactive basal planes of HOPG [141].

MWCNT can be described as sheets of graphene rolled into concentric tubes that share a common longitudinal axis. Critical to the electrochemical behaviour of MWCNTs is their anisotropic nature which stems from the fact that the tube walls are different from the ends. The "rolled" graphene sheet means the side walls have a relatively inert layer of sp^2 hybridized carbon atoms akin to the basal planes of HOPG described above, and the tips of the tubes have carbon atoms bonded to oxygen to yield a more reactive species, similar to the edge planes of HOPG.

Critical to electron transfer rates and efficient performance of an electrode is the microstructure of the electrode. That is the orientation, arrangement and level of surface coverage by the substrate. The small ΔE_p exhibited by GO relative to fMWCNT can be explained in terms of coverage: multilayer graphene oxides, unlike single layer GO have a large proportion of edge-plane sites (e^- transfer sites), and thus the enhanced voltammetric response with increased reaction kinetics and reversibility. However, the decreased current response (in relation to fMWCNT) is due to the relatively inert basal planes occupying a greater surface area on the electrode surface than the edge-planes and thus effectively blocking electron transfer at the underlying GCE surface [142].

The greatly enhanced electrochemical response observed for the acid-treated MWCNT can also be explained in terms of the edge-plane density effect similar to that of the multi-layer graphene-oxide; where, as shown in the SEM images (figure. 4.10.2 (b) and (d)) the bundles of acid treated MWCNT are exfoliated, and this is seen as a reduction in diameter, a straightened and relaxed appearance which exposes a greater proportion of the reactive “tube ends”. A theoretical study conducted found that for CNT cylinders with a radius less than 20 nm, there is an increase in the double layer capacitance; it is the exfoliation by acid treatment that decreases the cylinder diameter and thus enhances the electrochemical driving force for electron transfer [143] . In addition to this, MWCNT have the added property of high effective surface area on a nanometre sized particle which allows the diffusion of the electroactive species to the underlying GCE, thus increasing the current response [144]. The difference in the electrochemical properties GO and fMWCNT translate to the corresponding composites with the metal oxides as shown in figure 4.15(e).

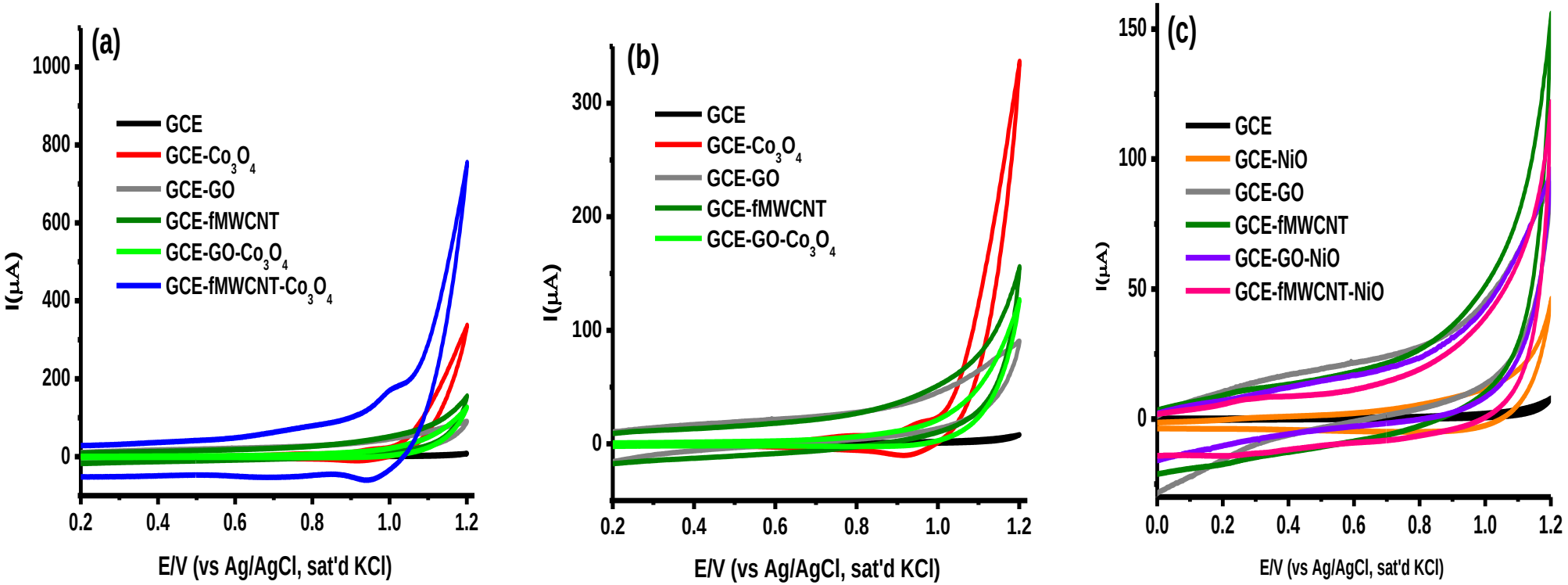

Figure 4.14: Cyclic voltammetric evolutions of GO and fMWCNT with (a) and (b) Co_3O_4 and (c) NiO-based modified electrodes and their respective nanocomposites in pH 7.0 PBS (scan rate = 25 mVs^{-1}).

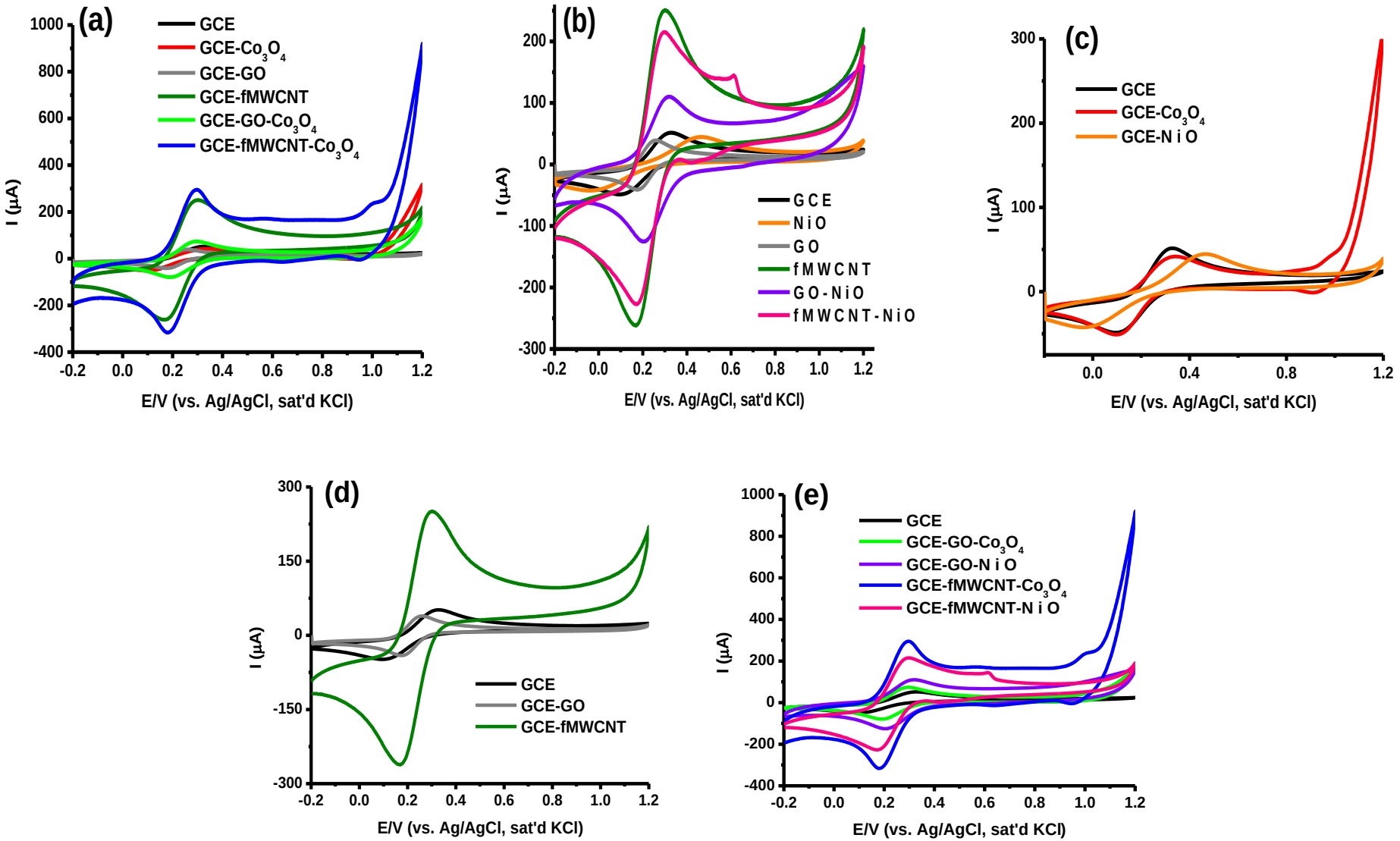

Figure 4.15: Comparative cyclic voltammetric evolutions (a) GO/fMWCNT/Co_3O_4 , (b) GO/fMWCNT/NiO based, (c) Metal oxide nanoparticles, (d) Carbon nanomaterial and (e) nanocomposite modified electrodes in 5 mM $[Fe(CN)_6]^{4-}/[Fe(CN)_6]^{3-}$ (scan rate = 25 mVs^{-1}).

The fact that the $[Fe(CN)_6]^{3-}$ / $[Fe(CN)_6]^{4-}$ redox process occurs at nearly the same formal potential ($E_{1/2}$ ≈0.2 V) for the electrodes creates a challenge in as far as unequivocally establishing the electron transfer rate for any of the electrodes. This necessitates the use of electrochemical impedance spectroscopy (EIS), performed at a fixed potential (0.2 V vs Ag|AgCl, sat'd KCl) and frequencies between 100kHz-0.1 Hz), in order to evaluate the extent to which each electrode modifying substrate allows electron transport between the redox probe and the underlying glassy carbon electrode. Figures 4.16-4.18 show typical Nyquist plots of all the electrodes. The experimental data was fitted satisfactorily using the Randles equivalent circuit. The adequacy of the fit was judged based on the Chi squared (χ^2) function and the relative percentage errors. To better understand the processes taking place on the electrode surface, the interpretation of the data is broadly divided into two regions: the high and low frequency regions. The y-axis represents the negative number of the imaginary part of the measured impedance (- Z" (Ω)) and the x-axis represents the real part of the measured impedance (Z' (Ω)). The Nyquist plot illustrates the charge transfer dynamics of the modified electrode. For reversible electrochemical reactions, the Nyquist plot has two regions: (i) the semicircle at high frequency regions, whose diameter corresponds to the electron-charge transfer process and (ii) a straight line segment at the low frequency region of the plot, which corresponds to the diffusion-limited transport of the redox species at the electrode/electrolyte interface.

The results obtained for the modified electrodes are presented in Table 4.2. The bare glassy carbon electrode had a large semicircle in the high frequency region and gave an R_{ct} value of 2.82 kΩ, exhibiting a short line in the low frequency region, hinting at a diffusive process. . After modification with the various substrates, the R_{ct} values decrease, indicating that the electrode was modified and that the substrates have a higher conductivity and are more facile to charge transfer. Figure 4.16.1 (a) compares the GO and fMWCNT; visual inspection of the

plots of the carbon nanomaterials shows that both GO and fMWCNT have semicircles in the high frequency indicating modification and a drastic decrease in charge transfer resistance (compared to GCE), but GO has a larger semicircle diameter and straight line in the high frequency region indicative of a larger resistance to charge transfer than fMWCNT and a high diffusion system, respectively. The lower charge transfer resistance displayed by the fMWCNT than GO leads to an improvement in the electrocatalytic activity and this is attributed to the fMWCNT providing a larger surface area, whereas the GO tends to block the charge transfer process This result is consistent with the CV results previously obtained, and are validated by the electron transfer rate constants (k_s) obtained for the carbon nanomaterials, where the k_s value for fMWCNT is nearly four times greater than that of GO.

Table 4.3 Impedance data obtained for the modified electrodes in 5mM $[Fe(CN)_6]^{-3/-4}$ in 0.1 M PBS (pH 7) solution at a fixed potential of 0.2 V (vs Ag|AgCl, sat'd KCl).

Electrodes	R_S (Ω cm^2)	C_{dl} (μF)	R_{ct} (Ω cm^2)	Z_W (Ω cm^2)	k_s (cm.s^{-1})
GCE	135	7.25	2.82×10^3	7.85×10^{-4}	2.672×10^{-10}
GO	124	5.71	260	8.94×10^{-4}	2.898×10^{-9}
fMWCNT	127		71	9.33×10^{-5}	1.063×10^{-8}
Co_3O_4	83	6.21×10^{-1}	1.01×10^3	4.23×10^{-4}	7.461×10^{-10}
NiO	85	5.43×10^{-1}	2.02×10^3	1.75×10^{-4}	3.731×10^{-10}
GCE-GO-Co_3O_4	80.9	2.06	183	7.03×10^{-4}	4.118×10^{-9}
GCE-GO-NiO	13.44	36.7×10^{-3}	116	5.37×10^{-4}	6.496×10^{-9}
GCE-fMWCNT-Co_3O_4	34.1	20.2×10^{-3}	70.8	5.26×10^{-3}	2.229×10^{-8}
GCE-fMWCNT-NiO	33.8	115×10^{-3}	66	3.50×10^{-3}	1.142×10^{-8}

Figure 4.16.1 (b) shows the impedance spectra for the two metal oxides. Co_3O_4 and NiO have nearly the same high frequency intercepts , indicating that Co_3O_4 and NiO had the same overall ohmic resistance (the combination of the ionic resistance of the electrolyte(R_s), the intrinsic resistance of the active materials and the contact resistance between the active materials and the current collector). The overlapping depressed semicircles (inset) at high-to-medium frequencies are representative of a parallel combination of the charge transfer resistance (R_{ct}) and double layer capacitance (C_{dl}). The observed overlaps of the metal oxide nanoparticles in the high frequency region are displayed in Table 4.2, where the solution resistance values (R_s) of Co_3O_4 and NiO are 83 and 85 $\Omega.cm^2$; the R_{ct} values: 1.01 and 2.02 kΩ and ; C_{dl} values: 0.621 and 0.543 µF, respectively [145] . In the low frequency region, semicircles of different diameters are observed for the metal oxides. These semicircles at low frequency are said to be frequency dependent and can be ascribed to an oxygen evolution reaction [146] or the adsorption of reaction intermediates on the electrode surface [147]. For impedance measurements run at 0.9 V and 0.8 V for Co_3O_4 and NiO, respectively (not shown), it was found that in the low frequency regions, the impedance spectra showed lines inclined at a constant angle to the real axis that can be attributed to Warburg impedance (Z_w) associated with the $[Fe(CN)_6]^{3-/4-}$ ion diffusion through the metal oxide to the glassy carbon electrode surface [72].

The impedance measurements obtained only serve to qualify the observations made using CV: where fMWCNT and Co_3O_4 show enhanced electrochemical and voltammetric performance relative to GO and NiO, respectively. These qualities translate to the nanocomposites, especially for the fMWCNT-MO composites. The GO-MO composites (figure. 4.16.2 (a)) display unexpected behaviour, in that GO-NiO has a larger current response and a smaller R_{ct} value than GO-Co_3O_4 despite the CV parameters such as peak-to-peak potential seperation (ΔE_p) and peak potential indicating that the GO-NiO modified electrode had sluggish electron transfer abilities than the GO-Co_3O_4 modified electrode; infact, the k_s value for GO-NiO exceeds that

calculated for GO-Co_3O_4. This is seen in the comparative Nyquist plots for the two composites, where GO-NiO has a smaller semicircle diameter than GO-Co_3O_4 in the high frequency region. The differences in the medium-to-low frequency region warrant thought. GO-Co_3O_4 has a higher Warburg impedance (7.03 x 10^{-4} Ω cm^2) fitting than GO-NiO (5.37 x 10^{-4} Ω cm^2), and the line inclined at an angle to the real axis for GO-NiO is steep and indicative of a higher solution diffusion rate [69]. A low resistance and high diffusion rate imply a faster charge transfer process and better accessibility for the $[Fe(CN)_6]^{3-/4-}$. NiO and GO exhibit a positive synergism that can only be speculated upon, as there are several plausible explanations. Tentatively, we offer (based on structural and morphological results obtained previously) that GO-NiO perform better than GO-Co_3O_4 because NiO particles were shown, using XRD and TEM, to be much smaller than the Co_3O_4. The small size of the NiO effectively shortens the electron path-length. The NiO nanoparticles appear to evenly decorate the GO sheets as seen in the SEM images above (figures 4.13 (a)), whereas Co_3O_4 has densely decorate the GO sheets, but it has large agglomerates. The smaller well dispersed NiO nanoparticles are in intimate contact with the conductive GO sheets and thus minimize the impedance for the charge transfer process the electrode/ solution interface [148].

The impedance spectra of fMWCNT-Co_3O_4 and fMWCNT-NiO were compared (figure 4.16.2 (b)), and the results validate the CV findings. At high frequencies, both electrodes exhibit equal high frequency intercepts in the real Z' axis and small overlapping semicircles, and this is seen with their *ca.* close R_s and R_{ct} values, respectively. In the intermediate-to-high frequencies, both electrodes have nearly vertical lines. The straight lines are attributed to the slower mass transport process of diffusion, and as such they are observed in the lower frequency region of the spectra. However, notable is that these lines are not at a 45^o angle typical of an infinite diffusion process, instead, they are nearly perpendicular to the real Z' axis. This indicates a pseudo capacitive behaviour and lower diffusion resistance to the ions as a result of the

mesoporous structures of the metal oxides and this allows for efficient access of the ions to the GCE surface [149] . The deviation of the low frequency line from the imaginary – Z" axis is also attributable to pseudo capacitance effects of the oxygen containing moieties attached to the MWCNT via the acid treatment [150] . This deviation implies that the capacitance, is not purely capacitive as shown by the Randle equivalent circuit, showing C_{dl} , but possibly a constant phase element (CPE) thus taking into account the porosity of the fMWCNT-MO substrate and creating a "real" application situation [151, 152].

Figures 4.17 and 4.18 show different comparative configurations of the Co_3O_4 based (figure 4.17) and NiO (figure 4.18) based electrodes.

Based on the preliminary CV and EIS study conducted to determine the electrochemical properties of the redox active nanomaterials using the $[Fe(CN)_6]^{3-}/[Fe(CN)_6]^{4-}$ redox probe, one might venture that the combination of the ΔE_P , I_p and k_s results indicate that the fMWCNT-Co_3O_4 modified GCE is a superior electrode.

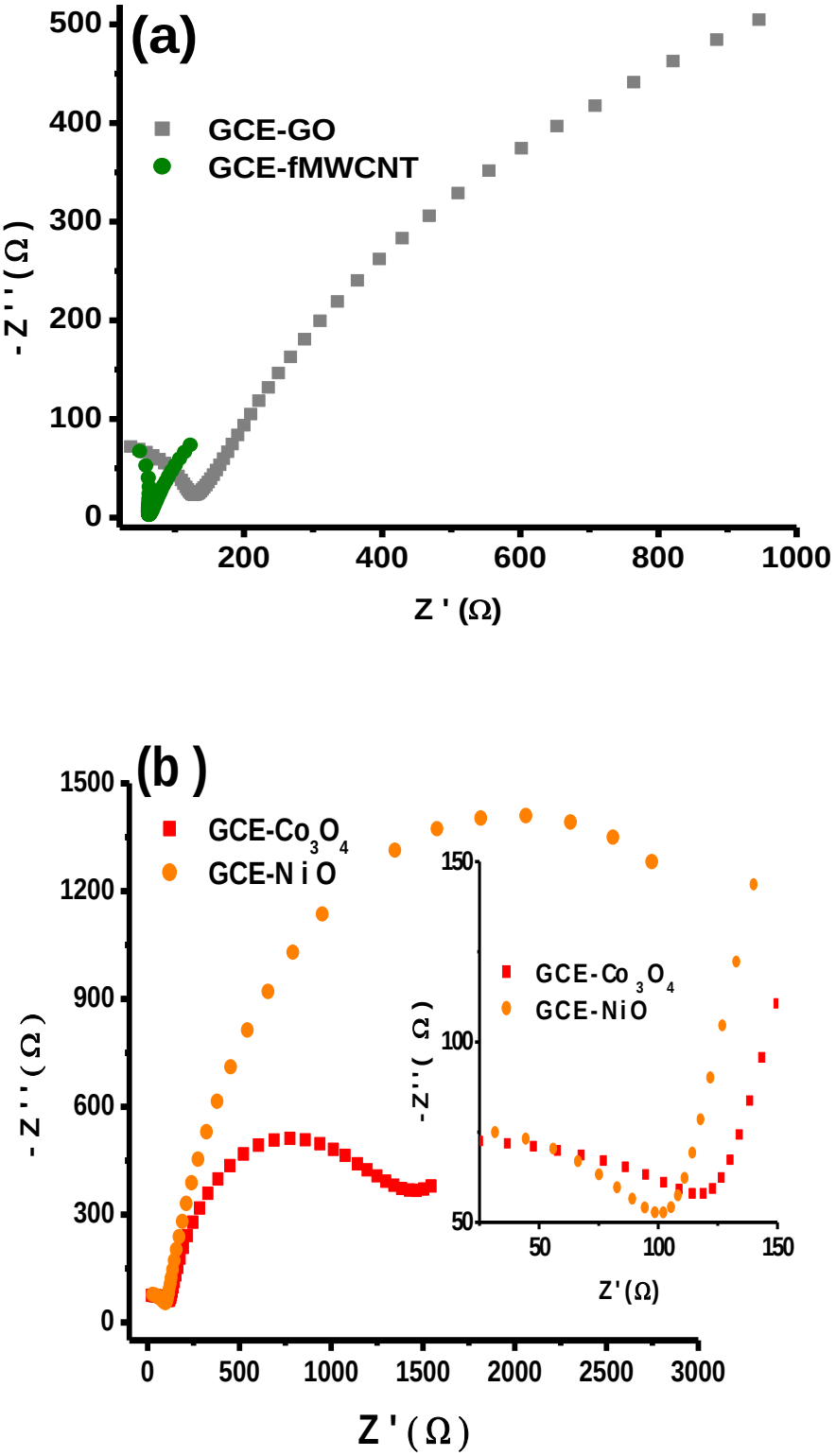

Figure 4.16.1: Nyquist plots obtained for the (a) carbon nanomaterial (b) metal in 5 mM $[Fe(CN)_6]^{4-}$ / $[Fe(CN)_6]^{3-}$ solution (PBS pH 7.0) at a fixed potential of 0.2 V (vs Ag|AgCl, sat'd KCl).

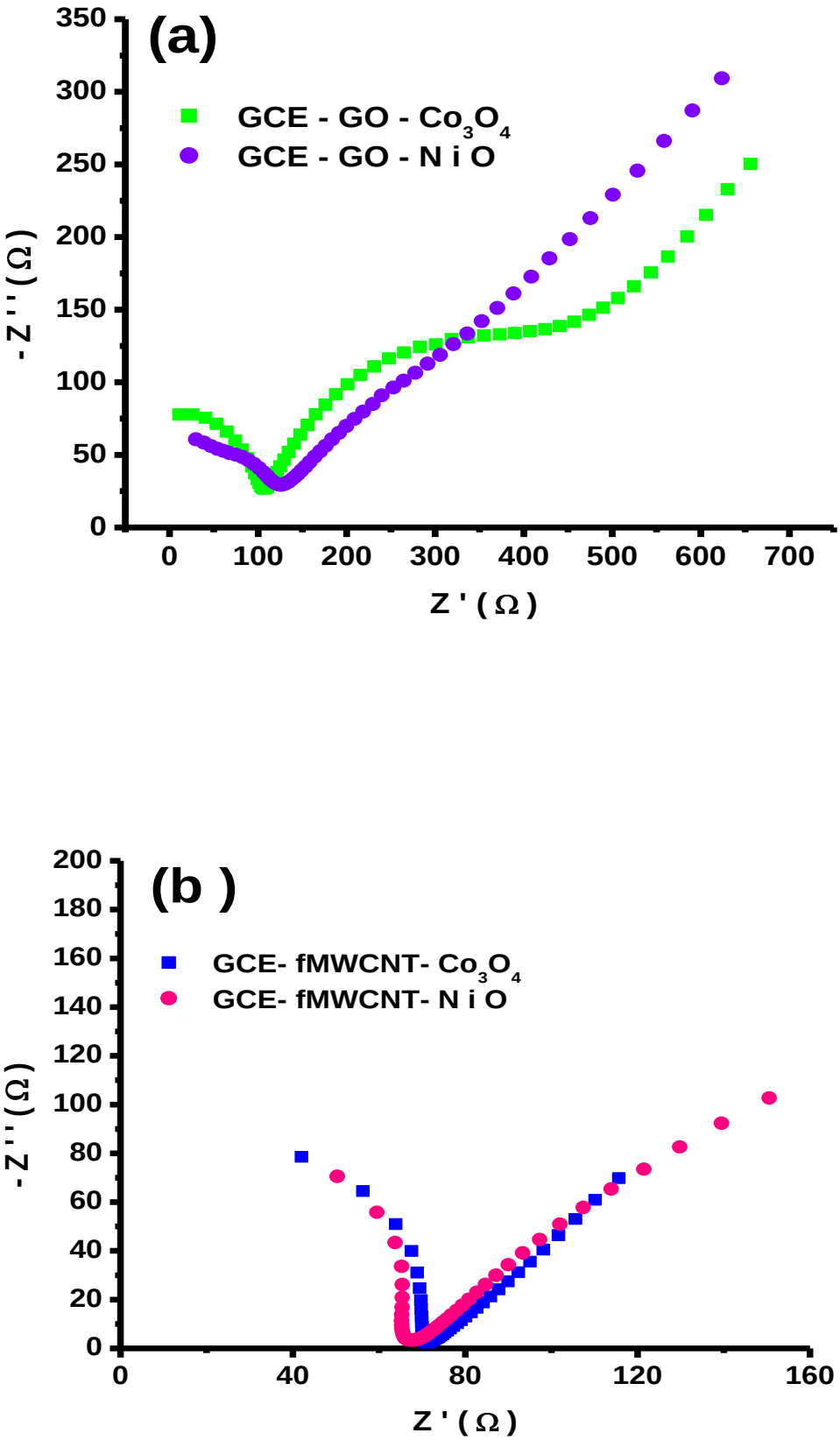

Figure 4.16.2: Nyquist plots obtained for the (a) GO-based composite and (b) fMWCNT-based composite electrodes in 5 mM $[Fe(CN)\ 6]^{4-}$ / $[Fe(CN)\ 6]^{3-}$ solution (PBS pH 7.0) at a fixed potential of 0.2 V (vs Ag|AgCl, sat'd KCl).

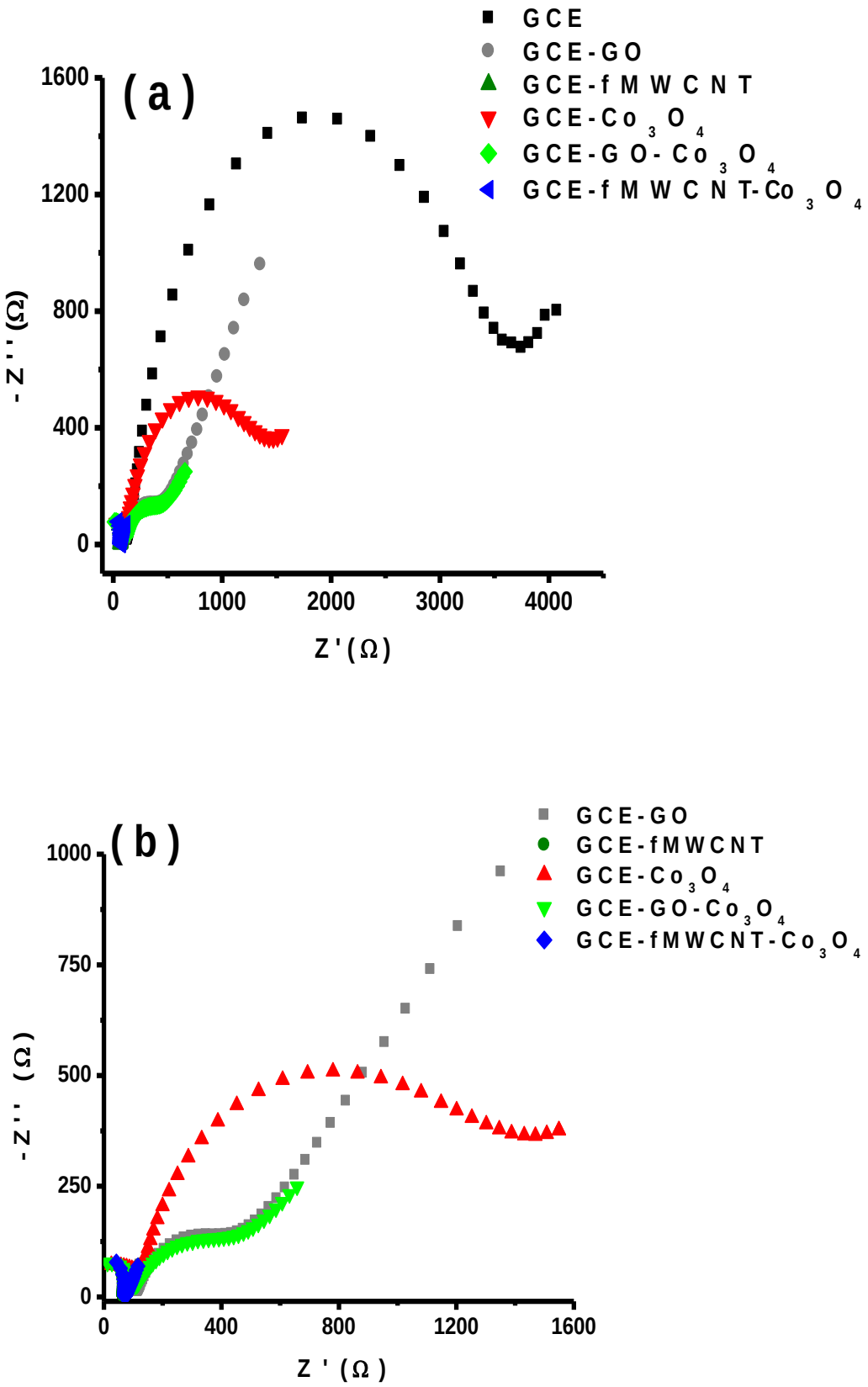

Figure 4.17.1: Nyquist plots obtained for the Co_3O_4 based electrodes in 5 mM $[Fe(CN)\ 6]^{4-}$ / $[Fe(CN)\ 6]^{3-}$ solution (PBS pH 7.0) at a fixed potential of 0.2 V (vs Ag|AgCl, sat'd KCl). (a) with GCE and (b) without GCE for clarity.

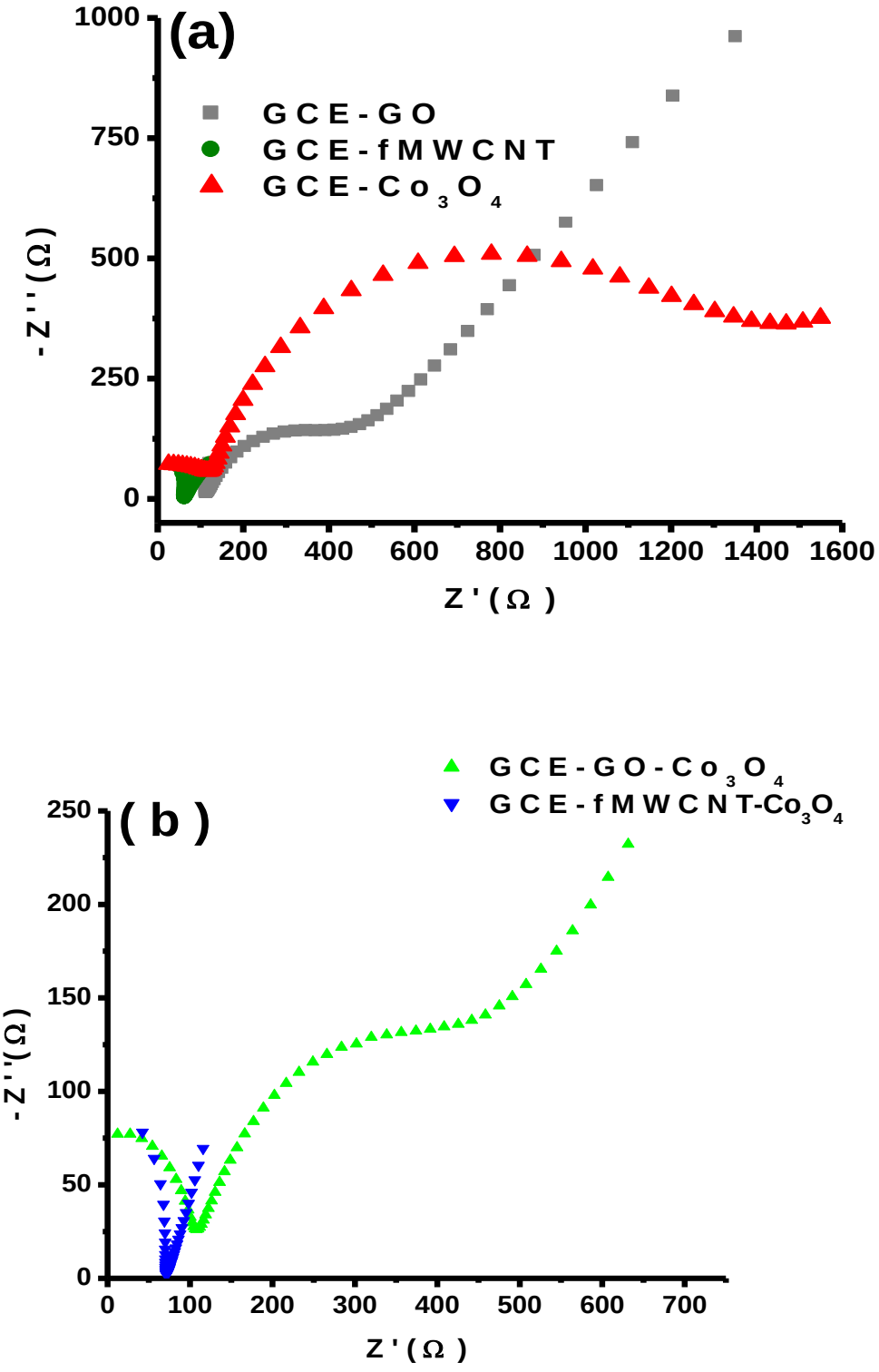

Figure 4.17.2: Nyquist plots obtained for the Co_3O_4 based electrodes in 5 mM $[Fe(CN)\ 6]^{4-}$ / $[Fe(CN)\ 6]^{3-}$ solution (PBS pH 7.0) at a fixed potential of 0.2 V (vs Ag|AgCl, sat'd KCl). (a) compares the metal oxide and the carbon nanomaterials.

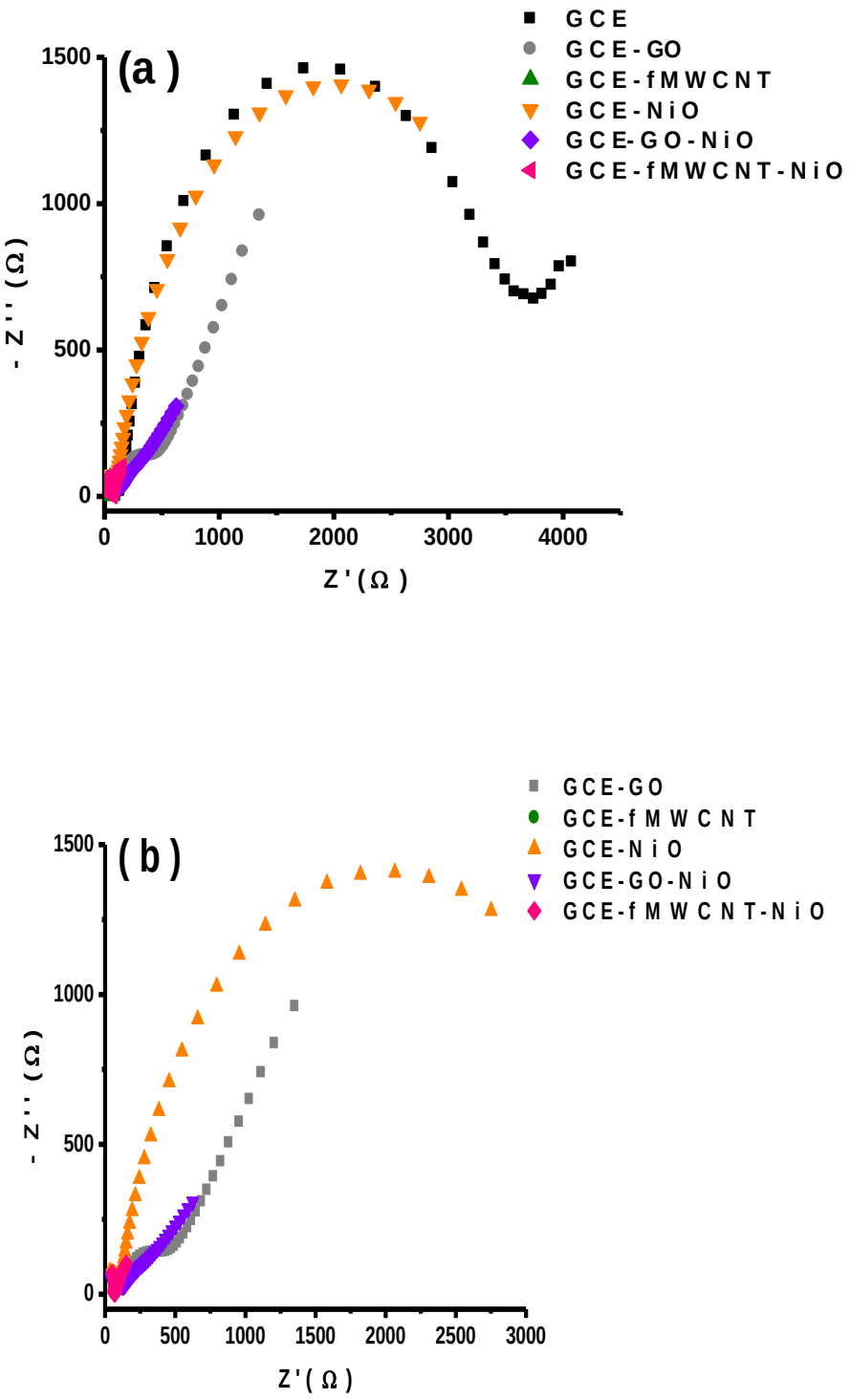

Figure 4.18.1: Comparative Nyquist plots obtained for the NiO based electrodes in 5 mM $[Fe(CN)\ 6]^{4-}$ / $[Fe(CN)\ 6]^{3-}$ solution (PBS pH 7.0) at a fixed potential of 0.2 V (vs Ag|AgCl, sat'd KCl) (a) with GCE and (b) without GCE for clarity.

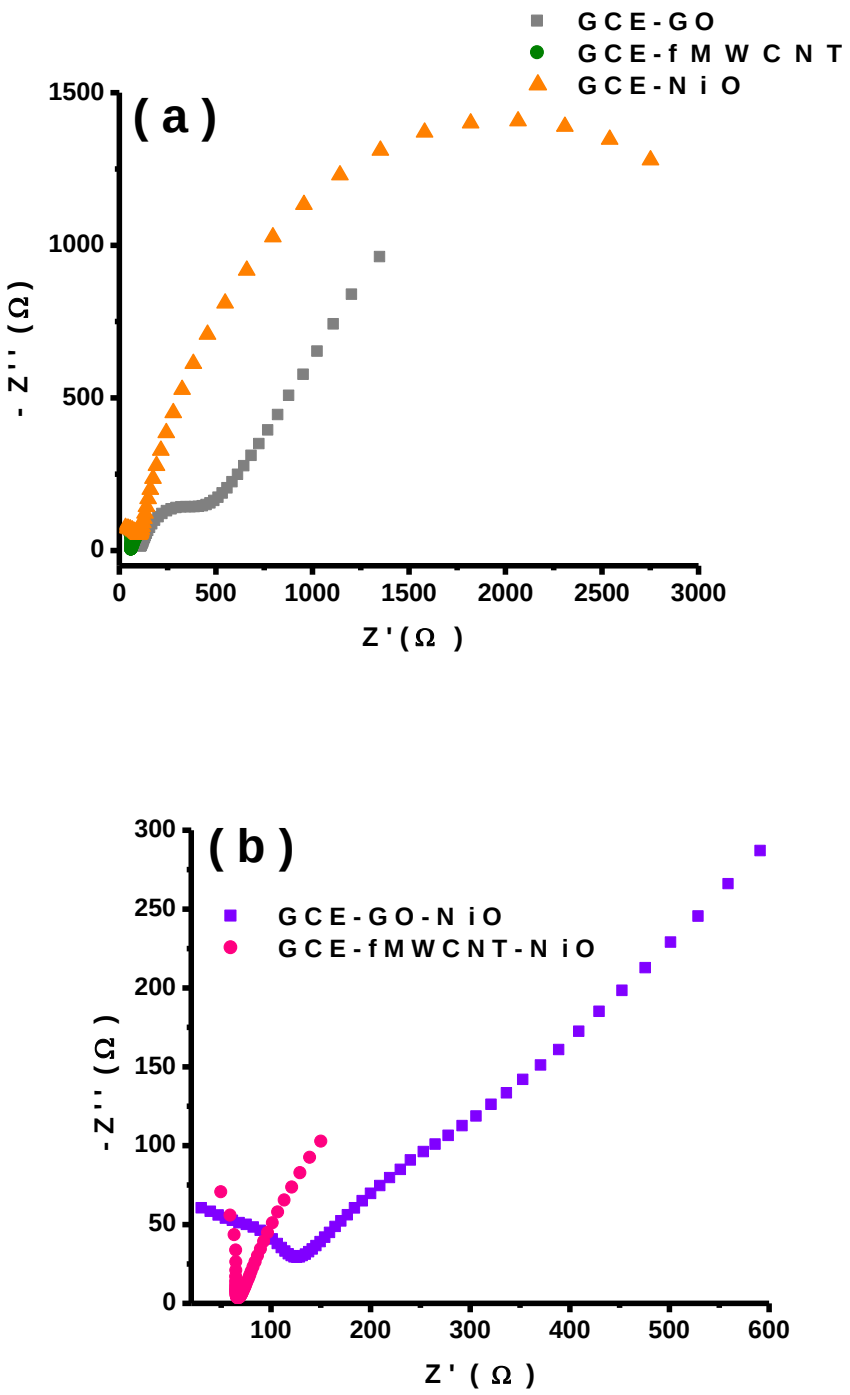

Figure 4.18.2: Comparative Nyquist plots obtained for the NiO based electrodes in 5 mM $[Fe(CN)\ 6]^{4-}$ / $[Fe(CN)\ 6]^{3-}$ solution (PBS pH 7.0) at a fixed potential of 0.2 V (vs Ag|AgCl, sat'd KCl).). (c) Compares the carbon nanomaterials and the metal oxide.

4.3 ELECTROCATALYTIC OXIDATION OF ANALYTE

4.3.1 Electrocatalytic Oxidation of Pyrene

The electrocatalytic response of the modified electrode to different concentrations of pyrene was studied in ethanol/water (1:5,*v:v*) with 1 M HCl as the supporting electrolyte. A potential window of 0.00 to +2000 mV with reference to Ag|AgCl electrode and a scan rate of 25 mV/s were the working conditions. Figure 4.19 (a) shows the cyclic voltammograms for GCE in 1 M HCl with and without 1 mM pyrene. This initial study was performed in order to determine the oxidation and reduction potentials of pyrene. In the presence of pyrene, a single anodic peak and no cathodic peak is observed, indicating that the electrocatalysis of Pyrene is an irreversible reaction. The current response is increased and the onset of oxidation is reduced (1780 to 1480 mV) to more negative oxidation potentials in the presence of pyrene.

Figure 4.19.1 (b) and figure 4.19.2 (a) show the comparative voltammograms of the (b) Co_3O_4 and (a) NiO nanoparticle based electrodes. In both cases, the modified electrodes are shown to have significantly enhanced the current response towards pyrene, when compared to the GCE. The carbon nanotube–metal oxide nanocomposite modified electrodes outperform the graphene oxide- metal oxide based electrodes. An interesting observation in the CVs for the electrocatalyis of pyrene for all the electrodes is that there is no distinct oxidation peak visible despite the fact that the oxidation of PAHs is irreversible. This can be attributed to the oxygen evolution reaction (OER). That is to say that because the OER starts at potentials much lower (~ 0.9-1 V) than those required for PAH oxidation (~ 1-2 V), any anodic peak generated by the oxidation of the PAH, would be masked by the large current generation caused by the oxygen evolution reaction [153]. The electrodes exhibit quasi-sigmoidal curves in the anodic region. This behaviour can be explained as a nanoscale phenomenon: that is to say that both the multi-walled carbon nanotubes and graphene oxide tend to behave like microelectrodes. The

fMWCNTs behave like low density nanoelectrode arrays; where each fMWCNT behaves like an individual electrode (figure 4.10.2 (d)) and displays the sigmoid CV which is typical of nanoelectrodes having radial diffusion and a steady state current [144] [154]. Similarly, the GO and GO-NiO electrodes exhibit quasi-sigmoidal voltammograms characteristic of radial diffusion at ultra-micro electrodes. This finding is reasonable because, the edges of the GO sheets essentially act like micro-electrodes (figure 4.9 (b) and (d)), the edges of the multilayer graphene oxide vary from ~3-40 µm, which is close to the length used to define an ultra-micro electrode (` 25µm) [155]. The same reasons cited for ultra-microelectrode-like behaviour of the fMWCNT-MO and GO-MO modified electrodes, can be used to explain the differences observed in the enhancement of the current response. These were cited in the preliminary experiment in the model outer-sphere redox probe *vide supra*.

It has been suggested that the rapid formation of a hydroquinone is responsible for the irreversible response observed in the cyclic voltammograms for each of the electrodes presented below [153]. Poly aromatic hydrocarbons can be electrochemically degraded via multiple steps: the process is initiated with a direct one electron transfer from the adsorbed PAH to the electrode to form cation radicals, followed by nucleophilic attack of water at the carbon atoms with the highest positive charge density and formation of hydroxyquinones and dihydroxyquinones and ultimately pyrene-1,6-dione and pyrene-1,8-dione [156]. A possible mechanism for the electro-oxidation of Pyrene is outlined in Scheme 4.1.

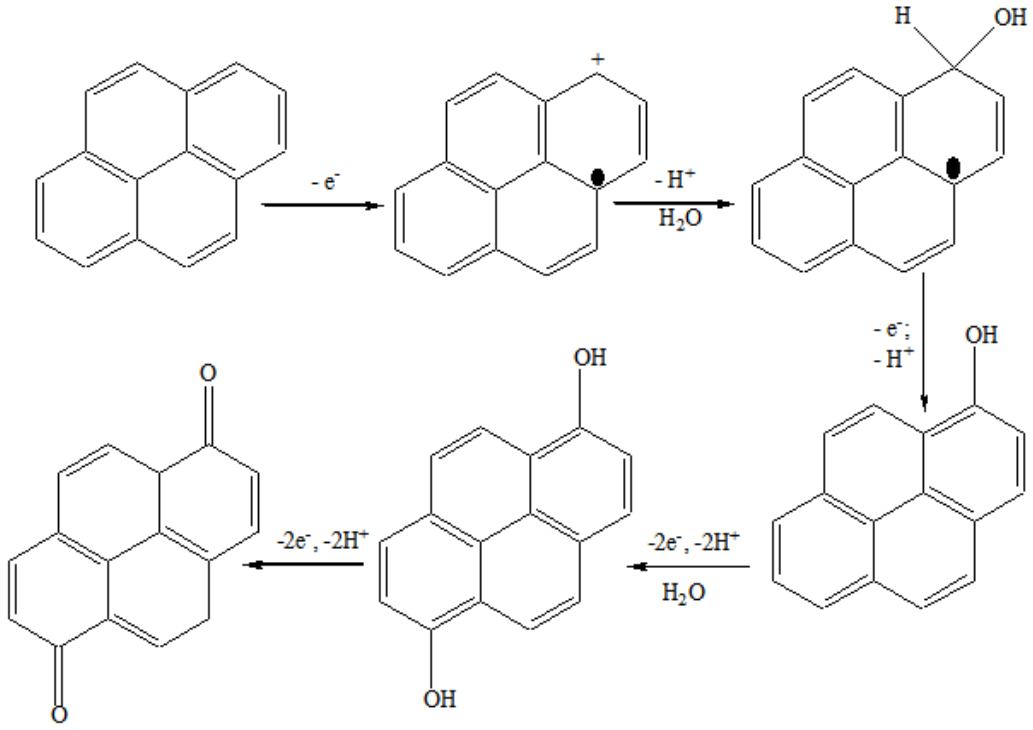

Scheme 4.1 : Proposed scheme for the oxidation of pyrene to pyrene-1,6- dione.

An important feature that is present in the cyclic voltammograms of all the electrodes is the prominent reduction peak that occurs between 0.5-1 V. This is attributed to the supporting electrolyte, where the chloride ions from the supporting electrolyte are reduced to form free chlorine (aqueous molecular chlorine), which combines with water to form hypochlorous acid, hydronium ions and regenerate the chloride ions [157, 158] . The reaction can be summarised as follows:

$$2Cl^- \rightarrow Cl_2 + 2e^-$$

$$Cl_2 + H_2O + 2e^- \rightarrow HOCl + H^+ + Cl$$

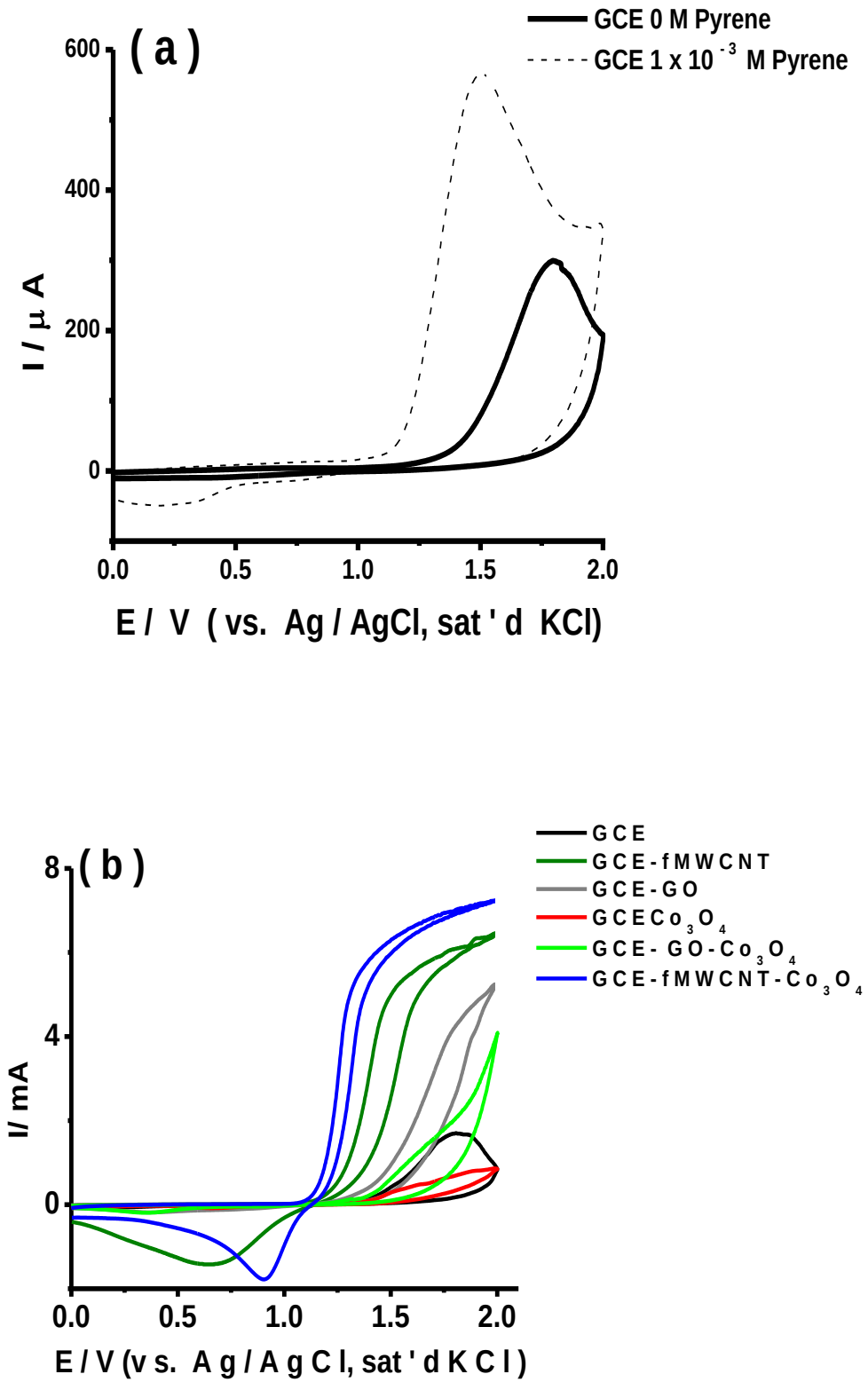

Figure 4.19.1: Cyclic voltammetric evolutions of (a) bare GCE in 1 mM (b) GO/fMWCNT/Co_3O_4 modified electrodes in 16 nM Pyrene solution in 1 M HCl (scan rate = 25 mVs^{-1}).

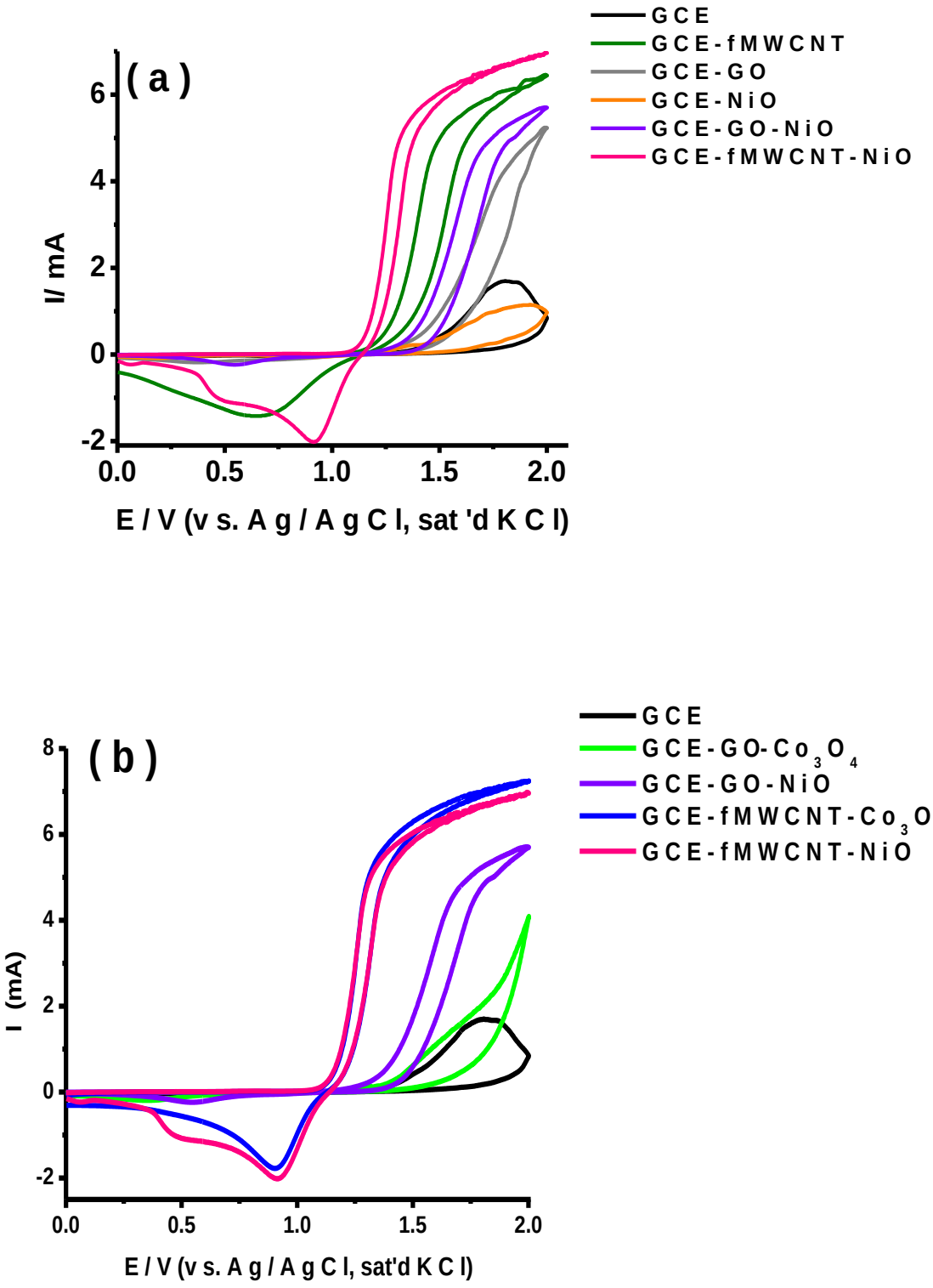

Figure 4.19.2: Cyclic voltammetric evolutions (a) GO/fMWCNT/NiO based and (b) nanocomposite modified electrodes in 16 nM Pyrene solution in 1 M HCl (scan rate =25 mVs^{-1}).

4.3.2 Electrochemical Impedance Spectroscopy (EIS) Studies of the Electrocatalytic Oxidation of Pyrene

Insight into the electrocatalytic oxidation of Pyrene at GCE-GO-Co_3O_4, GCE-GO-NiO GCE-fMWCNT-Co_3O_4 and GCE-fMWCNT-NiO modified electrodes was gained from the electrochemical impedance spectroscopy (EIS) technique. The Nyquist plots obtained for the various electrodes in Pyrene (at a fixed bias potential of 1.3 V vs. Ag/AgCl, sat'd KCl) at frequencies between 100 KHz and 0.1 Hz are presented in figure 4.20. The spectra were subjected to the Kramer-Konig (K-K) test. The impedance data were reasonably fitted with an equivalent circuit. The results are presented in Table 4.3. The circuit components in the model are R_s- solution resistance, C_{dl} represents the double layer capacitance, Z_w is the Warburg impedance and R_{ct} is the charge transfer resistance of the electrode.

From the EIS results presented in Table 4.3, it was found that the R_{ct} values for the nanocomposite electrode are significantly lower than the unmodified GCE. This indicates the modifying substrates' ability to create a pathway between the electrode and electrolyte for the movement of electrons. Once again, the fMWCNT-Co_3O_4 modified GCE exhibits outstanding electrochemical properties, and proves to be a good platform for sensing applications. Compared to the other nanocomposites, the combination of the acid treated MWCNT and Co_3O_4 creates a synergy that reduces the contact resistance (R_s) between the electrode and electrolyte and this translates into a significantly decreased R_{ct}; where the fMWCNT-Co_3O_4 enables much easier charge transfer at the electrode-electrolyte interface and thus boosts the electronic conductivity. This result is seen in the high electron transfer rate constant value (3.09 x 10^{-2} $cm.s^{-1}$) compared to the lowest seen for unmodified glassy carbon electrode (1.55 x 10^{-5} $cm.s^{-1}$).

The impedance spectra for the GO-MO modified GCE were rather complicated in that they have small, almost absent, disfigured semicircles in the high frequency region (figure 4.20.1 (b) Inset). These electrodes proved difficult to fit with the Randles model that describes the "true" Faradaic process (that is, true electron transfer in the interfacial region). The most suitable equivalent circuit model has the double layer capacitance (C_{dl}), Warburg impedance (Z_W) and charge transfer resistance (R_{ct}). This model yielded the most satisfactory results, considering the relative percentage error and χ^2. The EIS data obtained from fitting the equivalent circuit was obtained after several iterations. Upon perusal of the literature based on the detection of PAHs, it was found that the impedance behaviour of the electrocatalytic oxidation of Pyrene is sparse. Based on the electron transport study conducted using the model redox probe, it can be proposed that the complexity of the spectra obtained for GO-MO based electrodes can be ascribed to factors such as the electrode structure, interfacial properties of the multilayer graphene oxide as well as reaction kinetics. The near absence of a semicircle in the high frequency region could be as a result of the porosity of the metal oxides. This manifests as the absence of the solution resistance in the equivalent circuit model, implying that at high frequency, the semicircle portion may possibly intercept at the zero point of the real and imaginary axes (Figure 4.20.2 (a)). The GO-Co_3O_4 and GO-NiO modified electrodes both show overlapping lines inclined at a steep angle to the real axis indicative of a semi-finite linear diffusion related to the Warburg impedance. A peculiar observation is the fact that GO-Co_3O_4 has a lower charge transfer resistance and a higher electron transfer rate constant than GO-NiO. This result seems contrary to the results obtained in the CV. A possible explanation is the porous nature of the cobalt oxide nanoparticles that allow the pyrene and its intermediates to diffuse through the substrate towards the GCE. The combination of the high R_{ct} and C_{dl} values for the GO-MO substrates can be explained in terms of the adsorptive and adsorbent nature of PAHs and carbon nanomaterials, respectively. That is, Pyrene adsorbs onto the graphene oxide

via pi-pi interactions [159]. Graphene oxide possesses the open-layer structure that has a completely accessible adsorption surface for organic molecules. It has been demonstrated that the adsorption of PAHs onto carbon nanomaterials can be attributed to the existence of high surface energy sites, such as defects, edges and groove areas (like those on GO) , because molecules would occupy these sites with strong affinity [160], thus create a situation where electrons liberated during the oxidation of Pyrene are "blocked", and do not flow rapidly to the GCE, and thus the high charge transfer resistance observed. As mentioned previously, the steep diffusion lines in the low frequency regions indicate a pseudocapacitive behaviour that can also be attributed to the combination of the layered GO, PAH adsorbance and the oxygen groups attached to the edge planes of the GO. The capacitance (C_{dl}) is not purely capacitive and could be considered as C_{film} and the charge transfer resistance can be R_{ad} ; where C_{film} and R_{ad} are a consequence of the adsorption of the analyte and its intermediates (figure. 4.18) onto the electrode and C_{film} describes the high pseudocapacitive nature of the system [82, 161]. The appearance of kinetic (R_{ct}) and diffusion (Z_W) domains is indicative of mixed processes at the electrode/electrolyte interface, however, the long straight lines show that diffusion dominates in the GO-MO modified electrodes. The tendency of pyrene to adsorb onto the GO-MO electrodes would also affect the rate at which the electrons are transferred and this is seen in the lower k_s values cited in Table 4.3.

The impedance spectra obtained for the electro-oxidation process of pyrene at fMWCNT-Co_3O_4 and fMWCNT-NiO are presented in figure 4.20.2 (b). The fMWCNT based electrodes have similar impedance spectra. The fMWCNT-MO show small incomplete semicircles in the high frequency region (figure 4.20.1 (b (inset)) & figure 4.20.2 (a)). This is a consequence of the charge transfer resistance across the electrode/electrolyte interface. They show a nearly vertical line in the intermediate frequency region, which speaks of a combination of pseudocapacitive behaviour and diffusion controlled mass-transport. Visual inspection of the

diffusion lines of two electrodes shows that they are nearly parallel and have virtually equal slopes that are very large, which tells of a minimal diffusive resistance of the electrolyte in the electrode pores and diffusion of the analyte into the modifying nanocomposite . The transition point between the high and low frequency regions is commonly referred to as the "knee" or onset frequency (f_o). This is where the capacitive behaviour is dominant. This essentially describes the charge transferring capacity of the electrodes. That is to say: the higher the onset frequency, the more rapidly the capacitor (C_{dl}) can be charged and discharged [151]. Figure 4.20.2 (b) illustrates this clearly, with GCE-fMWCNT-Co_3O_4 having a knee at a higher frequency than GCE-fMWCNT-NiO. This translates to the fMWCNT-Co_3O_4 nanocomposite having the ability to transfer electron-charge more rapidly than the fMWCNT-NiO counterpart.

The results obtained using EIS indicate the improved electrical conductivity, enhanced electron transport and excellent electrocatalytic oxidation of Pyrene at the GCE-fMWCNT-Co_3O_4 electrodes, which validates the trend reported using cyclic voltammetry above.

Table 4.4 Impedance data obtained for the modified electrodes in 16 nM Pyrene solution in 1 M HCl at a fixed potential of 1.3 V (vs Ag|AgCl, sat'd KCl).

Electrodes	**R_S (Ω cm^2)**	**C_{dl} (μF)**	**R_{ct} (Ω cm^2)**	**Z_W (Ω cm^2)**	**k_s ($cm.s^{-1}$)**
GCE	29.6	0.389	15.25 x10^3	0.286 x 10^{-3}	1.55 x 10^{-5}
GCE-GO-Co_3O_4	-	0.256	452	0.450 x 10^{-3}	5.21 x 10^{-4}
GCE-GO-NiO	-	0.272	598	0.219 x 10^{-3}	3.94 x 10^{-4}
GCE-fMWCNT-Co_3O_4	12.0	98.8 x 10^{-3}	13.14	0.137 x 10^{-1}	3.09 x 10^{-2}
GCE-fMWCNT-NiO	18.44	68.1 x 10^{-3}	20.88	0.560 x 10^{-1}	2.36 x 10^{-2}

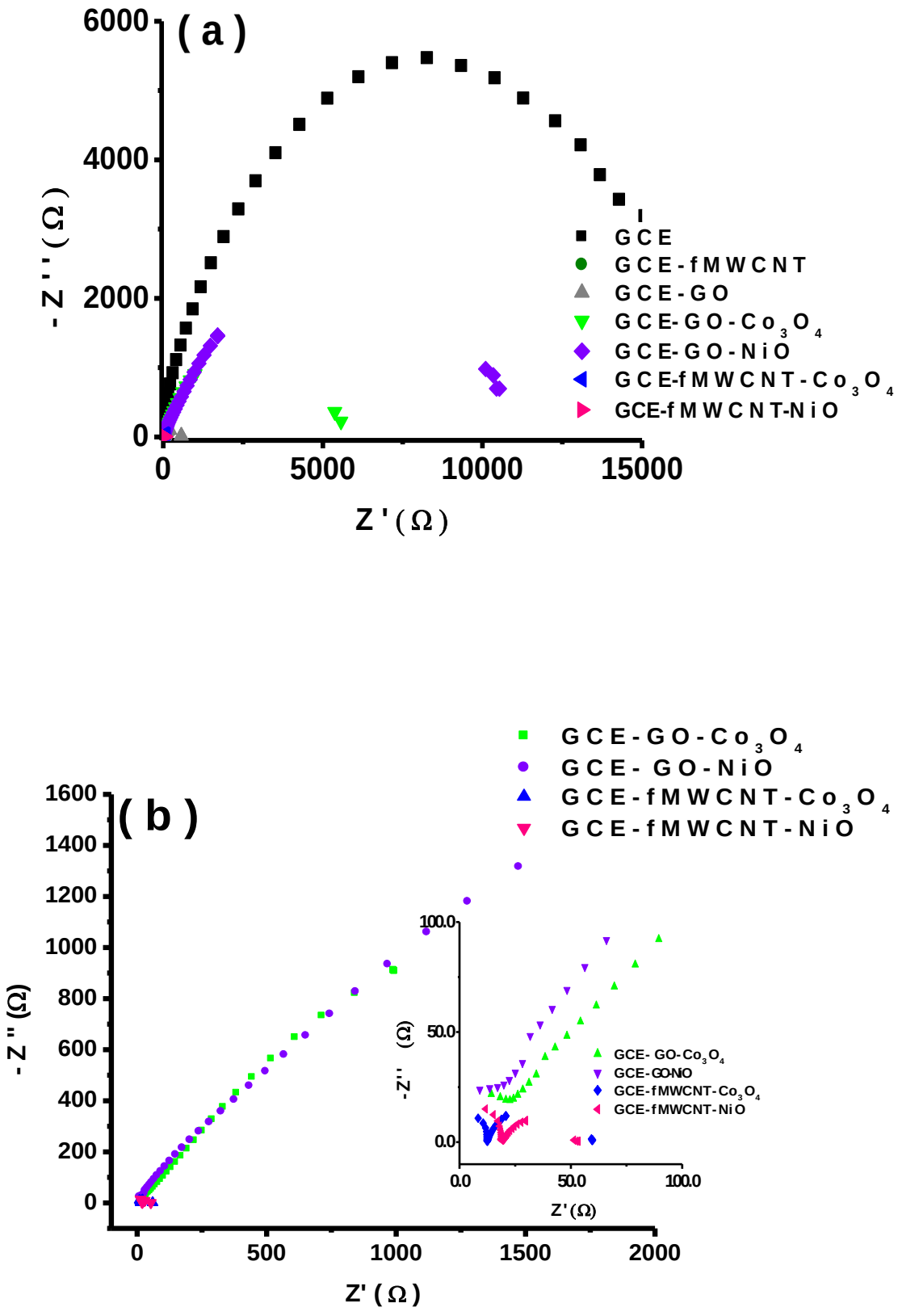

Figure 4.20.1: Comparative Nyquist plots obtained for (a) all electrodes, (b) nanocomposite modified electrodes in 16 nM Pyrene solution in 1 M HCl at a fixed potential of 1.3 V (vs Ag|AgCl, sat'd KCl).

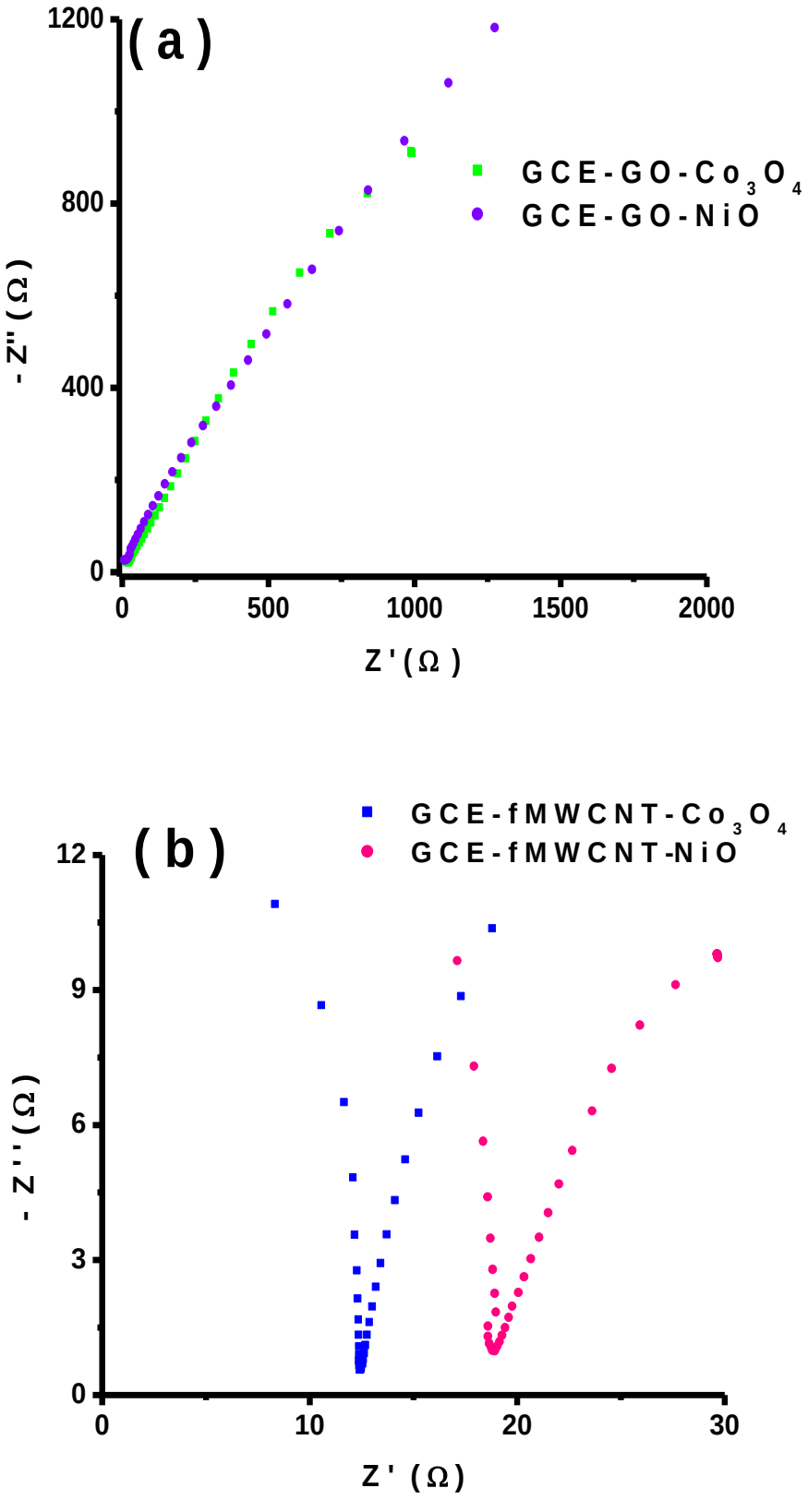

Figure 4.20.2: Comparative Nyquist plots obtained for (a) GO-Metal oxide nanocomposite and (b) fMWCNT-Metal oxide nanocomposite modified electrodes in 16 nM Pyrene solution in 1 M HCl at a fixed potential of 1.3 V (vs Ag|AgCl, sat'd KCl).

Since GCE-fMWCNT-Co_3O_4 has demonstrated excellent catalytic properties towards pyrene oxidation in this study, further studies were carried out using this electrode, unless otherwise stated.

4.3.3 Effect of Scan Rate on Pyrene oxidation

Cyclic voltammetric experiments were carried out with a view to assess the effect of the scan rate on the anodic peak current in 1 M HCl supporting electrolyte on a potential working window between 0-2.0 V using a constant concentration (1.0 x 10^{-3} M) of pyrene. It was found that the oxidation of pyrene on the GCE-fMWCNT-Co_3O_4 electrode (figure 4.21 (a)) displayed a linear increase in current with an increase in scan rate. At scan rates exceeding 250 mV/s, the oxidation current ceased to increase.

Based on Randles-Sevčik theory for an anodic oxidation process [162], the plot of anodic current (I_{pa}) versus the square root of the scan rate ($\upsilon^{1/2}$) (figure 4.21 (b)) yielded a linear regression of I_{pa} (mA) = 0.01455 $v^{1/2}$ ($mV^{1/2}. s^{-1/2}$)+ 4.8364, with a correlation coefficient of R^2 = 0.9852.

$$I_{p_a} = (2.99\, x\, 10^5) n[(1-\alpha)n]^{\frac{1}{2}} AC(Dv)^{1/2} \qquad 4.3$$

The deficient linearity and non-zero intercept, suggests that the process is in fact not completely controlled by the rate of diffusion of Pyrene from the solution to the surface of the electrode during the electro-oxidation. The results of the scan rate study for the oxidation of Pyrene indicate possible adsorption of the analyte and/ or oxidation product(s) to form a thin film or a fouling effect, as witnessed by the unchanging oxidation current with increasing scan rate beyond 250 mV/s [163].

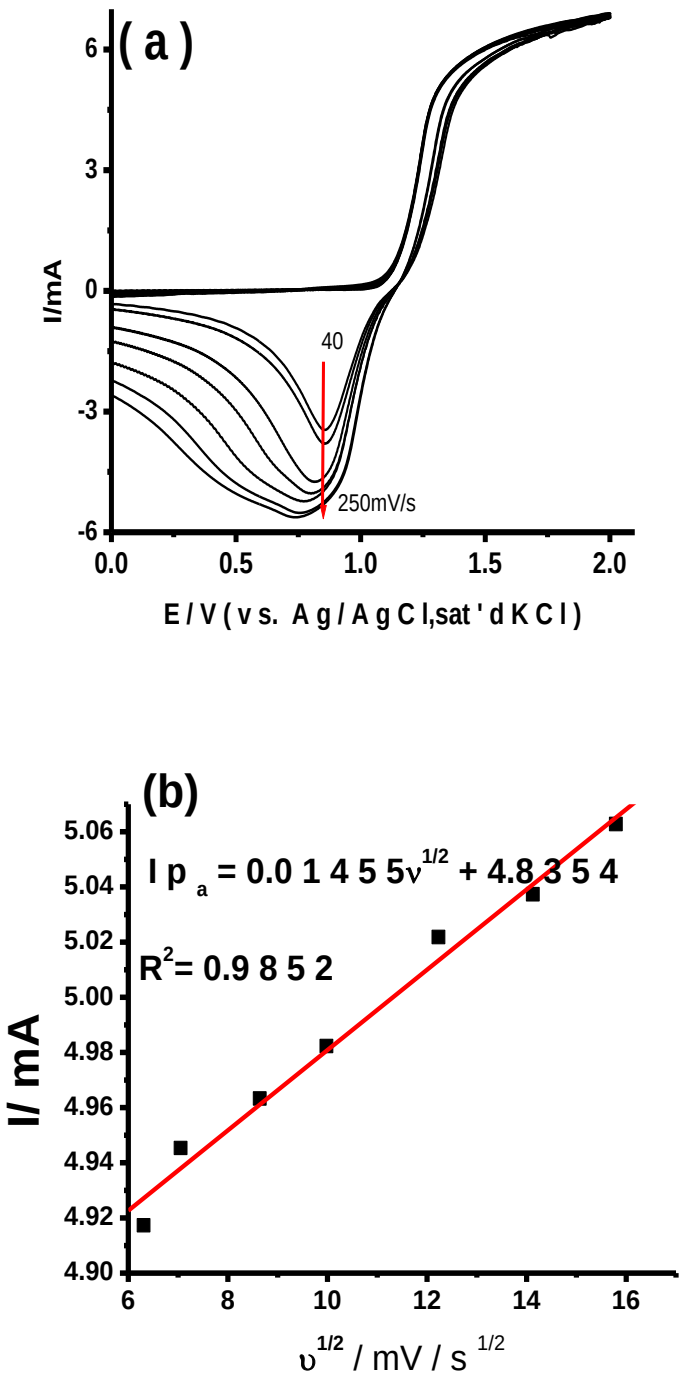

Figure 4.21: (a) Cyclic voltammetric evolutions of GCE-fMWCNT-Co_3O_4 electrode obtained in 1 M HCl containing 1.0 x 10^{-3} M Pyrene (scan rate 40-250 mV/s; inner to outer). (b) Plot of Anodic peak current dependence on scan rate.

Another observation made, was that the anodic potentials shifted positively with an increasing scan rate. This behaviour is indicative of an irreversible oxidation process [84].

The Tafel equation (4.4 and 4.5 below) was used to confirm the irreversibility of the diffusion dominated process for the electro-oxidation of Pyrene.

Using the Tafel equation for an irreversible-diffusion controlled process [73]

$$E_p = K + \frac{2.303\,RT}{2(1-\alpha)n_\alpha F}\log \nu \qquad 4.4$$

$$E_p = K + \frac{b}{2}\log \nu \qquad 4.5$$

Where α is the transfer coefficient, n_α is the number of electrons involved in the rate-determining step. *R*, *T* and *F* are the Molar gas constant; absolute temperature, and Faraday constant, respectively, *b* is the Tafel value.

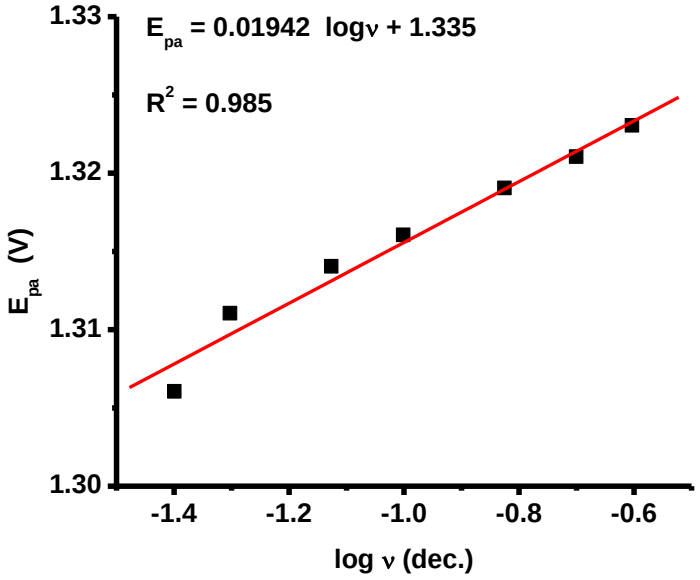

Figure 4.22: The Tafel plot for the electro-oxidation of 1 x 10^{-3} M Pyrene at GCE-fMWCNT-Co_3O_4 nanocomposite modified electrode in 1 M HCl (Scan rate 40-250 mV/s).

On the basis of $\Delta E_p/\Delta \log \nu$ slopes of the plot of E_p *vs*. log ν, the Tafel slope value was estimated at ~ 39mV/decade and α = 0.52. The Tafel slope value falls within the range of normal values (~ 30-120 mV/dec) for a single-electron process involved in the rate determining step[164].High Tafel slope values (> 120mV/dec for a one-electrode process) are associated with strong

binding of the analyte and/ or reaction intermediates to the electrode surface or reactions occurring within the porous electrode structure [165] . However, a Tafel slope of 120mV/decade suggest involvement of one electron in the rate determining step, whereas, the lower values, below ~ 60mV/decade indicate that a fast electron transfer is followed by a slow chemical step[166]. These findings are interesting in that, (i) the results of the scan rate study implied possible adsorption taking place, however, the low value of the Tafel slope obtained, suggests otherwise and advocates for a diffusion-controlled oxidation process (ii) the transfer coefficient (α) is associated with the potential energy transferred to a reaction and is one of the determining parameters for the rate of an electrochemical reaction (along with exchange current

i_o). It is theorized that the minimum value for α should be 0.5 for all standard electrochemical reaction mechanisms- because the transfer coefficient is effectively a measure of the symmetry of an energy barrier-, with α values greater than this, indicative of a better electrocatalytic mechanism [165, 167]. Thus, the α value estimated for the electro-oxidation of Pyrene implies that the catalyst used *viz*. GCE-fMWCNT-Co_3O_4 is indeed effective and there is an equal probability that the reaction activated transition state can form products or reactants [166].

4.4 ELECTROANALYSIS

4.4.1 Electroanalysis of Pyrene

The effect of varying the concentration of Pyrene on anodic current response was studied using the fMWCNT-Co_3O_4 modified glassy carbon electrode. The cyclic voltammetric analysis of the modified electrode is illustrated in figure 4.23 (a). The electro-oxidation was performed in ethanol/water (80:20, *v/v*) with 1 M HCl as a supporting electrolyte, between 0.0 and +2000 mV

potential working window at a 25mV/s scan rate. The anodic crest observed at ~ 1.284 V shifts negatively and increases at increasing concentrations of Pyrene. A calibration curve plot based on the anodic current *versus* concentration is presented in figure 4.23 (b). It was found to show satisfactory linearity over a range of concentrations from 1.0 x 10^{-9} – 100x 10^{-9} M, with a correlation coefficient of R^2 = 0.9997.

The detection limit was calculated based on the relationship:

$$\text{LOD} = {}^{3.3\,\delta}/_{m} \qquad 4.6$$

Where δ is the relative standard deviation of the intercept of the y-coordinates from the line of best fit, and *m* the slope of the same line[168]. The limit of detection, limit of quantification and sensitivity of the GCE-fMWCNT-Co_3O_4 electrode towards Pyrene is 1.62 x 10^{-9} M, 4.90 x 10^{-9} M and 4.5µA.nM^{-1} respectively, which establishes that the acid treated MWCNT cobalt oxide nanocomposite modified electrode has good electrocatalytic activity for the electro-oxidation of pyrene. The values reported herein for pyrene are an order of magnitude greater than those reported by Tovide 0.132pM, on a glassy carbon electrode modified with a polyaniline-tungsten oxide- graphene nanocomposite, using cyclic voltammetry [169].

The difference in the LoD values obtained could be attributed to the different electrode modifying substrates used, the different experimental conditions and their degree of interaction with the analytes.

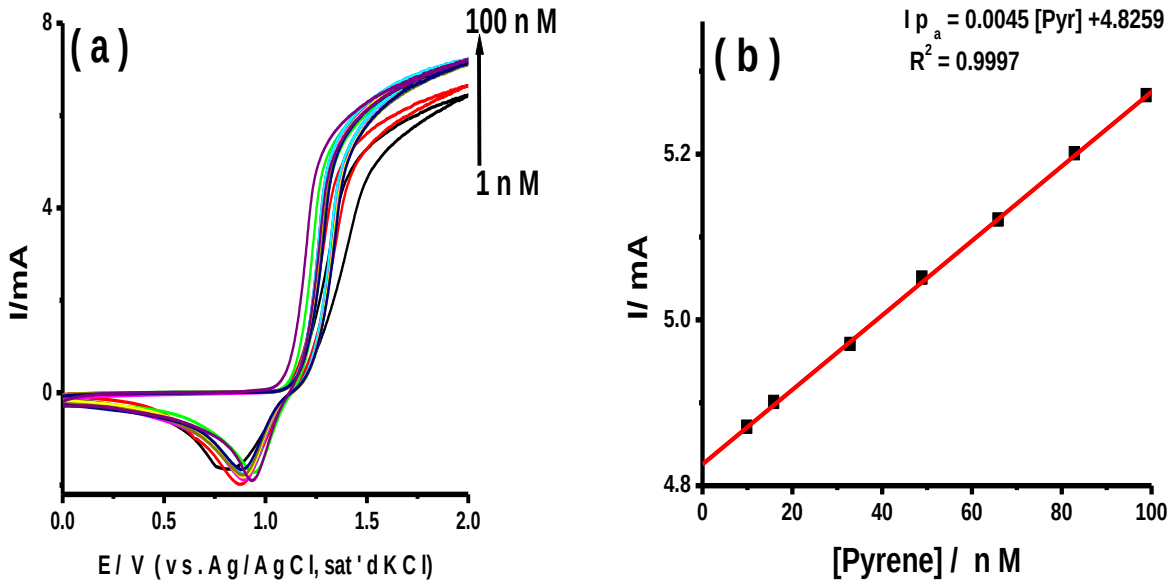

Figure 4.23: (a) Cyclic voltammetric evolutions of GCE-fMWCNT-Co_3O_4 in increasing concentrations of Pyrene at 25mV/s. (b) Shows a calibration plot for the GCE-fMWCNT-Co_3O_4 sensor showing current response *vs.* Pyrene concentration**.**

Based on the adsorbing and adsorbent nature of both the analyte and the substrate materials [170] and the somewhat inconsistent results in as far as the mass-transport/ interfacial region oxidation process goes, and the observed tendency towards saturation/ fouling of the electrode during the scan rate and concentration study, the Langmuir adsorption isotherm was employed , using data from the concentration study above, to monitor the extent of adsorption of the analyte at different concentrations. Using Langmuir adsorption theory, (eqn 4.7) [171].

$$\frac{[Pyrene]}{I_P} = \frac{1}{\beta I_P} + \frac{[Pyrene]}{I_P} \qquad 4.7$$

Where [Pyrene] is the concentration of Pyrene, I_p is the anodic current and β is the adsorption equilibrium constant.

The plot of $^{[Pyrene]}/_{Ip}$ *vs*. [Pyrene] yields a straight line which serves to confirm the presence of adsorption during the electrochemical process.

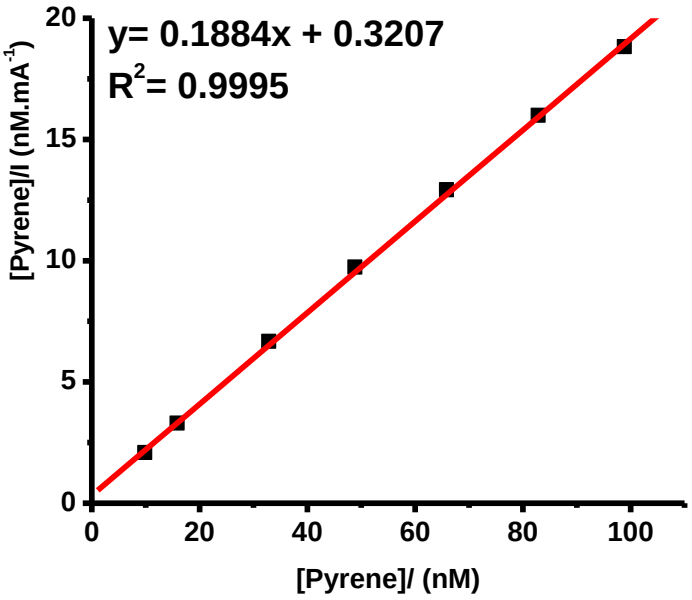

Figure 4.24 : Analysis of the anodic current and Pyrene concentration at a GCE-fMWCNT-Co_3O_4 modified electrode using the Langmuir equation and the data obtained in Figure 4.23

Furthermore, the adsorption equilibrium constant, β, for the GCE-fMWCNT-Co_3O_4 obtained from the slope and intercept of the Langmuir adsorption isotherm was found to be 5 .8 7 x 10^2 M^{-1}.

The relationship:

$$\Delta G^{O}_{ads} = -RT\ ln\beta \qquad 4.8$$

Where R and T are the Molar gas constant and absolute temperature and $\Delta G_{ads}{}^{o}$ is the Gibbs free energy change due to adsorption.

$\Delta G_{ads}{}^{o}$ was estimated at - 15.8 kJ/mol. The Gibbs free energy of adsorption is a very informative parameter in as far as understanding the type of adsorption occurring. The negative value indicates spontaneous adsorption of Pyrene onto the electrode. The magnitude of $\Delta G_{ads}{}^{o}$ is smaller than 40 kJ/mol. It has been cited that negative values of 20 kJ/ mol or less are ascribed to an electrostatic interaction between the charged molecules and the charged

metal- a phenomenon known as physisorption. $\Delta G_{ads}{}^{o}$ values of 40 kJ/mol or higher involve a situation in which organic molecules either share or transfer charge to the electrode surface to form a coordinate type bond. This is known as chemisorption. The value estimated herein (-15.8 kJ/mol) is indicative of a spontaneous electrostatic interaction between the analyte and the electrode substrate- physisorption, which supports the findings of adsorption occurring despite a diffusion dominated electrooxidation process [170, 172]. This is not an unreasonable conclusion because Pyrene has strong hydrophobic and π- electron transfer characteristics and as such has been employed as a "glue" material for carbon nanotubes- where it was found that SWCNT and Pyrene both aggregate heavily in aqueous media and give rise to remarkably stable SWCNT-Pyrene^{+} hybrids [173].

CHAPTER 5

CONCLUSION AND RECOMMENDATIONS

5.1 CONCLUSION

The aim of the research conducted herein to develop a method for the detection and quantification of Pyrene, has been achieved. The sensor was based on functionalised multi-walled carbon nanotubes and cobalt oxide nanocomposite synthesised using harsh acid treatments for the MWCNTs in order to functionalise with oxygen containing moieties such as carbonyl and carboxylic acid; and hydrothermal ammonium based precipitation was used for the synthesis of the metal oxide.

The electron transport and electrocatalytic properties of both the chemically synthesised metal oxides: Co_3O_4 and NiO; the carbon nanomaterials: graphene oxide and functionalised MWCNT that were used as grafting supports towards the electrocatalytic oxidation of the environmentally important molecules has been discussed.

The chemical synthesis and characterisation of the metal oxide and carbon nanomaterials has been presented. It was found that the multi-layer graphene oxide had flake sizes of ~ 46 nm and fMWCNT had diameters of ~9 nm as determined using XRD and TEM imaging, respectively. The metal oxides also had nanoscale dimensions of ~ 24 and 46 nm averages for NiO and Co_3O_4 particles, respectively, as estimated by XRD and TEM. These were used for subsequent experiments.

The morphology and spectroscopic characterisation of the nanocomposite materials were studied using a variety of characterisation techniques such as EDX, SEM and TEM. Electrochemical properties were evaluated using electrochemical impedance spectroscopy and cyclic voltammetry. The characterisation techniques confirmed the successful preparation of the nanocomposite materials and their immobilization onto the glassy carbon electrode.

The electrochemical measurements obtained in phosphate buffer and ferro/ferricyanide model redox probe revealed that the acidified multi-walled carbon nanotubes showed well defined redox peaks with a larger current response when compared to graphene oxide. Similarly, the cobalt oxide performed better than nickel oxide. The properties observed for the carbon nanomaterials and metal oxides were conveyed to the nanocomposites where the cobalt oxide and nickel oxide supported on carbon nanotubes performed better than the metal oxides supported on graphene oxide.

It was shown that a glassy carbon electrode, modified with graphene oxide and functionalised multi-walled carbon nanotubes decorated with nickel oxide and cobalt oxide nanoparticles, exhibits enhanced voltammetric and electrochemical response for the electro-oxidation of pyrene in acidic aqueous medium, with hydrochloric acid as a supporting electrolyte. The electrocatalysis of pyrene was successful on all the electrodes studied. The GCE-fMWCNT-Co_3O_4 showed electrochemical characteristics that exceeded those of GCE-fMWCNT-NiO,

GCE-GO-Co_3O_4 and GCE-GO-NiO, and outperformed these electrodes in as far as the electrocatalytic oxidation of Pyrene was concerned.

The fact that the fMWCNT-Co_3O_4 nanocomposite modified electrode showed the fastest electron transport as well as the best electrocatalytic behaviour towards Pyrene compared with other electrodes can be ascribed to the highly electrically conductive MWCNT that form a synergy with the cobalt oxide nanoparticles.

Application of the electrode as a sensor in aqueous media for the detection of Pyrene had a linear dynamic range of 1.0- 100.0 nM and a Limit of detection (LoD) of 1.62 nM. The GCE-fMWCNT-Co_3O_4 electrode exhibited excellent sensitivity towards the detection of Pyrene.

The charge transfer resistance, electron transfer, rate constant (k_s), Tafel value, limit of detection (LoD), sensitivity, adsorption equilibrium constant (β), Gibbs free energy change due to adsorption (ΔG_{ads}) of pyrene onto the GCE-fMWCNT-Co_3O_4 electrode was established and discussed. Analysis of the anodic current and pyrene concentration fitted the Langmuir adsorption isotherm.

Not only does the work presented herein provide a method for the development of a sensitive sensor for the detection of Pyrene, but it is a natural progression to a viable route for the green degradation of PAHs and other persistent organic pollutants via electrocatalytic oxidation.

5.2 RECOMMENDATIONS

The work presented herein provides a platform for the development of a sensitive method for the detection of pyrene.

The following recommendations are proposed:

(i) The careful control of the morphology and size of the metal oxides, because it has been found that the shape, size and uniformity of metal oxides improves their catalytic ability;

(ii) Optimization of the experimental conditions because they are key to the performance of electrodes, especially with regard to factors such as pH, supporting electrolyte, solvent used etc.;

(iii) The development of the PAH sensor using other electrodes such as screen and paper printed electrodes;

(iv) Further studies on other classes of persistent organic pollutants, such as the organochlorine pesticides and poly brominated biphenyls.

REFERENCES

1. Wong, M. H.; Leung, A. O. W.; Chan, J. K. Y.; Choi, M. P. K. A review on the usage of POP pesticides in China, with emphasis on DDT loadings in human milk. *Chemosphere* 2005, 60, 740-752.

2. Jones, K. C.; de Voogt, P. Persistent organic pollutants (POPs): state of the science. *Environmental Pollution* 1999, 100, 209-221.

3. Gevao, B.; Alegria, H.; Jaward, F. M.; Beg, M. U. Persistent Organic Pollutants in the Developing World. In *Persistent Organic Pollutants*. Harrad, S., Ed; Blackwell Publishing Ltd. John Wiley & Sons: United Kingdom, 2010.

4. de Cruz, I.; Mougin, C.; Grolleau, G. r. Chlorinated hydrocarbons in eggs of grey heron (Ardea cinerea L.) in France (Lac de Grandlieu). *Chemosphere* 1997, 35, 1003-1009.

5. El-Shahawi, M. S.; Hamza, A.; Bashammakh, A. S.; Al-Saggaf, W. T. An overview on the accumulation, distribution, transformations, toxicity and analytical methods for the monitoring of persistent organic pollutants. *Talanta* 2010, 80, 1587-1597.

6. Pauwels, A.; Covaci, A.; Weyler, J.; Delbeke, L.; Dhont, M.; De Sutter, P.; D'Hooghe, T.; Schepens, P. J. C. Comparison of Persistent Organic Pollutant Residues in Serum and Adipose Tissue in a Female Population in Belgium, 1996-1998. *Archives of Environmental Contamination and Toxicology* 2000, 39, 265-270.

7 Zani, C.; Gelatti, U.; Donato, F.; Capelli, M.; Portolani, N.; Bergonzi, R.; Apostoli, P. Polychlorinated biphenyls in serum, liver and adipose tissue of subjects with hepatocellular carcinoma living in a highly polluted area. *Chemosphere* 2013, 91, 194-199.

8. UNEP (United Nations Environment Programme). Guidance on the Global Monitoring Plan for Persistent Organic Pollutants; Africa Region, 2009; Draft Report. [Online]. Available: http://www.pops.int/documents/meetings/cop_3/meetingdocs/inf14/GMP%20Guidance%20CD/Guidance.pdf.

9. Ministry of Trade and Industry. Development Of Chemical Testing Laboratory Capacity To Expand The Scope Of Good Laboratory Practise Compliant Testing Facilities. Department of Trade and Industry, Enterprise and Industry Development Division RSA, Republic Of South Africa, Pretoria, 2007.

10. Li, G.; Miao, P. Theoretical Background of Electrochemical Analysis. In *Electrochemical Analysis of Proteins and Cells*; Springer Briefs in Molecular Science; Springer Science & Business Media: Berlin, Heidelberg, 2013; pp 5-18.

11. Balzani, V. Nanoscience and nanotechnology: a personal view of a chemist. *Small* 2005, 1, 278-283.

12. Welch, C.; Compton, R. The use of nanoparticles in electroanalysis: a review. *Analytical and Bioanalytical Chemistry* 2006, 384, 601-619.

13. Rassaei, L.; Marken, F.; Sillanpaa, M.; Amiri, M.; Cirtiu, C. M.; Sillanpaa, M. Nanoparticles in electrochemical sensors for environmental monitoring. *TrAC Trends in Analytical Chemistry* 2011,30, 1704-1715.

14. Jang, A.; Zou, Z.; Lee, K. K.; Ahn, C. H.; Bishop, P. L. State-of-the-art lab chip sensors for environmental water monitoring. *Measurement Science and Technology* 2011, 22, 032001.

15. Yang, Q.; Sun, Q.; Zhou, T.; Shi, G.; Jin, L. Determination of Parathion in Vegetables by Electrochemical Sensor Based on Molecularly Imprinted Polyethyleneimine/Silica Gel Films. *Journal of Agricultural and Food Chemistry* 2009, 57, 6558-6563.

16. Farghaly, O.; Hameed, R. A.; Abu-Nawwas, A.-A. H. Analytical Application Using Modern Electrochemical Techniques. *International Journal of Electrochemical Science* 2014, 9, 3287-3318.

17. Dong, X.-C.; Xu, H.; Wang, X.-W.; Huang, Y.-X.; Chan-Park, M. B.; Zhang, H.; Wang, L.-H.; Huang, W.; Chen, P. 3D Graphene-Cobalt Oxide Electrode for High-Performance Supercapacitor and Enzymeless Glucose Detection. *ACS Nano 2012*, 6, 3206-3213.

18. Adekunle, A. S.; Ozoemena, K. I.; Agboola, B. O. MWCNTs/metal (Ni, Co, Fe) oxide nanocomposite as potential material for supercapacitors application in acidic and neutral media. *Journal of Solid State Electrochemistry* 2013, 17, 1311-1320.

19. Eduljee, G. H. Chapter 1, Budget and Source Inventories: Issues and Challenges. In *Persistent organic pollutants: Environmental behaviour and pathways of human exposure,* Harrad, S. Ed. Kluwer Academic Publishers, Springer Science & Business Media: London 2001, pp 1-26.

20. Kim, S.-K.; Khim, J. S.; Lee, K.-T.; Giesy, J. P.; Kannan, K.; Lee, D.-S.; Koh, C.-H. Emission, Contamination and Exposure, Fate and Transport, and National Management Strategy of Persistent Organic Pollutants in South Korea. In *Developments in Environmental Science*; Li, A; Tanabe, S.; Jiang, G.; Giesy, J. P.; Lam, P.K. S., Eds. Elsevier: 2007; Vol.7; pp 31-157.

21. Ravindra, K.; Sokhi, R.; Van Grieken, R. Atmospheric polycyclic aromatic hydrocarbons: Source attribution, emission factors and regulation. *Atmospheric Environment* 2008, 42, 2895-2921.

22. Dabestani, R.; Ivanov, I. N. A Compilation of Physical, Spectroscopic and Photophysical Properties of Polycyclic Aromatic Hydrocarbons. *Photochemistry and Photobiology* 1999, 70, 10-34.

23. Jiao, L.; Zheng, G. J.; Minh, T. B.; Richardson, B.; Chen, L.; Zhang, Y.; Yeung, L. W.; Lam, J. C. W.; Yang, X.; Lam, P. K. S.; Wong, M. H. Persistent toxic substances in remote lake and coastal sediments from Svalbard, Norwegian Arctic: Levels, sources and fluxes. *Environmental Pollution* 2009, 157, 1342-1351.

24. Neff, J. M. *Polycyclic aromatic hydrocarbons in the aquatic environment: sources, fates, and biological effects.* Applied Science Publishers Ltd. : Essex, England 1979; p 262.

25. Henner, P.; Schiavon, M.; Morel, J.-L.; Lichtfouse, E. Polycyclic aromatic hydrocarbon (PAH) occurrence and remediation methods. *Analusis* 1997, 25, M56-M59.

26. Eisler, R. *Polycyclic Aromatic Hydrocarbon Hazards to Fish, Wildlife, and Invertebrates: A Synoptic Review.* U. S. Fish and Wildlife Service. Biological Report 1987, 85 (1.11).

27. National Research Council Canada, *Polycyclic Aromatic Hydrocarbons in the Aquatic Environment: Formation, Sources, Fate and Effects on Aquatic Biota*. Report No. 18981; NRCC: Canada, 1983.

28. Atwater, J.W.; Mavinic, D. S. Determination of trace organic compounds in Canadian coal wastewater and wastewater sludges. Department of Civil Engineering, Environmental Engineering Group, The University of British Columbia, Vancouver, B.C. 1985

29. Nagpal, N. K. *Ambient Water Quality Criteria For Polycyclic Aromatic Hydrocarbons (PAHs)*. Ministry of Environment, Lands and Parks, Water Quality Branch; Water Management Division, British Columbia, 1993.

30. Brown, J. R.; Thornton, J. L. Percivall Pott (1714-1788) and Chimney Sweepers' Cancer of the Scrotum. *British Journal of Industrial Medicine* 1957, 14, 68-70.

31. Grimmer, G.; Jacob, J.; Naujack, K.-W. Profile of the polycyclic aromatic compounds from crude oils. *Fresenius' Zeitschrift Fuer Analytische Chemie* 1983, 314, 29-36.

32. Grimmer, G.; Brune, H.; Deutsch-Wenzel, R.; Dettbarn, G.; Misfeld, J.; Abel, U.; Timm, J. The contribution of polycyclic aromatic hydrocarbons to the carcinogenic impact of emission condensate from coal-fired residential furnaces evaluated by topical application to the skin of mice. *Cancer letters* 1984, 23, 167-176.

33. Boström, C.-E.; Gerde, P.; Hanberg, A.; Jernström, B.; Johansson, C.; Kyrklund, T.; Rannug, A.; Törnqvist, M.; Victorin, K.; Westerholm, R. Cancer risk assessment, indicators, and guidelines for polycyclic aromatic hydrocarbons in the ambient air. *Environmental Health Perspectives* 2002, 110, 451-488.

34. Ravindra, K.; Mittal, A. K.; Van Grieken, R. Health risk assessment of urban suspended particulate matter with special reference to polycyclic aromatic hydrocarbons: a review. *Reviews on Environmental Health* 2001, 16, 169-189.

35. Ramírez, N.; Cuadras, A.; Rovira, E.; Maria Marcé, R.; Borrull, F. Risk assessment related to atmospheric polycyclic aromatic hydrocarbons in gas and particle phases near industrial sites. *Environmental Health Perspectives* 2011, 119, 1110.

36. Busbee, D.; Norman, J.; Ziprin, R. Comparative uptake, vascular transport, and cellular internalization of aflatoxin-B1 and benzo (a) pyrene. *Archives of Toxicology* 1990, 64, 285-290.

37. Santodonato, J. Review of the estrogenic and antiestrogenic activity of polycyclic aromatic hydrocarbons: Relationship to carcinogenicity. *Chemosphere* 1997, 34, 835-848.

38. International Agency for Research on Cancer. IARC Monographs on the Evaluation of Carcinogenic Risks to Humans: Some Non-heterocyclic Polycyclic Aromatic Hydrocarbons and Some Related Exposures. Vol. 92. IARC: Lyon, France, 2010.

39. Schroeder, H. Developmental Brain and Behaviour Toxicity of Air Pollutants: A Focus on the Effects of Polycyclic Aromatic Hydrocarbons (PAHs). *Critical Reviews in Environmental Science and Technology* 2011, 41, 2026-2047.

40. Niu, Q.; Zhang, H.; Li, X.; Li, M. Benzo[a]pyrene-induced neurobehavioral function and neurotransmitter alterations in coke oven workers. *Occupational and Environmental Medicine* 2010, 67, 444-448.

41. Malcolm, H. M.; Shore, R. F. Effects of PAHs on Terrestrial and Freshwater Birds, Mammals and Amphibians. In *PAHs: An Ecotoxicological Perspective*, Douben, P. E., Ed. John Wiley & Sons, Ltd: 2003; pp 225-241.

42. Ma, W. C.; Immerzeel, J.; Bodt, J. Earthworm and Food Interactions on Bioaccumulation and Disappearance in Soil of Polycyclic Aromatic Hydrocarbons: Studies on Phenanthrene and Fluoranthene. *Ecotoxicology and Environmental Safety* 1995, 32, 226-232.

43. Hallett, D. J.; Brecher, R. W. Cycling of polynuclear aromatic hydrocarbons in the Great Lakes ecosystem [Water pollution, fish toxicity]. *Advances in Environmental Science and Technology* 1984.

44. Peakall, D.; Hallett, D.; Bend, J.; Foureman, G.; Miller, D. Toxicity of Prudhoe Bay crude oil and its aromatic fractions to nestling herring gulls. *Environmental Research* 1982, 27, 206-215.

45. Hough, J. L.; Baird, M. B.; Sfeir, G. T.; Pacini, C. S.; Darrow, D.; Wheelock, C. Benzo(a)pyrene enhances atherosclerosis in White Carneau and Show Racer pigeons. *Arteriosclerosis, Thrombosis, and Vascular Biology* 1993, 13, 1721-7.

46. Dickerson, R.; Hooper, M.; Gard, N. Cobb G and Kendall R (1994) Toxicological foundations of ecological risk assessment: biomarker development and interpretation based upon laboratory and wildlife species. *Environmental Health Perspectives* 102, 65-69.

47. Blondin, O.; Viau, C. Benzo (a) pyrene-blood protein adducts in wild woodchucks used as biological sentinels of environmental polycyclic aromatic hydrocarbons contamination. *Archives of Environmental Contamination and Toxicology* 1992, 23, 310-315.

48. Rappe, C. Chemical behavior of pesticides. In *Ecological Problems of the Circumpolar Area,* Bylund, E.; Linderholm, H.; Rune, O. eds. Lulea, Sweden: Norrbottens Museum, 1974, pp. 29–32, 1974.

49. Wania, F.; Mackay, D. Global Fractionation and Cold Condensation of Low Volatility Organochlorine Compounds in Polar Regions. *Ambio* 1993, 22, 10-18.

50. Wania, F.; MacKay, D. Peer Reviewed: Tracking the Distribution of Persistent Organic Pollutants. *Environmental Science & Technology* 1996, 30, 390A-396A.

51. Niehaus, R.; Scheulen, B.; Dürbeck, H. W. Determination of airborne polycyclic aromatic hydrocarbons using a filter/adsorber combination. *Science of The Total Environment* 1990, 99, 163-172.

52. Moja, S. J.; Mtunzi, F.; Madlanga, X. Determination of polycyclic aromatic hydrocarbons (PAHs) in river water samples from the Vaal Triangle area in South Africa. *Journal of Environmental Science and Health, Part A* 2013, 48, 847-854.

53. Eisler, R. *Polycyclic Aromatic Hydrocarbon Hazards to Fish, Wildlife and Inverterbrates: A Synoptic Review.* US Department of Commerce, National Technical Information Service: 1987.

54. Edwards, N. T. Polycyclic aromatic hydrocarbons (PAH's) in the terrestrial environment—a review. *Journal of Environmental Quality* 1983, 12, 427-441.

55. Suess, M. J. The environmental load and cycle of polycyclic aromatic hydrocarbons. *Science of The Total Environment* 1976, 6, 239-250.

56. Lee, S. D., and L. Grant (Eds.). *Health and ecological assessment of polynuclear aromatic hydrocarbons*. Pathotex Publishers: Park Forest South, Illinois, 1981.

57. Huang, Z.; Natu, G.; Ji, Z.; Hasin, P.; Wu, Y. p-Type Dye-Sensitized NiO Solar Cells: A Study by Electrochemical Impedance Spectroscopy. *The Journal of Physical Chemistry C* 2011, 115, 25109-25114.

58. Waser, R.; Dittmann, R.; Staikov, G.; Szot, K. Redox-Based Resistive Switching Memories – Nanoionic Mechanisms, Prospects, and Challenges. *Advanced Materials* 2009, 21, 2632-2663.

59. Nuli, Y.-N.; Zhao, S.-L.; Qin, Q.-Z. Nanocrystalline tin oxides and nickel oxide film anodes for Li-ion batteries. *Journal of Power Sources* 2003, 114, 113-120.

60. Li, F.; Chen, H.-y.; Wang, C.-m.; Hu, K.-a. A novel modified NiO cathode for molten carbonate fuel cells. *Journal of Electroanalytical Chemistry* 2002, 531, 53-60.

61. Song, X.; Gao, L.; Mathur, S. Synthesis, Characterization, and Gas Sensing Properties of Porous Nickel Oxide Nanotubes. *The Journal of Physical Chemistry C* 2011, 115, 21730-21735.

62. Liu, X. M.; Zhang, X. G. NiO-based composite electrode with RuO2 for electrochemical capacitors. *Electrochimica Acta* 2004, 49, 229-232.

63. Salimi, A.; Sharifi, E.; Noorbakhsh, A.; Soltanian, S. Direct electrochemistry and electrocatalytic activity of catalase immobilized onto electrodeposited nano-scale islands of nickel oxide. *Biophysical Chemistry* 2007, 125, 540-548.

64. Quintino, M. d. S. M.; Winnischofer, H.; Nakamura, M.; Araki, K.; Toma, H. E.; Angnes, L. Amperometric sensor for glucose based on electrochemically polymerized tetraruthenated nickel-porphyrin. *Analytica Chimica Acta* 2005, 539, 215-222.

65. Fleischmann, M.; Korinek, K.; Pletcher, D. The kinetics and mechanism of the oxidation of amines and alcohols at oxide-covered nickel, silver, copper, and cobalt electrodes. *Journal of the Chemical Society*, Perkin Transactions 2 1972, 1396-1403.

66. Kumary, V. A.; Nancy, T. E.; Divya, J.; Sreevalsan, K. Nonenzymatic Glucose Sensor: Glassy Carbon Electrode Modified with Graphene-Nickel/Nickel Oxide Composite. *International Journal of the Electrochemical Society* 2013, 8, 2220-2228

67. Chen, Q.; Wang, J.; Rayson, G.; Tian, B.; Lin, Y. Sensor array for carbohydrates and amino acids based on electrocatalytic modified electrodes. *Analytical Chemistry* 1993, 65, 251-254.

68. Li, M.; Bo, X.; Mu, Z.; Zhang, Y.; Guo, L. Electrodeposition of nickel oxide and platinum nanoparticles on electrochemically reduced graphene oxide film as a nonenzymatic glucose sensor. *Sensors and Actuators B: Chemical* 2014, 192, 261-268.

69. Gu, C. D.; Huang, M. L.; Ge, X.; Zheng, H.; Wang, X. L.; Tu, J. P. NiO electrode for methanol electro-oxidation: Mesoporous vs. nanoparticulate. *International Journal of Hydrogen Energy* 2014, 39, 10892-10901.

70. Li, W. Y.; Xu, L. N.; Chen, J. Co3O4 Nanomaterials in Lithium-Ion Batteries and Gas Sensors. *Advanced Functional Materials* 2005, 15, 851-857.

71. Xie, X.; Shen, W. Morphology control of cobalt oxide nanocrystals for promoting their catalytic performance. *Nanoscale* 2009, 1, 50-60.

72. Guo, H.-j.; Sun, Q.-m.; Li, X.-h.; Wang, Z.-x.; Peng, W.-j. Synthesis and electrochemical performance of Co3O4/C composite anode for lithium ion batteries. *Transactions of Nonferrous Metals Society of China* 2009, 19, 372-376.

73. Schultze, J. W. Sergio Trasatti (Ed.): Electrodes of Conductive Metallic Oxides, Part A. *Berichte der Bunsengesellschaft für physikalische Chemie* 1981, 85, 461-462.

74. Salimi, A.; Hallaj, R.; Soltanian, S.; Mamkhezri, H. Nanomolar detection of hydrogen peroxide on glassy carbon electrode modified with electrodeposited cobalt oxide nanoparticles. *Analytica Chimica Acta* 2007, 594, 24-31.

75. Salimi, A.; Mamkhezri, H.; Hallaj, R.; Soltanian, S. Electrochemical detection of trace amount of arsenic(III) at glassy carbon electrode modified with cobalt oxide nanoparticles. *Sensors and Actuators B: Chemical* 2008, 129, 246-254.

76. Salimi, A.; Hallaj, R.; Mamkhezri, H.; Hosaini, S. M. T. Electrochemical properties and electrocatalytic activity of FAD immobilized onto cobalt oxide nanoparticles: Application to nitrite detection. *Journal of Electroanalytical Chemistry* 2008, 619–620, 31-38.

77. Kauffman, D. R.; Star, A. Carbon nanotube gas sensors and vapor sensors. *Angwandte Chemie International Edition* 2008, 47, 6550-6570.

78. Singh, V.; Joung, D.; Zhai, L.; Das, S.; Khondaker, S. I.; Seal, S. Graphene based materials: Past, present and future. *Progress in Materials Science* 2011, 56, 1178-1271.

79. Hummers, W. S.; Offeman, R. E. Preparation of Graphitic Oxide. *Journal of the American Chemical Society* 1958, 80, 1339-1339.

80. Biswas, C.; Lee, Y. H. Graphene Versus Carbon Nanotubes in Electronic Devices. *Advanced Functional Materials* 2011, 21, 3806-3826.

81. Wang, J.; Rogers, K. *Electrochemical sensors for environmental monitoring: a review of recent technology*. US Environmental Protection Agency, Office of Research and Development, Environmental Monitoring and Support Laboratory: 1995

82. Ebenso, E.; Adekunle, A.; Fayemi, E.; Olasunkanmi, L.; Ogunfowokan, R.; Oyekunle, J. A. O.; Boikanyo, D.; Ntsoaki, M.; Lebogang, S.; Gwala, P.; Tsele, T. Electrochemical Response of Nitrite and Nitric Oxide on Graphene Oxide Nanoparticles Doped with Prussian Blue (PB) and Fe_2O_3 Nanoparticles. *RSC Advances* 2015, 5, 27759-27774.

83. Tovide, O.; Jaheed, N.; Mohamed, N.; Nxusani, E.; Sunday, C. E.; Tsegaye, A.; Ajayi, R. F.; Njomo, N.; Makelane, H.; Bilibana, M.; Baker, P. G.; Williams, A.; Vilakazi, S.; Tshikhudo, R.; Iwuoha, E. I.

Graphenated polyaniline-doped tungsten oxide nanocomposite sensor for real time determination of phenanthrene. *Electrochimica Acta* 2014, 128, 138-148.

84. Mailu, S. N.; Waryo, T. T.; Ndangili, P. M.; Ngece, F. R.; Baleg, A. A.; Baker, P. G.; Iwuoha, E. I. Determination of anthracene on Ag-Au alloy nanoparticles/overoxidized-polypyrrole composite modified glassy carbon electrodes. *Sensors* 2010, 10, 9449-9465.

85. Rassie, C.; Olowu, R. A.; Waryo, T. T.; Wilson, L.; Williams, A.; Baker, P. G.; Iwuoha, E. I. Dendritic 7T-polythiophene electro-catalytic sensor system for the determination of polycyclic aromatic hydrocarbons. *International Journal of Electrochemical Science* 2011, 6, 1949-1967.

86. Liu, X.-Y.; Nakamura, C.; Nakamura, N.; Hirano, T.; Shinbo, T.; Miyake, J. Detection of polychlorinated biphenyls using an antibody column in tandem with a fluorescent liposome column: Effect of albumin on phospholipase A2-catalyzed membrane leakage. *Journal of Chromatography A* 2005, 1087, 229-235.

87. Haglund, P.; Korytár, P.; Danielsson, C.; Diaz, J.; Wiberg, K.; Leonards, P.; Brinkman, U. T.; de Boer, J. GC×GC-ECD: a promising method for the determination of dioxins and dioxin-like PCBs in food and feed. *Analytical and Bioanalytical Chemistry* 2008, 390, 1815-1827.

88. Buzitis, J.; Ylitalo, G. M.; Krahn, M. M. Rapid Method for Determination of Dioxin-Like Polychlorinated Biphenyls and Other Congeners in Marine Sediments Using Sonic Extraction and Photodiode Array Detection. *Archives of Environmental Contamination and Toxicology* 2006, 51, 337-346.

89. Wang, J.-X.; Jiang, D.-Q.; Gu, Z.-Y.; Yan, X.-P. Multiwalled carbon nanotubes coated fibers for solid-phase microextraction of polybrominated diphenyl ethers in water and milk samples before gas chromatography with electron-capture detection. *Journal of Chromatography A* 2006, 1137, 8-14.

90. Shimomura, M.; Nomura, Y.; Zhang, W.; Sakino, M.; Lee, K.-H.; Ikebukuro, K.; Karube, I. Simple and rapid detection method using surface plasmon resonance for dioxins, polychlorinated biphenylx and atrazine. *Analytica Chimica Acta* 2001, 434, 223-230.

91. McCreery, R. L. Raman spectroscopy for chemical analysis. In *Chemical Analysis: A Series of Monographs on Analytical Chemistry and Its Applications*; John Wiley & Sons: 2005; Vol. 225.

92. Zhang, L.; Fang, M. Nanomaterials in pollution trace detection and environmental `improvement. *Nano Today* 2010, 5, 128-142.

93. Loryuenyong, V.; Totepvimarn, K.; Eimburanapravat, P.; Boonchompoo, W.; Buasri, A. Preparation and Characterization of Reduced Graphene Oxide Sheets via Water-Based Exfoliation and Reduction Methods. *Advances in Materials Science and Engineering* 2013, 2013, 5.

94. Habibi, B.; Jahanbakhshi, M. Silver nanoparticles/multi walled carbon nanotubes nanocomposite modified electrode: Voltammetric determination of clonazepam. *Electrochimica Acta* 2014, 118, 10-17.

95. Datsyuk, V.; Kalyva, M.; Papagelis, K.; Parthenios, J.; Tasis, D.; Siokou, A.; Kallitsis, I.; Galiotis, C. Chemical oxidation of multiwalled carbon nanotubes. *Carbon* 2008, 46, 833-840.

96. Liu, J.; Rinzler, A. G.; Dai, H.; Hafner, J. H.; Bradley, R. K.; Boul, P. J.; Lu, A.; Iverson, T.; Shelimov, K.; Huffman, C. B.; Rodriguez-Macias, F.; Shon, Y.-S.; Lee, T. R.; Colbert, D. T.; Smalley, R. E. Fullerene Pipes. *Science* 1998, 280, 1253-1256.

97. Xiang, L. D., X.Y. Jin, Y. Experimental study on synthesis of NiO nano-particles. *Scripta Materialia* 2002, 47, 219-224.

98. Yao, W.; Yang, J.; Wang, J.; Tao, L. Synthesis and electrochemical performance of carbon nanofiber–cobalt oxide composites. *Electrochimica Acta* 2008, 53, 7326-7330.

99. Wang, J. *Analytical Electrochemistry,* 2nd ed. John Wiley & Sons Inc.: 2001, USA.

100. Boukamp, B. A. A Nonlinear Least Squares Fit procedure for analysis of immittance data of electrochemical systems. *Solid State Ionics* 1986, 20, 31-44.

101. Mudunkotuwa, I. A.; Minshid, A. A.; Grassian, V. H. ATR-FTIR spectroscopy as a tool to probe surface adsorption on nanoparticles at the liquid-solid interface in environmentally and biologically relevant media. *Analyst* 2014, 139, 870-881.

102. Coates, J. Interpretation of Infrared Spectra, A Practical Approach. In *Encyclopedia of Analytical Chemistry*, John Wiley & Sons, Ltd: 2006.

103. Marcano, D. C.; Kosynkin, D. V.; Berlin, J. M.; Sinitskii, A.; Sun, Z.; Slesarev, A.; Alemany, L. B.; Lu, W.; Tour, J. M. Improved Synthesis of Graphene Oxide. *ACS Nano* 2010, 4, 4806-4814.

104. Reich, S.; Thomsen, C. Raman spectroscopy of graphite. *Philosophical Transactions of the Royal Society of London A: Mathematical, Physical and Engineering Sciences* 2004, 362, 2271-2288.

105. Wang, Y.; Alsmeyer, D. C.; McCreery, R. L. Raman spectroscopy of carbon materials: structural basis of observed spectra. *Chemistry of Materials* 1990, 2, 557-563.

106. Masikini, M.; Mailu, S. N.; Tsegaye, A.; Ikpo, C. O.; Njomo, N.; Waryo, T. T.; Baker, P. G.; Iwuoha, E. I. In-situ Electrochemical Synthesis, Microscopic and Spectroscopic Characterisations of Electroactive poly (2, 5-dimethoxyaniline)–Multi-Walled Carbon Nanotubes Composite Films in Neutral Media. *International Journal of Electrochemical Science* 2014, 9, 7003-7020.

107. Bokobza, L.; Zhang, J. Raman spectroscopic characterization of multiwall carbon nanotubes and of composites. *Express Polymer Letters* 2012, 6, 601-608

108. Costa, S.; Borowiak-Palen, E.; Kruszynska, M.; Bachmatiuk, A.; Kalenczuk, R. Characterization of carbon nanotubes by Raman spectroscopy. *Materials Sciences-Poland* 2008, 26, 433-441

109. Kalantar-zadeh, K.; Fry, B. *Nanotechnology-Enabled Sensors*. Springer US, 2007.

110. Bhattacharyya, A.; Ali, S. W. Characterization techniques for nanotechnology applications in textiles. *Indian Journal of Fibre and Textile Research* 2008, 33, 304-317.

111. NanoComposix. UV/VIS/IR Spectroscopy Analysis of Nano. NanoComposix: San Diego, California, 2012; Vol. 2015, pp 1-6.

112. Paredes, J.; Villar-Rodil, S.; Martinez-Alonso, A.; Tascon, J. Graphene oxide dispersions in organic solvents. *Langmuir* 2008, 24, 10560-10564.

113. Genge, M. J.; Jones, A. P.; Price, G. D. An infrared and Raman study of carbonate glasses: mplications for the structure of carbonatite magmas. *Geochimica et Cosmochimica Acta* 1995, 59, 927-937.

114. Li, J.; Yan, R.; Xiao, B.; Liang, D. T.; Lee, D. H. Preparation of Nano-NiO Particles and Evaluation of Their Catalytic Activity in Pyrolyzing Biomass Components. *Energy & Fuels* 2007, 22, 16-23.

115. Adekunle, A. S.; Oyekunle, J. A.; Oluwafemi, O. S.; Joshua, A. O.; Makinde, W. O.; Ogunfowokan, A. O.; Eleruja, M. A.; Ebenso, E. Comparative Catalytic Properties of Ni (OH)2 and NiO Nanoparticles Towards the Degradation of Nitrite (NO2-) and Nitric Oxide (NO). *International Journal of Electrochemical Science* 2014, 9, 3008-3021.

116. Boschloo, G.; Hagfeldt, A. Spectroelectrochemistry of Nanostructured NiO. *The Journal of Physical Chemistry B* 2001, 105, 3039-3044.

117. Qi, Y.; Qi, H.; Li, J.; Lu, C. Synthesis, microstructures and UV–vis absorption properties of β-Ni(OH)2 nanoplates and NiO nanostructures. *Journal of Crystal Growth* 2008, 310, 4221-4225.

118. Zhao, T.; Jiang, H.; Ma, J. Surfactant-assisted electrochemical deposition of α-cobalt hydroxide for supercapacitors. *Journal of Power Sources* 2011, 196, 860-864.

119. Athar, T.; Hakeem, A.; Topnani, N.; Hashmi, A. Wet synthesis of monodisperse cobalt oxide nanoparticles. *ISRN Materials Science*, vol. 2012, Article ID 691032, 5 pages, 2012.

120. Salavati-Niasari, M.; Khansari, A.; Davar, F. Synthesis and characterization of cobalt oxide nanoparticles by thermal treatment process. *Inorganica Chimica Acta* 2009, 362, 4937-4942.

121. Al-Ghoul, M.; El-Rassy, H.; Coradin, T.; Mokalled, T. Reaction–diffusion based co-synthesis of stable α-and β-cobalt hydroxide in bio-organic gels. *Journal of Crystal Growth* 2010, 312, 856-862.

122. Gulino, A.; Dapporto, P.; Rossi, P.; Fragalà, I. A Novel Self-generating Liquid MOCVD Precursor for Co_3O_4 Thin Films. *Chemistry of Materials* 2003, 15, 3748-3752.

123. Farhadi, S.; Safabakhsh, J.; Zaringhadam, P. Synthesis, characterization, and investigation of optical and magnetic properties of cobalt oxide (Co_3O_4) nanoparticles. *Journal of Nanostructure in Chemistry* 2013, 3, 1-9.

124. Dorofeev, G.; Streletskii, A.; Povstugar, I.; Protasov, A.; Elsukov, E. Determination of nanoparticle sizes by X-ray diffraction. *Colloid Journal* 2012, 74, 675-685.

125. Scardi, P.; Leoni, M.; Delhez, R. Line broadening analysis using integral breadth methods: a critical review. *Journal of Applied Crystallography* 2004, 37, 381-390.

126. Lemine, O. M. Microstructural characterisation of nanoparticles using, XRD line profiles analysis, FE-SEM and FT-IR. *Superlattices and Microstructures* 2009, 45, 576-582.

127. Pan, D.; Zhang, J.; Li, Z.; Wu, M. Hydrothermal Route for Cutting Graphene Sheets into Blue-Luminescent Graphene Quantum Dots. *Advanced Materials* 2010, 22, 734-738.

128. Wang, G.; Yang, J.; Park, J.; Gou, X.; Wang, B.; Liu, H.; Yao, J. Facile Synthesis and Characterization of Graphene Nanosheets. *The Journal of Physical Chemistry C* 2008, 112, 8192-8195.

129. Saleh, T. A. The Role of Carbon Nanotubes in Enhancement of Photocatalysis. In *Syntheses and Applications of Carbon Nanotubes and Their Composites*; Suzuki, S., Ed.; Intechopen, 2013.

130. Kooti, M.; Matouri, L. A Facile and Mild Method for Synthesis of Nickel Oxide Nanoparticles in the Presence of Various Surfactants. Research and Reviews: *Journal Of Material Sciences* 2014, 2, 37-42.

131. Saghatforoush, L. A.; Hasanzadeh, M.; Sanati, S.; Mehdizadeh, R. Ni $(OH)_2$ and NiO nanostructures: synthesis, characterization and electrochemical performance. *Bulletin of the Korean Chemical Society* 2012, 33, 2613-2618

132. Hudson, J. B. *Surface Science: An Introduction*. Wiley: 1998.

133. Le Bourhis, E.; Patriarche, G. TEM-nanoindentation studies of semiconducting structures. *Micron* 2007, 38, 377-389.

134. Gervasi, C.; Alvarez, P.; Bimbi, M. F.; Folquer, M. Comparative cyclic voltammetry and SEM analysis of tin electrodes in citrate buffer solutions. *Journal of Electroanalytical Chemistry* 2007, 601, 194-204.

135. Zecho, T.; Güttler, A.; Küppers, J. A TDS study of D adsorption on terraces and terrace edges of graphite (0001) surfaces. *Carbon* 2004, 42, 609-617.

136. Boussouari, B., Baitoul, M. A Comparative Study of Multi-Walled Carbon Nanotubes Purification Techniques. *Journal of Materials Science and Engineering with Advanced Technology* 2014, 9, 1-15.

137. Osswald, S.; Havel, M.; Gogotsi, Y. Monitoring oxidation of multiwalled carbon nanotubes by Raman spectroscopy. *Journal of Raman Spectroscopy* 2007, 38, 728-736.

138. Xiang, L.; Deng, X. Y.; Jin, Y. Experimental study on synthesis of NiO nano-particles. *Scripta Materialia* 2002, 47, 219-224.

139. Sunohara, S.; Nishimura, K.; Yahikozawa, K.; Ueno, M.; Enyo, M.; Takasu, Y. Electrocatalysis of transition-metal oxides for reduction and oxidation of nitrite ions. *Journal of Electroanalytical Chemistry* 1993, 354, 161-171.

140. Xing, W.; Li, F.; Yan, Z.-f.; Lu, G. Q. Synthesis and electrochemical properties of mesoporous nickel oxide. *Journal of Power Sources* 2004, 134, 324-330.

141. Novoselov, K. S.; Geim, A. K.; Morozov, S. V.; Jiang, D.; Zhang, Y.; Dubonos, S. V.; Grigorieva, I. V.; Firsov, A. A. *Science* 2004, 306, 666.

142. Kampouris, D. K.; Banks, C. E. Exploring the physicoelectrochemical properties of graphene. *Chemical Communications* 2010, 46, 8986-8988.

143. Brownson, D. A.; Munro, L. J.; Kampouris, D. K.; Banks, C. E. Electrochemistry of graphene: not such a beneficial electrode material? *RSC Advances* 2011, 1, 978-988.

144. Henstridge, M. C.; Dickinson, E. J. F.; Compton, R. G. On the estimation of the diffuse double layer of carbon nanotubes using classical theory: Curvature effects on the Gouy–Chapman limit. *Chemical Physics Letters* 2010, 485, 167-170.

145. Pujadó, M. P. *Carbon nanotubes as platforms for biosensors with electrochemical and electronic transduction*. Springer Science & Business Media: 2012.

146. Xia, H.; Zhu, D.; Luo, Z.; Yu, Y.; Shi, X.; Yuan, G.; Xie, J. Hierarchically Structured Co_3O_4@Pt@MnO_2 Nanowire Arrays for High-Performance Supercapacitors. *Scientific Report* 2013, 3.

147. Laouini, E.; Hamdani, M.; Pereira, M.; Berghoute, Y.; Douch, J.; Mendonca, M.; Singh, R. Impedance study of spinel type Fe-Co3O4 oxide thin film electrodes in alkaline medium. *International Journal of Electrochemical Science* 2009, 4, 1074-84.

148. Danaee, I.; Jafarian, M.; Forouzandeh, F.; Gobal, F.; Mahjani, M. Impedance spectroscopy analysis of glucose electro-oxidation on Ni-modified glassy carbon electrode. *Electrochimica Acta* 2008, 53, 6602-6609.

149. Xiang, C.; Li, M.; Zhi, M.; Manivannan, A.; Wu, N. A reduced graphene oxide/Co3O4 composite for supercapacitor electrode. *Journal of Power Sources* 2013, 226, 65-70.

150. Khdary, N. H.; Abdesalam, M. E.; EL Enany, G. Mesoporous Polyaniline Films for High Performance Supercapacitors. *Journal of the Electrochemical Society* 2014, 161, G63-G68.

151. Aboutalebi, S. H.; Chidembo, A. T.; Salari, M.; Konstantinov, K.; Wexler, D.; Liu, H. K.; Dou, S. X. Comparison of GO, GO/MWCNTs composite and MWCNTs as potential electrode materials for supercapacitors. *Energy & Environmental Science* 2011, 4, 1855-1865.

152. Chidembo, A. T.; Ozoemena, K. I.; Agboola, B. O.; Gupta, V.; Wildgoose, G. G.; Compton, R. G. Nickel (II) tetra-aminophthalocyanine modified MWCNTs as potential nanocomposite materials for the development of supercapacitors. *Energy & Environmental Science* 2010, 3, 228-236.

153. Adekunle, A. S.; Agboola, B. O.; Pillay, J.; Ozoemena, K. I. Electrocatalytic detection of dopamine at single-walled carbon nanotubes–iron (III) oxide nanoparticles platform. *Sensors and Actuators B: Chemical* 2010, 148, 93-102.

154. Bouvrette, P.; Hrapovic, S.; Male, K. B.; Luong, J. H. T. Analysis of the 16 Environmental Protection Agency priority polycyclic aromatic hydrocarbons by high performance liquid chromatography-oxidized diamond film electrodes. *Journal of Chromatography A* 2006, 1103, 248-256.

155. Skandan, G.; Singhal, A.; Contescu, C.; Putyera, K. *Dekker encyclopedia of nanoscience and nanotechnology*. Taylor & Francis: 2009.

156. Li, W.; Tan, C.; Lowe, M. A.; Abruna, H. D.; Ralph, D. C. Electrochemistry of individual monolayer graphene sheets. *ACS nano* 2011, 5, 2264-2270.

157. Hammel, K. E.; Kalyanaraman, B.; Kirk, T. K. Oxidation of polycyclic aromatic hydrocarbons and dibenzo[p]-dioxins by Phanerochaete chrysosporium ligninase. *Journal of Biological Chemistry* 1986, 261, 16948-16952.

158. Kodera, F.; Umeda, M.; Yamada, A. Detection of hypochlorous acid using reduction wave during anodic cyclic voltammetry. *Japanese Journal of Applied Physics* 2005, 44, L718.

159. El-Ashtoukhy, E. S. Z.; Amin, N. K. Removal of acid green dye 50 from wastewater by anodic oxidation and electrocoagulation—A comparative study. *Journal of Hazardous Materials* 2010, 179, 113-119.

160. Björk, J.; Hanke, F.; Palma, C.-A.; Samori, P.; Cecchini, M.; Persson, M. Adsorption of aromatic and anti-aromatic systems on graphene through π− π stacking. *The Journal of Physical Chemistry Letters* 2010, 1, 3407-3412.

161. Ji, L.; Chen, W.; Xu, Z.; Zheng, S.; Zhu, D. Graphene Nanosheets and Graphite Oxide as Promising Adsorbents for Removal of Organic Contaminants from Aqueous Solution. *Journal of Environmental Quality* 2013, 42, 191-198.

162. Majdi, S.; Jabbari, A.; Heli, H.; Moosavi-Movahedi, A. A. Electrocatalytic oxidation of some amino acids on a nickel–curcumin complex modified glassy carbon electrode. Electrochimica Acta 2007, 52, 4622-4629.

163. Bard, A. J.; Faulkner, L. *Electrochemical methods: fundamentals and applications*. 2nd ed.; John Wiley & Sons, 2001.

164. Iwuoha, E. I.; Saenz de Villaverde, D.; Garcia, N. P.; Smyth, M. R.; Pingarron, J. M. Reactivities of organic phase biosensors. 2. The amperometric behaviour of horseradish peroxidase immobilised on a platinum electrode modified with an electrosynthetic polyaniline film. *Biosensors and Bioelectronics* 1997, 12, 749-761.

165. Zen, J. M.; Senthil Kumar, A.; Chang, M. R. Electrocatalytic oxidation and trace detection of amitrole using a Nafion/lead–ruthenium oxide pyrochlore chemically modified electrode. *Electrochimica Acta* 2000, 45, 1691-1700.

166. Soderberg, J. N.; Co, A. C.; Sirk, A. H.; Birss, V. I. Impact of porous electrode properties on the electrochemical transfer coefficient. *The Journal of Physical Chemistry B* 2006, 110, 10401-10410.

167. Agboola, B.; Nyokong, T. Comparative electrooxidation of nitrite by electrodeposited Co(II), Fe(II) and Mn(III) tetrakis (benzylmercapto) and tetrakis (dodecylmercapto) phthalocyanines on gold electrodes. *Analytica Chimica Acta* 2007, 587, 116-123.

168. Bard, A. J.; Faulkner, L. R. *Electrochemical methods: fundamentals and applications*. Wiley New York: 1980; Vol. 2.

169. Christian, G. D. Analytical chemistry, 6th ed.; Wiley: 2004.

170. Tovide, O. O. Graphenated Polyaniline Nanocomposite for the Determination of Polyaromatic Hydrocarbons (PAHs) in Water. Ph.D. Thesis, University of the Western Cape, Western Cape, Cape Town, Bellvile, 2013.

171. Wang, W.-D.; Huang, Y.-M.; Shu, W.-Q.; Cao, J. Multiwalled carbon nanotubes as adsorbents of solid-phase extraction for determination of polycyclic aromatic hydrocarbons in environmental waters coupled with high-performance liquid chromatography. *Journal of Chromatography A* 2007, 1173, 27-36.

172. Ju, H.; Leech, D. Electrochemical study of a metallothionein modified gold disk electrode and its action on Hg^{2+} cations. *Journal of Electroanalytical Chemistry* 2000, 484, 150-156.

173. Avci, G. Corrosion inhibition of indole-3-acetic acid on mild steel in 0.5 M HCl. *Colloids and Surfaces A: Physicochemical and Engineering Aspects* 2008, 317, 730-736.

174. Ehli, C.; Rahman, G. M. A.; Jux, N.; Balbinot, D.; Guldi, D. M.; Paolucci, F.; Marcaccio, M.; Paolucci, D.; Melle-Franco, M.; Zerbetto, F.; Campidelli, S.; Prato, M. Interactions in Single Wall Carbon Nanotubes/Pyrene/Porphyrin Nanohybrids. *Journal of the American Chemical Society 2006*, 128, 11222-11231.

APPENDICES

APPENDIX I

Formulas used

Einsteins' Equation: $E_g = h \times {}^{C}/_{\lambda}$

Scherrer Equation: $D = \frac{K\lambda}{B\,Cos\theta}$

Laviron equation : $I_P = \frac{n^2F^2\upsilon A\Gamma}{4RT}$

Surface coverage: $\Gamma = \frac{Q}{nFA}$

¤ Half-wave potential $E_{1/2}$: $E_{1/_2} = E^0 + \frac{RT}{2F} ln \frac{[O]}{[R]}$

¤ Peak potential separation Δ E_p : $\Delta E_p = E_{pc} - E_{pa} = \frac{RT}{nF}$

at 25°C, $\Delta E = \frac{59\,mV}{n}$

¤ Randles- Sevčik equation : $I_p = (2.69\ x\ 10^5)n^{3/2}\,[O]A(Dv)^{1/2}$

§ Randles- Sevčik equation : $I_p = (2.99\ x\ 10^5)n[(1-\alpha)n]^{\frac{1}{2}}AC(Dv)^{1/2}$

Electron transfer rate constant: $k_s = \frac{RT}{n^2F^2AR_{ct}}$

§ Tafel equation : $E_P = \left(\frac{b}{2}\right)\log\upsilon + k$ or $E_p = k + \frac{2.303RT}{2(1-\alpha)n_\alpha F}\log\upsilon$

Limit of detection : LoD = ${3.3\,\delta}/{m}$

Langmuir Adsorption Isotherm equation $\frac{[Pyrene]}{I_P} = \frac{1}{\beta I_P} + \frac{[Pyrene]}{I_P}$

Gibbs standard free energy of adsorption $\Delta G^O_{ads} = -RT\ ln\beta$

Where R is the molar gas constant, T, is temperature (K), F is the Faraday constant (96 485 $Cmol^{-1}$) and [O] and [R] are concentration ($mol.L^{-1}$) of the oxidized and reduced species, respectively; E_{Pc} and E_{Pa} are the cathodic and anodic peak potential, respectively, and n is the number of electrons transferred. I_P is the peak current (A) , A, electrode area (cm^{-2}), D, diffusion coefficient ($cm^2.s^{-1}$), and v, the scan rate ($V.s^{-1}$)

¤ *For reversible electrochemical process (Model redox probe $[Fe(CN)_6]^{-3}$ /$[Fe(CN)_6]^{-4}$).*

§ *For Irreversible electrochemical process (Pyrene).*

APPENDIX II

Conference presentations from this thesis:

"*Electrochemical Properties of Graphene oxide/Metal oxide nanocomposite*."
Diseko Boikanyo, Abolanle S. Adekunle and Eno E. Ebenso.
7th International Symposium on Macro- and Supramolecular Architectures and Materials (MAM-14). 23-27 November 2014. Johannesburg South Africa. (**ORAL PRESENTATION BY Diseko Boikanyo**)

" Electrochemical Properties of Graphene oxide and MWCNT/ Metal oxide nanocomposites for the detection of Pyrene."
Diseko Boikanyo, Abolanle S. Adekunle and Eno E. Ebenso.
3rd International Symposium on Electrochemistry (MAPET '15). 26-28 May 2015. Belville, South Africa. (**ORAL PRESENTATION BY Diseko Boikanyo**)

Paper submitted for publication from this thesis:

D. Boikanyo, Abolanle S. Adekunle, Eno. E. Ebenso, (2015). "*Electrochemical Study of Pyrene on Glassy Carbon Electrode Modified with Metal-Oxide Nanoparticles and Graphene Oxide / Multi-Walled Carbon Nanotubes Nanoplatform*"
Accepted for publication in **STV: Nanomaterials for Electrocatalysis and Electrochemical Energy Applications:**